PNL-7106
UC-313

18J

Inert Electrodes Program

Fiscal Year 1988 Annual Report

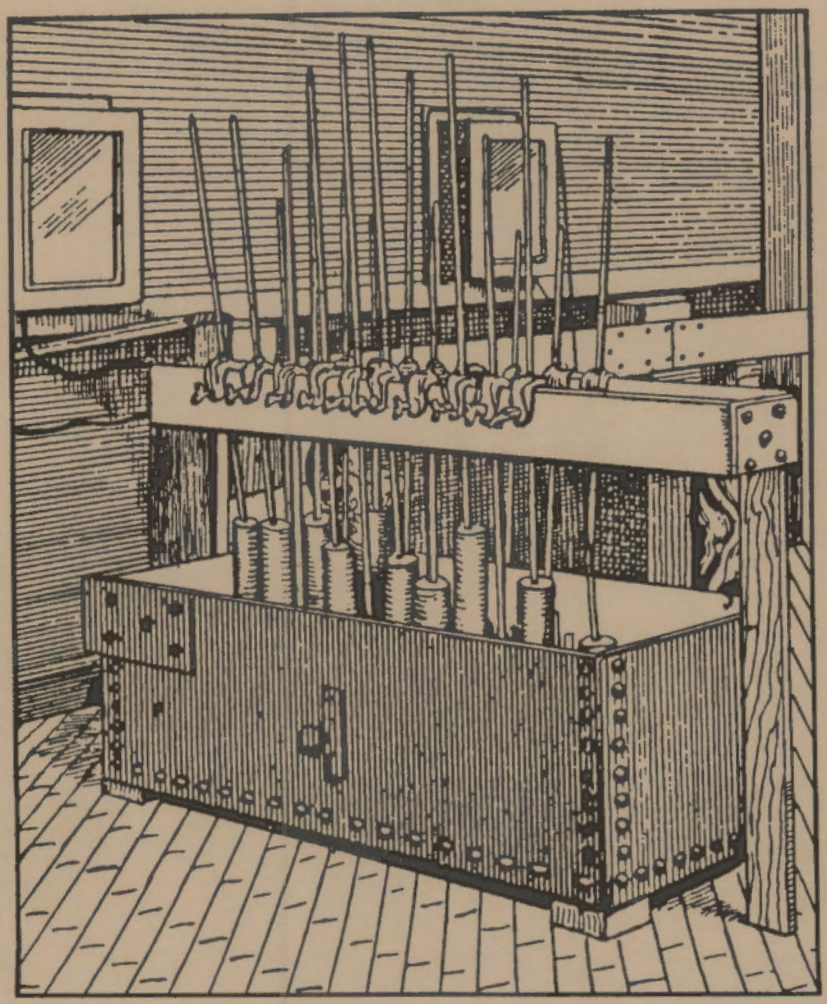

October 1989

Prepared for the U.S. Department of Energy
under Contract DE-AC06-76RLO 1830

Pacific Northwest Laboratory
Operated for the U. S. Department of Energy
by Battelle Memorial Institute

Battelle

PNL-7106

On the cover:

Aluminum reduction pots at the Pittsburgh Reduction Company's (Alcoa's) plant in 1889. Adapted from a photograph, courtesy of Alcoa.

PACIFIC NORTHWEST LABORATORY
operated by
BATTELLE MEMORIAL INSTITUTE
for the
UNITED STATES DEPARTMENT OF ENERGY
under Contract DE-AC06-76RLO 1830

Printed in the United States of America

Available to DOE and DOE contractors from the
Office of Scientific and Technical Information, P.O. Box 62, Oak Ridge, TN 37831;
prices available from (615) 576-8401. FTS 626-8401.

Available to the public from the National Technical Information Service,
U.S. Department of Commerce, 5285 Port Royal Rd., Springfield, VA 22161.

NTIS Price Codes, Microfiche A01

Printed Copy

Pages	Price Codes
001-025	A02
026-050	A03
051-075	A04
076-100	A05
101-125	A06
126-150	A07
151-175	A08
176-200	A09
201-225	A10
226-250	A11
251-275	A12
276-300	A13

PNL-7106
UC-313

Inert Electrodes Program

FISCAL YEAR 1988 ANNUAL REPORT

D. M. Strachan
S. C. Marschman
N. C. Davis
J. R. Friley
C. H. Schilling

October 1989

Prepared for
the U.S. Department of Energy
under Contract DE-AC06-76RLO 1830

Pacific Northwest Laboratory
Richland, Washington 99352

ACKNOWLEDGMENTS

The authors wish to acknowledge the technical assistance of L. S. Dake, H. E. Kissinger, K. H. Pool, N. T. Saenz, S. O. Slate, D. E. Smith, and R. W. Stephens, Pacific Northwest Laboratory (PNL), for their contributions to the performance of the experimental and analytical work; the valuable contributions of W. E. Haupin and R. Keller, program consultants; the assistance of R. E. Westerman and S. R. Gano in performing the technical and editorial reviews of the report; the programmatic assistance provided by M. J. McMonigle, Office of Industrial Programs, U.S. Department of Energy (DOE), Washington, D.C., and P. M. Pak and D. R. Segna, Richland Operations Office, DOE; and the programmatic support provided by the Office of Industrial Programs, DOE.

SUMMARY

The Inert Electrodes Program, being conducted by Pacific Northwest Laboratory (PNL), involves improving the Hall-Heroult cells used by the Aluminum Industry for the electrochemical production of aluminum. The PNL research centers on developing more energy efficient, longer-lasting anodes and cathodes and ancillary equipment. Major accomplishments for Fiscal Year 1988 are summarized below.

SCALE-UP ACTIVITIES

The scale-up activities involved working with industry to produce and test industrial-scale anodes. Two companies were selected for construction of a prototype anode and for pilot testing a cluster of inert anodes.

Thermal and mechanical properties of the anode were evaluated and the data incorporated in the finite element analyses, which were used to better understand the behavior of the anode during thermal events. The finite element analyses indicated that differences in coefficients of thermal expansion among materials in the anode are the primary causes of thermal stresses and potential distortion. Stresses caused by thermal nonuniformity within the anode are, for the conditions studied, of secondary importance.

The electrical connection developed by PNL for large anodes is produced by including a "core" of Cu/Ni alloy powder in the anode while the anode mold is being filled. This powder core is then pressed and sintered as part of the anode. After sintering, the core is drilled and tapped to form a threaded connection between the electrical conductor/support rod and the cermet anode body.

ANODE PERFORMANCE

In the Anode Performance task, confirmation tests were conducted to evaluate cermets based on the two-phase oxide system NiO-Fe_2O_4, containing a third electrically conductive metal phase primarily composed of copper or copper/nickel alloy. Also, a long-term test was conducted on a new cell under conditions suitable for operation of inert anodes. Work was also

directed towards designing and fabricating an experimental apparatus for determining current efficiency with variable anode-to-cathode distance (ACD) during the electrolytic production of aluminum with cermet laboratory-scale anodes.

The laboratory confirmation testing was useful in obtaining a better understanding of electrolysis cell operating parameters. Operating conditions that lead to anode degradation have been partly identified, and some control methods have been developed to ensure proper operation of small electrolysis cells using nonconsumable anodes. Laboratory-scale testing showed the NiO-$NiFe_2O_4$-Cu[(a)]-based cermets are potentially viable as nonconsumable anodes for use in the electrolytic production of aluminum.

The long-term testing involved a new cell made of SiC, which was expected to withstand attack by cryolite. However, the SiC oxidized and dissolved in the cryolite. While the test was terminated as a result of SiC interference and cell degradation, some useful information was obtained on the chemical processes that occurred in the cell.

The apparatus being constructed for reduced ACD testing is designed to evaluate current efficiency as a function of several parameters. These parameters include anode-cathode spacing, anode and cathode slope, bath chemistry, different electrode geometries, and different electrode materials.

ANODE MATERIALS

Work continued on producing standard anode materials for use in electrolysis testing and sensor development. Some anodes were fabricated from NiO-$NiFe_2O_4$-17 wt% Cu by using a PNL-developed powder rather than spray-dried powder. The PNL procedure appeared to produce a more homogeneous microstructure. Other fabrication work centered on NiO-$NiFe_2O_4$-Cu-Ni-Al cermets, which exhibited the highest electrical conductivities measured.

(a) Throughout this report, this designation is used for simplicity to describe the cermet anode material. It is not meant to imply an exact composition, however. A more accurate designation would be $Ni_xFe_{1-x}O$-$Ni_yFe_{3-y}O_4$. The metal phase, e.g., Cu, is designated as a weight percent addition.

CATHODE PERFORMANCE

In the cathode performance task, the degradation mechanisms for TiB_2-graphite cathode materials were studied. Results indicated that the time at maximum temperature with no electrolysis affected spalling, Al_4C_3 formation, penetration by molten Al, and subsurface cracking of the TiB_2-graphite material. While further study of the TiB_2-graphite materials is not specifically planned, these materials will be included as cathodes in laboratory-scale electrolysis cells. Only limited evaluations of these materials will be performed.

CONTENTS

FIGURES

TABLES

1.0 INTRODUCTION

The Inert Electrodes Program is being conducted at the Pacific Northwest Laboratory (PNL)[a] for the U.S. Department of Energy (DOE), Office of Industrial Programs (OIP). The purpose of the program is to develop long-lasting, energy-efficient anodes and ancillary equipment for Hall-Heroult cells used by the aluminum industry. Emphasis has been placed on the development of anodes made from a ceramic/metal composite consisting of Ni and Cu oxides and a Cu/Ni metal phase. These anodes are expected to have lifetimes of 5 to 7 years, as opposed to the current technology, which requires replacement of carbon anodes approximately every 20 days. The program is in a transition phase, in which experience gained with laboratory-scale anode production and evaluation technology is being scaled up in preparation for large-scale pilot tests that will take place in FY 1989.

- Scale-up Activities. The objective of this task is to produce and test industrial-scale anodes, and to transfer the associated technology to industry.

  In FY 1988, this task oversaw the solicitation of industrial cooperation in the testing of large-scale anodes; the determination of mechanical/physical properties of the cermet material, and a finite element stress analysis of the conceptual anode design, to assist in formulating operating procedures and ensure adequate attention to design details; and the development of a method to obtain a robust junction between the cermet anode body and the electrical conductor/anode support rod.

- Anode Performance. The objective of this task is to evaluate the performance of anode materials based on the two-phase oxide system NiO-$NiFe_2O_4$, containing an electrically conductive metal phase composed primarily of Cu and Ni, under laboratory-scale electrolysis conditions.

  In FY 1988, the behavior of test anodes was determined in electrolytes of varying composition; the effect of anode geometry (flat bottom versus round bottom) was investigated; the sources of impurities in the Al produced were addressed; and the performance of cermets containing metallic Ni and Al in addition to Cu were evaluated.

(a) Operated for the U.S. Department of Energy by Battelle Memorial Institute under Contract DE-AC06-76RLO 1830.

- Anode Materials. The objective of this task is to produce and characterize inert anode materials for laboratory-scale testing and for sensor applications.

  In FY 1988, the effect of composition, powder type/source, and processing parameters on the density and microstructures of the anodes produced for testing were catalogued to provide a reference base for future anode production.

- Cathode Performance. The objective of this task is to promote the application of an inert cathode material in Hall-Heroult cells by evaluating the compatibility of the candidate TiB_2-graphite material with electrolysis-cell bath constituents.

  In FY 1988, TiB_2-graphite materials, considered to be candidate materials for use as cathodes in Hall-Heroult cells, were exposed to electrolysis cell environments in conjunction with inert anode studies. The degradation of the cathode material was evaluated as a function of cell operating conditions, and plausible degradation mechanisms were explored.

This Inert Electrodes Program annual report highlights the major technical accomplishments of FY 1988. The accomplishments are presented in the following sections: Management, Scale-Up Activities, Anode Performance, Anode Materials, and Cathode Performance. Also included is a Conclusions/Future Directions section and an appendix, which contains discussion of the thermophysical properties of a cermet.

2.0 MANAGEMENT

Laboratory work at the Pacific Northwest Laboratory continued to demonstrate that inert anode technology is viable. Tests in laboratory cells with capacities up to 60 amperes were performed, with successful production of low-impurity-level aluminum. Laboratory-size anodes were successfully produced in a variety of shapes, and a superior method of making the electrical connection to the anode was developed. Efforts in FY 1988 included scale-up activities, bringing the technology closer to commercial reality.

Work with cathode materials decreased during FY 1988. However, work performed during FY 1988 corroborated the mechanism of degradation of TiB_2-graphite that had been postulated in FY 1987.

Two papers were presented at the Electrochemical Society Meeting in Atlanta, Georgia, May 15-20, 1988. The following presentations were made: Evaluation of TiB_2-Based Cathodes for Aluminum Processing Applications by C. H. Schilling and S. C. Marschman and Development and Testing of Non-Consumable Anodes for the Electrolytic Production of Aluminum by S. C. Marschman. In addition, three metallographic exhibits were submitted to society meetings: Microstructural Changes in Cermets Used for the Electrolytic Production of Aluminum by N. T. Saenz, S. C. Marschman, N. C. Davis, and D. H. Parks (Prize - Honorable Mention International Metallographic Society Contest, Composites Class, July, 1988, Toronto, Canada); Aluminum Penetration in TiB_2-Graphite Composites by N. T. Saenz, C. H. Schilling, D. H. Parks, and G. L. Graff (Prize - Third Place International Metallographic Society Contest, Composites Class, July, 1988, Toronto, Canada); and Elemental Segregation in TiB_2-Graphite Cathode During Aluminum Smelting by C. H. Schilling, N. T. Saenz, H. Kjarmo, G. L. Graff, and S. C. Marschman (Prize - Honorable Mention, 1987 American Ceramic Society Ceramography Contest, Pittsburgh).

The following reports were published during FY 1988: Marschman, S. C., N. C. Davis, and R. W. Stephens. 1987. Nonconsumable Anode Electrical Contacts and Support Mechanisms, PNL-6393, Pacific Northwest Laboratory, Richland, Washington; Schilling, C. H. 1988. Laboratory Testing of TiB_2-

Based Cathodes for Electrolytic Production of Aluminum, PNL-6594, Pacific Northwest Laboratory, Richland, Washington; and Schilling, C. H. and G. L. Graff. 1988. Immersion Tests of TiB_2-Based Materials for Aluminum Processing Applications, PNL-6593, Pacific Northwest Laboratory, Richland, Washington.

An industry review meeting was held in Seattle, Washington, November 3, 1987. Representatives from the major aluminum companies, the Bonneville Power Administration, Eltech, and the U.S. Department of Energy attended this review meeting. Details of the program activities were presented. Four program review meetings were held--two in Washington, D.C., and two in Richland, Washington.

Two new consultants were retained by the program. Mr. Fred Huetig was retained for his expertise in the ferrite industry. Mr. Huetig will be assisting the program in scale-up and production of anodes. Mr. Max Adkins was also retained by the program. He will assist the program by making economic assessments of the inert anode technology.

The program staff hosted several visitors from various ceramics industries interested in producing TiB_2 cathode materials or ferrite anode materials. Dr. Jomar Thonstad from Trondheim University, Trondheim, Norway, also visited PNL. He discussed the research being performed in his laboratory on inert anodes for aluminum smelting.

3.0 SCALE-UP ACTIVITIES

Scale-up activities included selecting two private companies for producing and pilot testing large anodes. The other tasks involved development of an electrical connection that also acts as the anode support; evaluation of thermal/mechanical properties of the anode; and finite element analyses, using the thermal and mechanical data, to better understand the behavior of the large anode during thermal events.

3.1 INDUSTRIAL PARTICIPATION

During FY 1988, industrial participation in the Inert Electrodes Program was solicited to bring industrial partners into the program; to gain additional insight into the industrial approach for commercializing the inert anode technology; and to begin transferring the technology to industry. The solicitation process involved publishing the "intent to issue request for proposals" in the Commerce Business Daily (CBD). From the response to the advertisement in CBD, a list of candidate companies was formed and requests for proposals were mailed to these companies. Each request for proposal contained detailed information on one of two projects--construction of a prototype anode and performance of a pilot test of a cluster of inert anodes. Proposals from two companies for anode construction and one company for the pilot cell test were evaluated. One company for each task was selected by an evaluation committee based on evaluation criteria set at the time the requests for proposals were sent to the candidate companies.

The first large anodes will be produced at Cercom, Inc., Vista, California. These anodes will be a simple, cup-shaped design, approximately 15 cm (6 in.) in diameter and 20 cm (8 in.) high. In this design, optimum gas release is not a consideration. Survivability tests are planned to demonstrate the performance of the anode material at the prescribed operating conditions.

The schedule for the delivery of the large anodes calls for the first or prototype anode to be delivered to PNL at the end of February 1989. This anode will be nondestructively examined for defects, fitted with an

electrical connection and sensor connections, and shipped to Reynolds Metals Co., Sheffield, Alabama, where laboratory tests will be run.

The laboratory test will be initiated in March 1989 with a single anode and an externally heated, Al_2O_3-lined, graphite cell approximately 18 cm (7.5 in.) in diameter. After a successful laboratory test, additional anodes will be produced for testing in a large pilot cell at the Reynolds Metals Co. For the large-scale test, a cluster of six inert anodes will be tested in the pilot cell. The total amperage through this cluster will be in the range of 1 kA to 1.2 kA. A carbon anode within the cell will be used to supply most of the heat needed to keep the cell functional. The test will run for 3 weeks and anodes will be changed each week. This test will be used to evaluate the survivability of inert anodes under nearly industrial conditions, to obtain an estimate of the impurity level in the metal produced, and to determine operating parameters of the inert anodes. The large-scale test is scheduled for the summer of 1989, with the exact date depending on the anode production schedule.

3.2 ELECTRICAL CONNECTION

Cermet materials typically are difficult to join to other materials while maintaining good electrical conductivity and mechanical strength. Scientists at Alcoa made successful experimental joints by reducing cermet surfaces with carbon, then diffusion-welding the reduced layer to nickel stubs (Weyand et al. 1986). They also included a transition zone (a tailored cermet-metal mix) between the cermet, the diffusion weld, and the nickel stub. Mechanical joining of the anode to the electrical conductor has attractive features, but has not been pursued because of the hostile operating environment.

Nickel continues to be the principal material candidate for the electrical connectors because the coefficient of thermal expansion for Ni (13.3×10^{-6} cm/cm-°C) is similar to that for the cermet material $10.3\text{-}13.1 \times 10^{-6}$ cm/(cm-°C) (see Table 3.2). In addition, Ni is readily fabricated and appears to have adequate strength at elevated temperatures. The dual objectives of a higher-strength junction and elimination of the reduction step

could be realized if a metal alloy core could be placed in the anode during fabrication, sintered in place without excessive oxidation, and later drilled and tapped. This concept is the subject of this section.

At PNL brazing was identified as a technique that could be used effectively to join the cermet anode to nickel metal (Marschman, Davis, and Stephens 1987). This method was a two-step technique involving treatment of the surface to be brazed with Ar/4% H_2 followed by furnace brazing of the Ni rod using a Cu/20% Ni alloy. This furnace-brazed connection was satisfactory for electrochemical testing of small anode samples. There was concern, however, that larger anodes would require additional mechanical strength at the connector junction; also, it was evident that the H_2 reduction step presented some process control difficulties. Parts of the anode other than the region being prepared for the electrical connection could be reduced.

3.2.1 Fabrication

In the following procedure, the preparation of the electrical connection is described. A major portion of the procedure is carried out prior to sintering the anode. The configuration of the isostatic press mold components are shown in Figure 3.1.

1. The rubber mold sleeve is placed on the forming mandrel and the assembly is placed on a vibrating table.
2. Cermet powder is loaded into the annular space between the mold sleeve and the mandrel, forming the thin walls of the anode.
3. Filling of the mold is interrupted when the powder level reaches the top of the mandrel.
4. A small rigid sleeve is placed on top of the mandrel to locate, center, and contain the metal alloy powder.
5. After the metal powder is in position and additional cermet powder is added to the annulus between the retaining sleeve and the mold sleeve, the retaining sleeve is removed. This leaves the metal alloy powder in a central position for later electrical connection.
6. The balance of the cermet powder is loaded, the closure plug is sealed in position, and the mold is isostatically pressed.
7. Machining may be performed on the green anode if required. For example, a pilot hole may be drilled for the electrical connection.

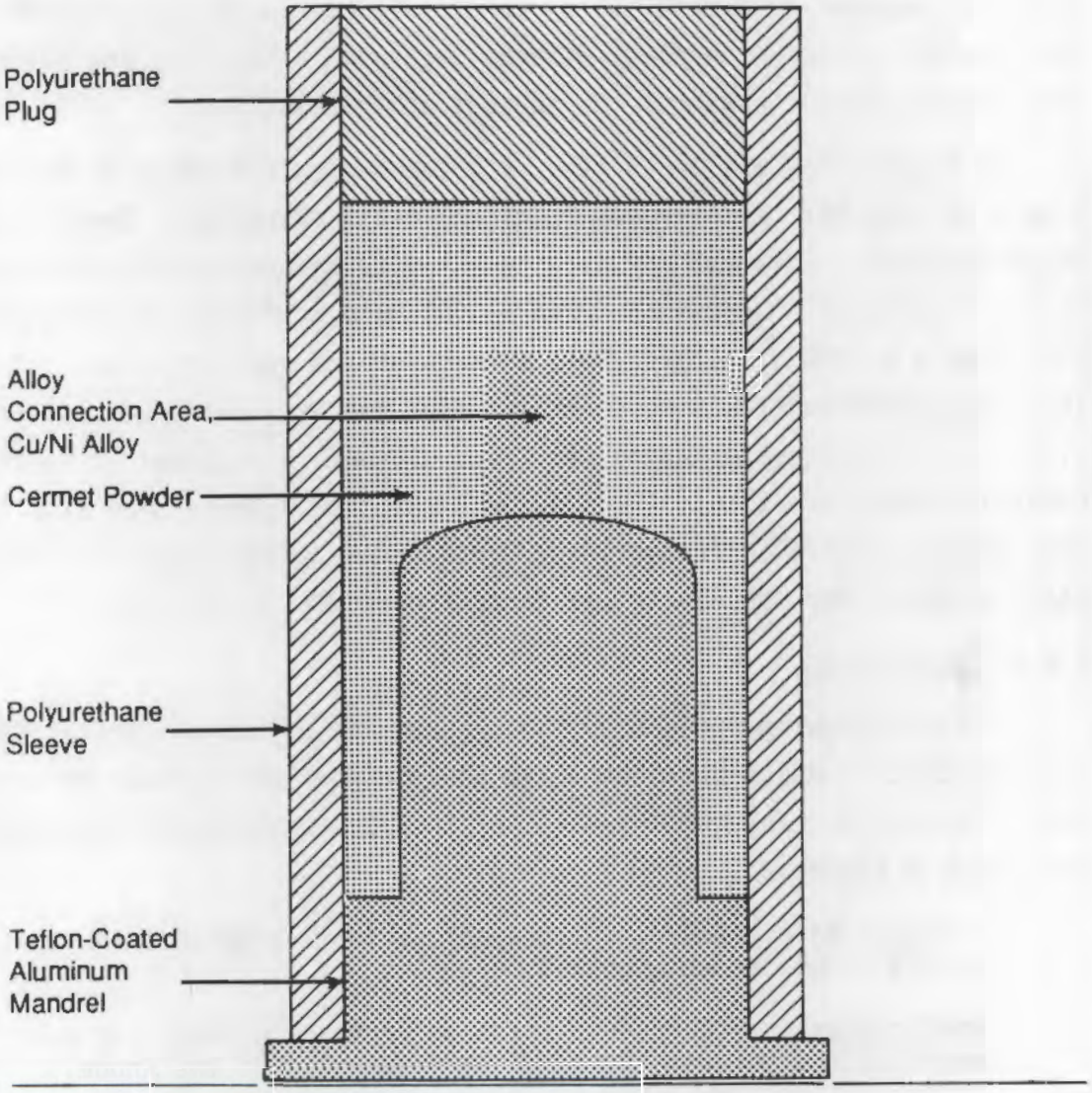

FIGURE 3.1. Isostatic Pressing Mold

8. The final drilling and tapping is done on the sintered anode. This provides clean, freshly cut, highly conductive metal threads without the need for hydrogen reduction.

Drilling and thread tapping have been successful using 80/20, 70/30, 65/35, 60/40 and 50/50 wt% Cu/Ni alloys in both standard fine and coarse threads. To obtain the highly conductive, oxide-free surface for this connection, the drilling (to size) and tapping should be the final post-sintering operation.

Several anodes have been made using the Cu/Ni alloy plug for the electrical connection. Of these anodes, four (Anodes 148, 149, 150, and 152) have been selected to illustrate the results obtained in the use of this connection. Standard sintering conditions (Marschman and Davis 1987) were used to produce all four of the anodes shown in Figures 3.2 through 3.5. The threaded core in one anode, Anode 148, was given a reduction treatment with an Ar-H_2 gas mixture prior to brazing a Ni conductor rod in place. The cores of the other three anodes described did not receive a reduction treatment, nor was the Ni rod brazed in place prior to testing in an electrolysis cell; the drilling and tapping of the electrical connection was done after the sintering of these anodes, and the connector rods were simply screwed into place. The details of the production of each anode connection are discussed in Table 3.1.

3.2.2 Results of Connection Evaluation

Results from the four anodes are summarized in Figures 3.2 through 3.9. Figures 3.2 through 3.5 are low-magnification photographs of the sectioned Anodes 148, 149, 150, and 152, and Figures 3.6 through 3.9 are higher magnifications of the electrical connection. Fracturing of the anodes is believed to have resulted from the thermal shock the anodes received when air-quenched from 950°C. The cross-sectional surfaces of these anodes were polished only enough to permit observation of relatively large-scale details of interest.

Examination of the electrical connection area in Anode 148 reveals that the furnace brazing operation achieved the intended goal. The bond between the Ni rod and the core material appears to be solid, with only small gaps between the threads. Not evident in these photos is a problem associated with the use of Ar/4% H_2, i.e., reduction of other parts of the anode surface to the metallic state as a result of difficulties in gas control. Base metals (Cu, Ni, Fe) are more easily corroded in cryolite than in the ferrite material. Thus, unless extreme care is exercised, unwanted side effects will result from the use of a reducing gas. Moreover, it appears that a reduction treatment is not needed.

FIGURE 3.2. Anode 148

FIGURE 3.3. Anode 149

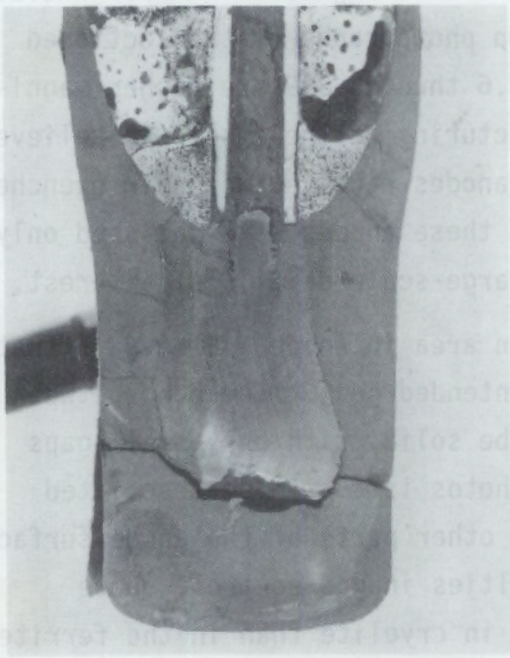

FIGURE 3.4. Anode 150

FIGURE 3.5. Anode 152

TABLE 3.1. Anode Production Details

Anode Number	Comments
148	The cermet material consisted of 83% NiO-$NiFe_2O_4$[(a)] and 17% Cu metal. A 60% Cu/40% Ni powder core was pre-formed into the cermet as previously described. Surrounding this core material was a transition zone between the core and the cermet consisting of 50% metal/50% ceramic. Threads were tapped into the metal core after sintering. The threaded area was treated with Ar/4% H_2 at 800°C, prior to brazing-in the Ni conductor. The Ni rod was furnace brazed at 1200°C using an 80% Cu/20% Ni braze alloy. This anode was not used in an electrolysis cell.
149	The cermet material consisted of 83% NiO-$NiFe_2O_4$ and 17% Cu. Surrounding the 60% Cu/40% Ni core material was a transition zone consisting of 50% cermet and 50% metal. Standard 1/4 x 20 threads were tapped into the metal core. No furnace brazing of the Ni rod was used; the Ni rod was simply screwed into the metal core prior to use in a 100-h electrolysis test.
150	The cermet material consisted of 83% NiO-$NiFe_2O_4$ and 17% Cu. No transition zone was employed between the metal core and the cermet. Standard 1/4 x 20 threads were used on the Ni rod and in the 70% Cu/30% Ni core. The anode was used for 68 h in an electrolysis test.
152	This anode was fabricated in the same manner as Anode 150 except that the cermet material was processed from the raw oxides of NiO and Fe_2O_3, rather than using the spray-dried NiO-$NiFe_2O_4$. The anode was used for 100 h in an electrolysis test.

(a) Throughout this report, this designation is used for simplicity to describe the cermet anode material. It is not meant to imply an exact composition, however. A more accurate designation would be $Ni_xFe_{1-x}O$-$Ni_yFe_{3-y}O_4$. The metal phase, e.g., Cu, is designated as a weight percent addition.

In Anodes 149, 150, and 152, the Ni rod was screwed into place before the electrolysis test. The photographs (Figures 3.3 through 3.5 and 3.7 through 3.9) reveal that significant diffusion welding occurred at the cell operating temperature (~970°C). In most cases it is difficult to make out the original outline of the threads in the macrographs obtained from these polished (but unetched) metallographic specimens. Diffusion of the metal core into the cermet and the effect of the transition zone cannot be evaluated from these photographs, nor can the benefit of a transition zone.

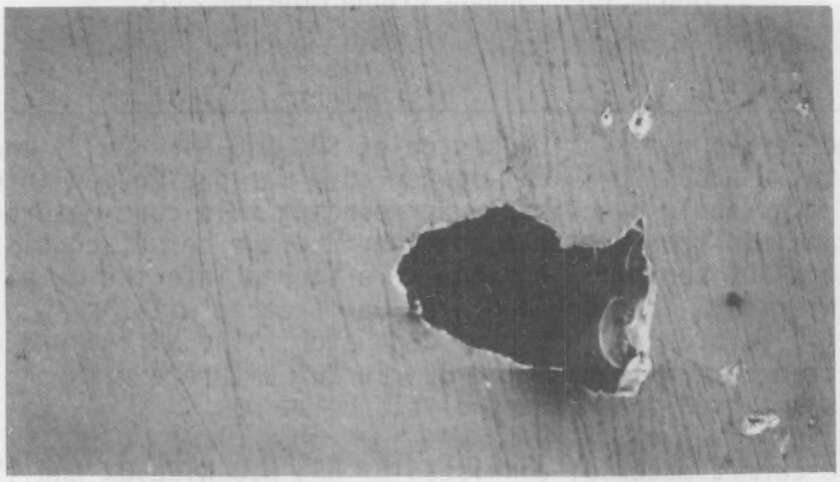

100X

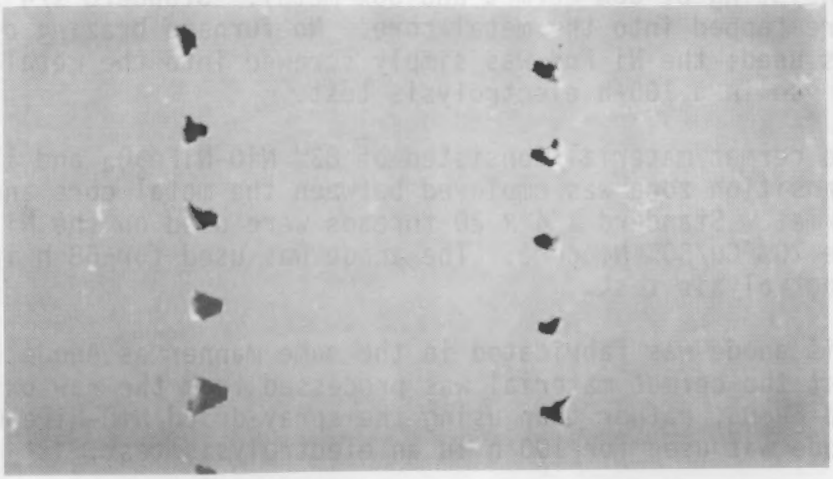

20X

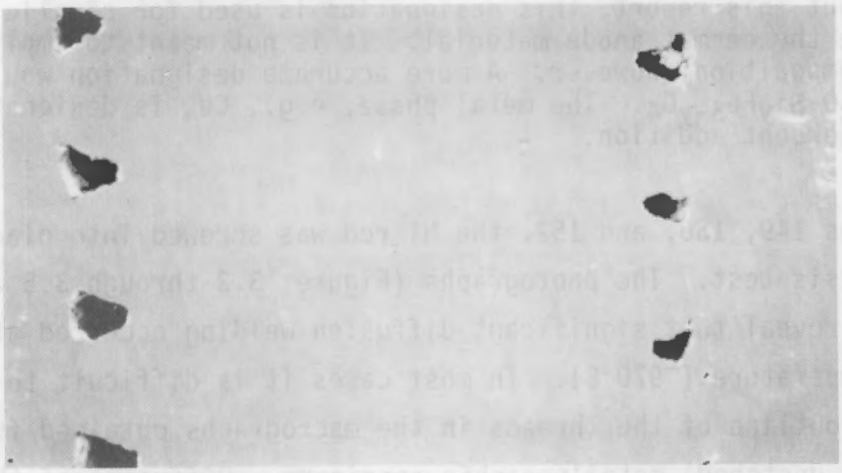

13X

FIGURE 3.6. Anode 148

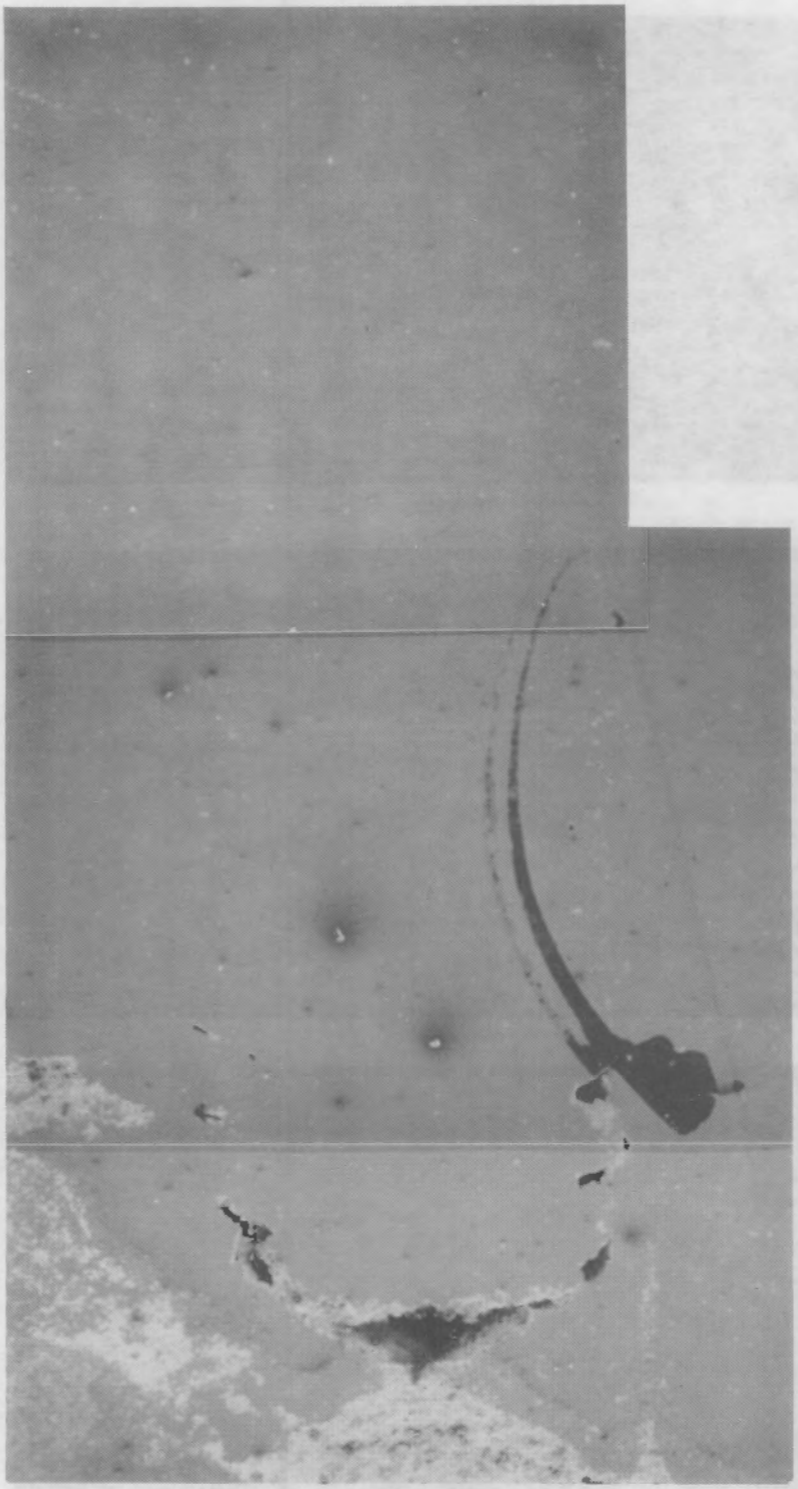

FIGURE 3.7. Anode 149

100X

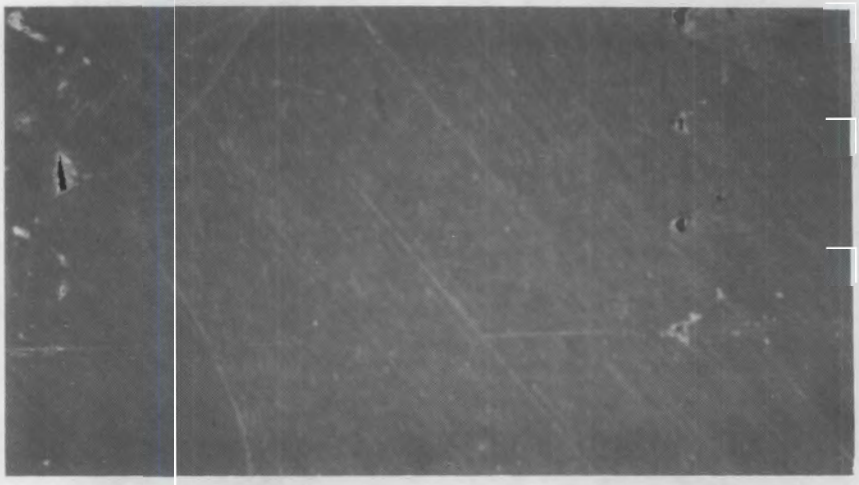

20X

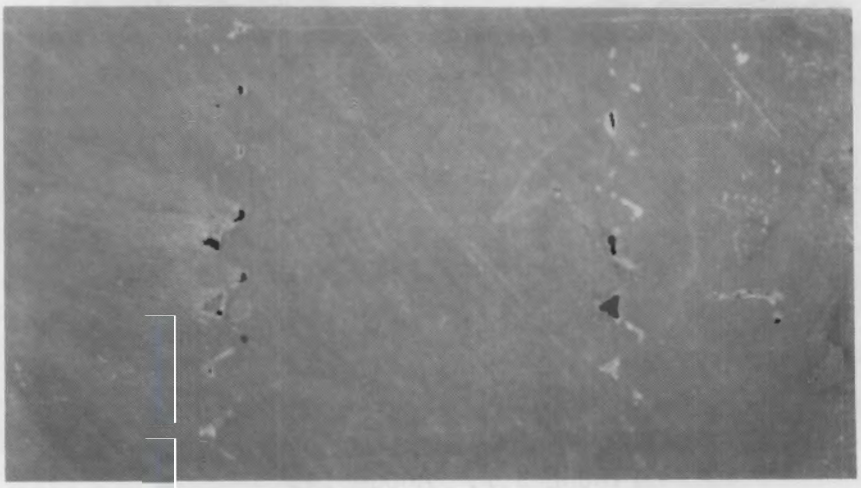

13X

FIGURE 3.8. Anode 150

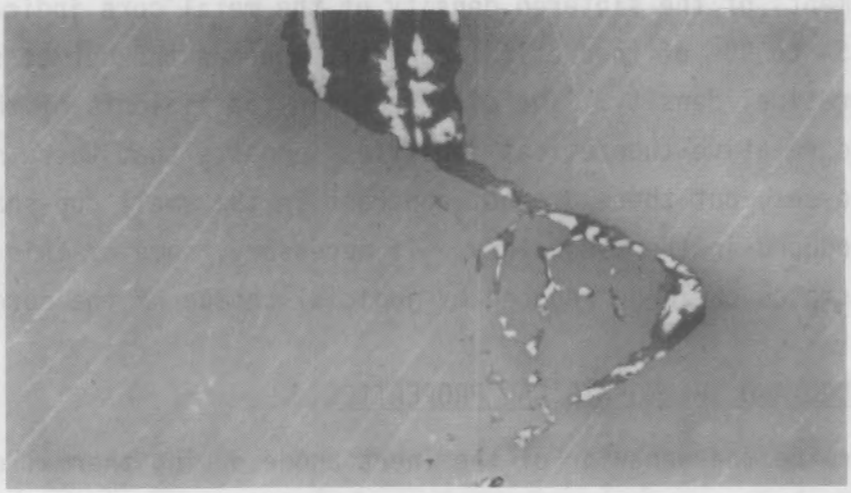

100X

20X

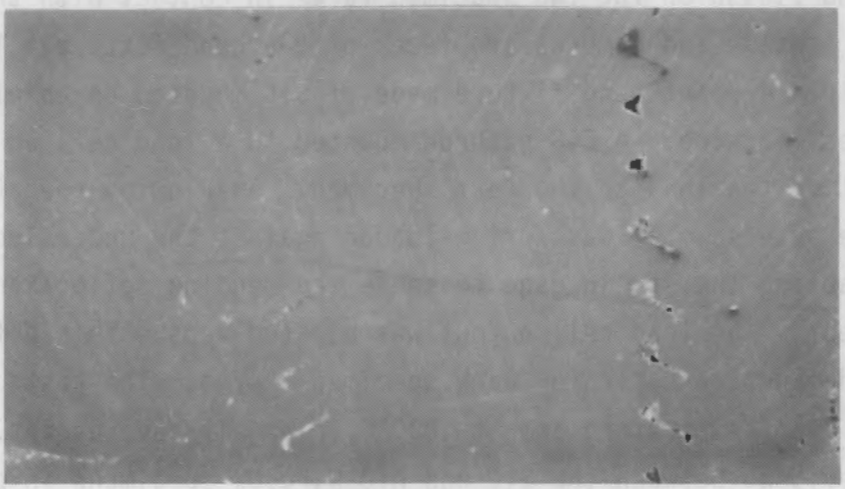

13X

FIGURE 3.9. Anode 152

Measurements of the sintered density of the metal core indicate that the density is 85% to 90% of theoretical density, whereas the cermet sinters to >95% of theoretical density. The difference in coefficients of thermal expansion and relative theoretical densities suggests that there may be internal stresses, but these are not apparent in the small cup-shaped anodes currently produced in the laboratory. If necessary, some of this thermal expansion mismatch could be reduced by judicial choice of the core alloy.

3.3 MECHANICAL AND THERMOPHYSICAL PROPERTIES

To determine the behavior of the inert anode during thermal events, the thermal and mechanical properties were studied. These mechanical and thermal data were used as input to the finite element analyses.

3.3.1 Mechanical Properties

Cermet flexure strengths and bending moduli were determined by means of a 4-point bending test procedure.

3.3.1.1 Experimental Methods

Bars in the form of rectangular parallelepipeds [4.9 mm (0.19 in.) x 3.5 mm (0.14 in.) x 50 mm (2.0 in.)] were machined from NiO-$NiFe_2O_4$-17% Cu material processed in the usual fashion (Marschman and Davis 1987). The material had a final density of 6.02 x 10^3 kg/m^3. The bars were polished to a 6-μm diamond finish on the two specimen faces in contact with the roller pins and the tensile and compressive faces of the bend fixture. The bars were tested in a 4-point bend fixture made of SiC mounted on an electro-mechanical test machine. A SiC pushrod mounted to a load cell on the cross-head transmitted the load to the test specimen. An alumina rod attached to a strain gage extensometer was spring-loaded against the underside of the bend bar, enabling the strain gage to sense the bending deflection of the bar during the test. The load cell output was plotted versus this deflection to give a load-deflection curve for each specimen tested. The tests were performed at room temperature and at 1000°C in an air environment. There was no reaction evident between the SiC and NiO-$NiFe_2O_4$ specimens in post-test examination of the high-temperature test specimens. Some surface oxidation of the specimens occurred during the tests; however, the anodes will be in

contact with an oxidizing environment in actual use, so this was not considered to be a serious deficiency of the test procedure. Obviously, time at temperature could have a profound effect on mechanical properties, but investigation of this variable was beyond the scope of this limited investigation.

3.3.1.2 Technical Progress

A total of thirteen specimens were tested, nine at room temperature and four at 1000°C. Of the nine tested at room temperature, six failed under the loading pins of the 4-point bend fixture and three failed in the center of the span. Only the data from the three specimens that failed in the center of the span are valid. A 4-point flexure strength of 97.7 MPa ±3.5 MPa (one standard deviation) was determined for the material at room temperature. The bending modulus at room temperature was 109 GPa ±14 GPa (one standard deviation). These measurements were in good agreement with published Alcoa data (Weyand et al. 1986).

Bend tests conducted at 1000°C revealed that the NiO-$NiFe_2O_4$-17% Cu material was very ductile (plastic) at this temperature. Failure did not occur because the specimens deformed to the limits of the bend fixture, which corresponds to a deflection of 0.5 mm (0.02 in.) Therefore, no strength data are available for 1000°C. However, a stress of about 30 MPa (corresponding to a maximum tensile fiber stress) was required to cause significant plastic flow. It must be realized, however, that these were short-term tests, and that creep, or time-dependent flow properties, cannot be reliably inferred from these data.

3.3.2 Thermophysical Properties

Thermal diffusivities and thermal expansions of the NiO-$NiFe_2O_4$-17% Cu cermet material were needed for a finite element analysis of the stresses in a cermet anode. Specimens for testing were cut from a larger piece of NiO-$NiFe_2O_4$-17% Cu material (the same piece used for the thermophysical property specimens) that had been mixed, pressed, and sintered in the usual manner. Measurements were made at the Thermophysical Properties Research Laboratory, Purdue University (see Appendix).

3.3.2.1 Experimental Methods and Materials

Bar and disk specimens of NiO-$NiFe_2O_4$-17% Cu cermet were prepared for testing. The bars used for the thermal expansion measurements were 50 mm (2 in.) x 4.8 mm (0.19 in.) x 4.8 mm (0.19 in.); the disks used for the thermal diffusivity measurements were 12.7 mm (0.5 in.) in diameter x 3.8 mm (0.15 in.) thick. All of the tests were performed in air.

Thermal diffusivity data were obtained by the laser flash method, in which a pulse of energy is delivered with a laser to one face of the disk specimen and the temperature rise on the other face is measured as a function of time. The results are then calculated from the thermal response of the face opposite the face to which the thermal pulse was delivered. This measurement was repeated at 100°C intervals between room temperature and 1000°C. After the test a thin surface oxide coating was observed on the specimens. This thin coating was not expected to have a significant effect on the results of the tests.

Thermal expansion properties were measured using a dual pushrod dilatometer. In this apparatus, the differential expansion is measured between a standard from the National Institute of Standards and Technology and the test specimen as a function of temperature. Eighteen preselected temperatures between room temperature and 1000°C were used in this series of measurements, nine of which were also used for measurements taken on cooling the specimen. Absolute expansions and average expansions are reported. The average value is then calculated by dividing the absolute value by the change in temperature between room temperature and the temperature of measurement.

3.3.2.2 Technical Progress

Results from the thermal expansion and thermal diffusivity are reported in Tables 3.2 and 3.3, respectively.

The thermal expansion results are shown in Figure 3.10. There is good agreement between the values obtained on heating and cooling the specimen.

TABLE 3.2. Thermal Expansion Results

Phase	Temperature, °C	Expansion, μm/m	Average Coefficient, 10^{-6} μm/m-°C
Heating	21	0	
	147	1,253	10.3
	197	1,804	10.3
	247	2,498	11.1
	297	3,106	11.3
	347	3,718	11.4
	397	4,363	11.6
	447	5,041	11.8
	497	5,748	12.1
	547	6,496	12.3
	597	7,294	12.7
	647	7,971	12.7
	697	8,601	12.7
	747	9,215	12.7
	797	9,836	12.7
	847	10,510	12.7
	897	11,200	12.8
	947	11,920	12.9
	997	12,760	13.1
Cooling	947	12,030	13.0
	897	11,250	12.8
	847	10,540	12.8
	797	9,876	12.7
	747	9,228	12.7
	697	8,588	12.7
	647	7,939	12.7
	597	7,256	12.6
	547	6,449	12.3

TABLE 3.3. Thermal Diffusivity Results

Phase	Temperature, °C	Diffusivity, $cm^2\ s^{-1}$
Heating	23	0.0258
	100	0.0221
	200	0.0184
	300	0.0167
	400	0.0160
	500	0.0155
	600	0.0142
	700	0.0140
	800	0.0135
	900	0.0129
	1000	0.0127
Cooling	200	0.0192

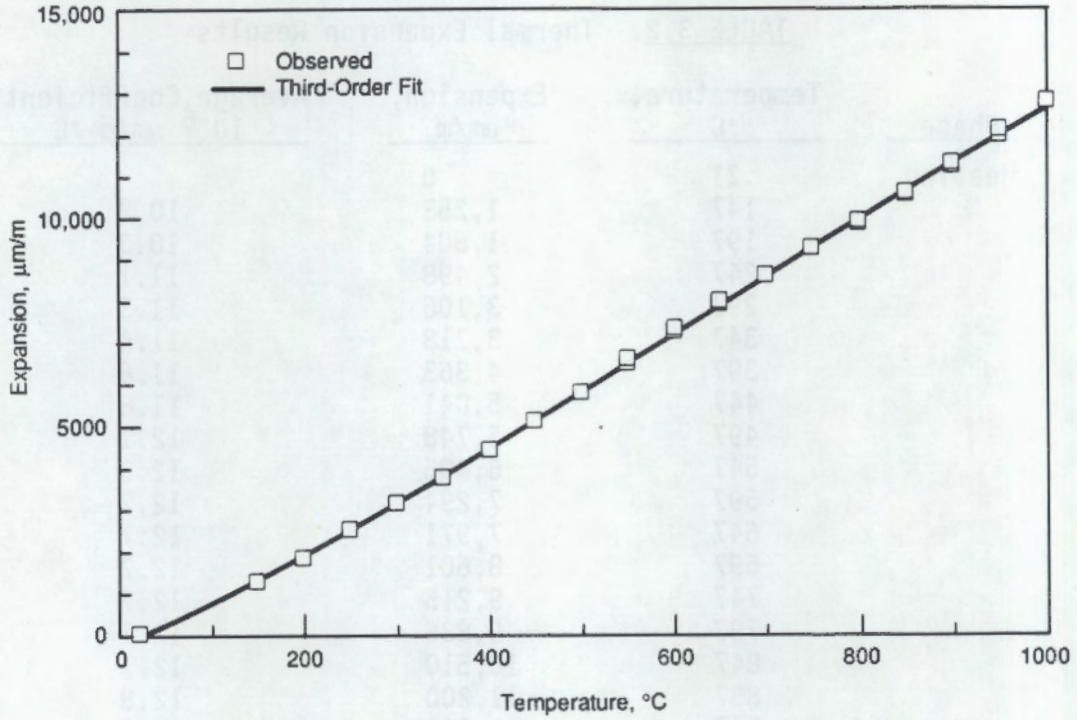

FIGURE 3.10. Thermal Expansion of NiO-$NiFe_2O_4$-17% Cu Anode Material

In Figure 3.11, the difference between adjacent expansion data divided by the change in temperature in degrees Celsius is plotted against the mean temperature for the two expansion data. For example, the expansion at 347°C (3718 µm/m; see Table 3.2) is subtracted from the expansion at 397°C (4363 µm/m). The difference (645 µm/m) is divided by 50°C (645 µm/m/50°C = 12.9 µm/m-°C) and plotted at a mean temperature of 372°C. With this method, changes in thermal expansion caused by phase changes and other phenomena that affect the thermal expansion of a solid can be readily detected. Thermal expansion data for the NiO-$NiFe_2O_4$-17% Cu material have been treated in this manner and plotted in Figure 3.11.

Two maxima are seen in the data shown in Figure 3.11. It is not known what change caused the peak at about 200°C. The peak at about 550°C appears to be due to a magnetic transition, according to the Purdue University studies. The data in the 800 to 1000°C range suggest the onset of another transition, perhaps structural.

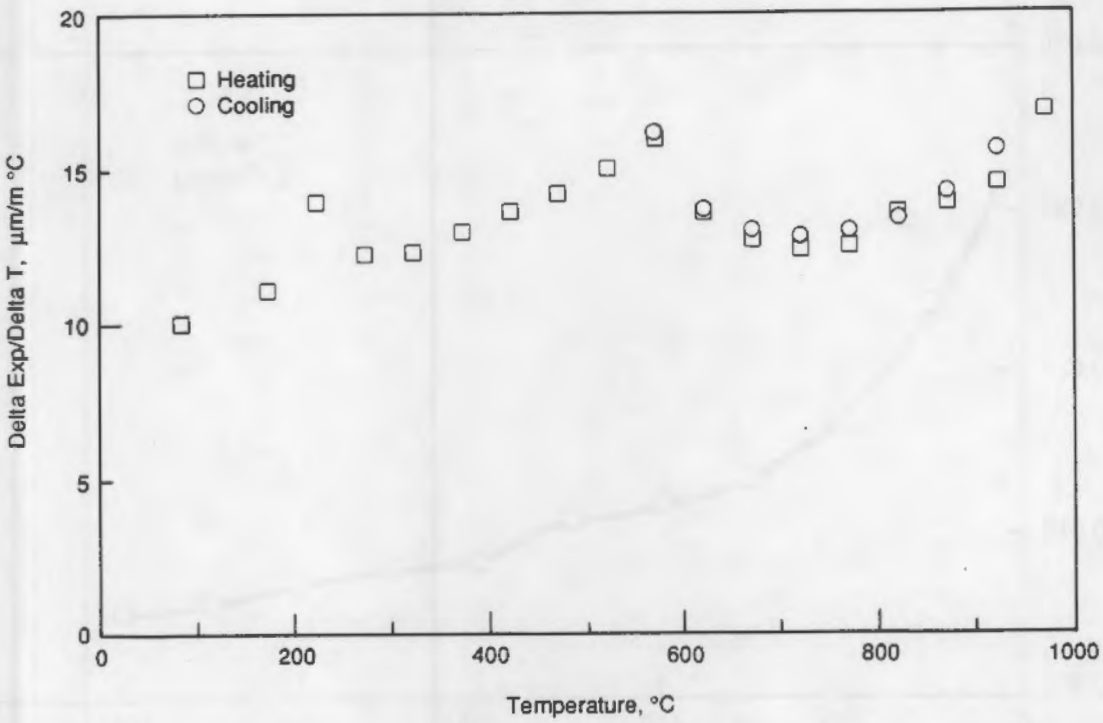

FIGURE 3.11. Thermal Expansion Data for NiO-$NiFe_2O_4$-17% Cu Anode Material

The thermal diffusivity results are shown in Figure 3.12. Again, there is good agreement between the values at 200°C taken on heating and cooling the specimen. The inflection at about 550°C was interpreted in the Purdue work as being due to the magnetic transition. However, there have been no independent measurements of the magnetic transition in this material.

3.4 FINITE ELEMENT ANALYSES

Finite element analyses were performed to better understand the behavior of a large cermet anode during several different thermal events and to determine, if possible, what thermal heating or cooling rates could be tolerated before induced stresses caused cracking.

All analyses were axisymmetric, and two-dimensional modeling was used to facilitate the level of computational effort involved in arriving at solutions. Figure 3.13 is used here to describe some of the modeling assumptions used. The outside bottom radius of the model shown is 2.5 cm (1.0 in.). The

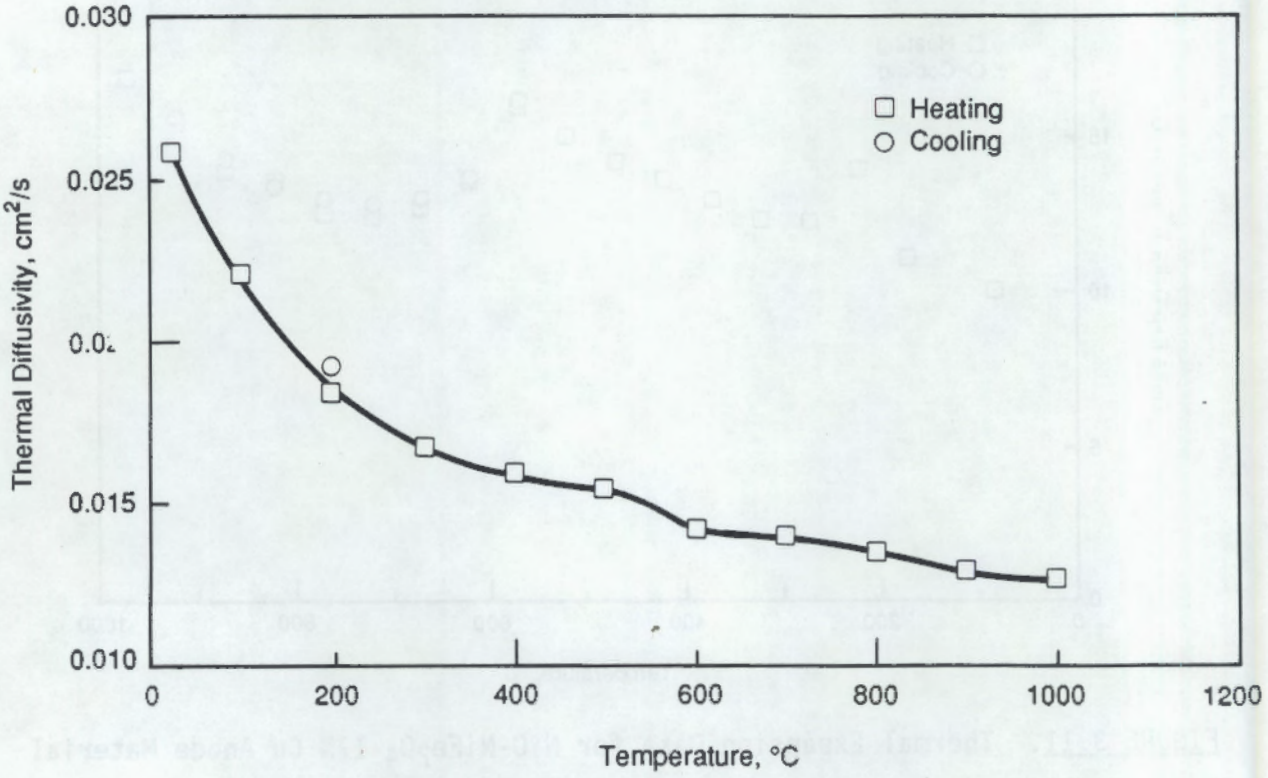

FIGURE 3.12. Thermal Diffusivity

only difference between this geometry and the other two geometries studied was this radius. Other values were 1.27 cm (0.5 in.) and 0.64 cm (0.25 in.). Line AL represents the axis of symmetry of the model. Other lettered line segments will be used to describe boundary conditions imposed on the model.

The model contains four materials indicated by circled numbers. Material 1 is the cermet material (NiO-$NiFe_2O_4$-17% Cu). Material 2 is an alloy of 65% Cu and 35% Ni. This material is assumed to be theoretically dense and rigidly bonded to both the cermet material and the Ni cylindrical bar, Material 3. Material 4 is powdered alumina, which is used to protect the electrical connection from cryolite vapors and is primarily significant only in the thermal modeling. Negligible structural stiffness was assumed for Material 4 in the structural modeling. The thermal and mechanical properties were discussed in Section 3.3 and from Weyand et al. (1986)

The ANSYS finite element code (DeSalvo and Gorman 1987) was used for both thermal and structural analyses of the models considered. Identical

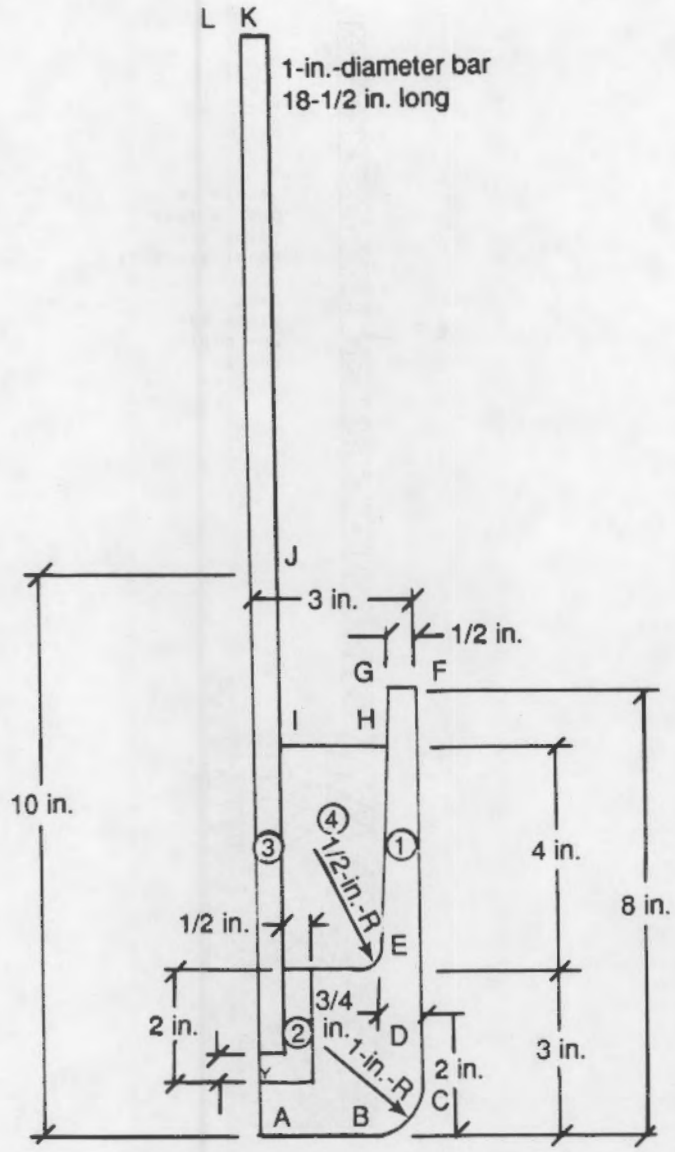

FIGURE 3.13. Typical Anode Geometry

mesh configurations were used for thermal and structural models. Triangular elements were employed to facilitate modeling of irregular boundaries. The mesh used for the 2.5 cm (1 in.) bottom radius model is shown in Figure 3.14.

A total of six temperature configurations were used to compute thermal stresses for each of the three slightly different geometries considered. These six cases (referred to as steps in the attached figures) appear to represent the thermal history of preheating the electrodes, transferring the

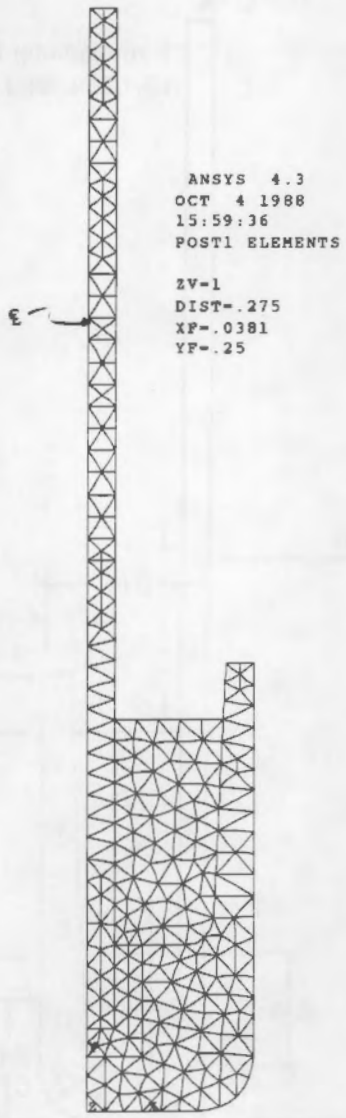

FIGURE 3.14. Typical ANSYS Finite Element Geometry

electrode to the electrolyte cell, and allowing steady-state temperatures to develop after immersion. A description of boundary conditions used for these six steps follows:

- Step 1--This load case is intended to represent steady-state temperatures of the electrode when it is in the pre-heat oven. It was assumed that temperatures along line LK (Figure 3.13) were maintained at 40°C. This condition along LK was maintained throughout all six steps. Free convection was assumed to occur along line ABCDEFGHIJK. The convection coefficient used for this was 5 Btu/(h-ft^2-°F), which corresponds to 0.00677 Kcal/s-m^2-°C. While convection coefficients are quite variable, this value was quoted in Kreith (1965) as being typical. Bulk

temperature (the air temperature exterior to the relevant boundary layer) was assumed to be 1000°C along line ABCDEFGHIJ. Along JK the bulk temperature was assumed to vary linearly from 1000°C to 40°C. The boundary along the center line was assumed to be insulated because of its symmetry.

- Step 2--This load case represents a transient temperature simulating removal of the electrode from the preheat oven. Initial conditions are taken from those temperatures calculated in Step 1. It was assumed that free convection (with 40°C bulk temperature) existed on the exposed surfaces of the electrode. The convection coefficient used was the same as that used in Step 1.

- Steps 3, 4, and 5--These cases represent "snap shots" of a thermal transient resulting from immersing the anode (initially at the temperatures) calculated in Step 2 into the cryolite bath. Boundary conditions along line ABCD were step changed to 1000°C. This step change is most likely more severe than what would occur in actual practice since the cryolite has finite thermal conductivity and specific heat. Along line DE, the surface was assumed to be insulated. This is where the bath crust is assumed to reside, and it was assumed that a small air space separated the media. Along line EFGHIJK, a free convection (convection coefficient equal to that used in Step 1) was assumed. The bulk temperature was assumed to be 1000°C at point E and to vary linearly with axial position to 40°C at point K. Line LK was assumed to be maintained at 40°C. Steps 3, 4, and 5 correspond to 1000, 2000, and 3000 s, respectively, into the transient event.

- Step 6--This load step utilized the same thermal boundary conditions as Steps 3, 4, and 5. It was a steady-state simulation and would represent the temperature distribution during continuous operation. Temperatures of Steps 5 and 6 were noticed to be only slightly different; i.e., steady state was almost reached in 3000 s.

Structural analyses were performed for all six temperature distributions corresponding to the steps above. The structural boundary conditions assumed that the electrode was supported in the axial direction from line LK. However, radial expansion along LK was allowed. A stress-free temperature must be assumed for the anode since the materials were assumed to have different expansion coefficients. For purposes of this effort, that temperature was assumed to be 50°C. Initial stresses, due, for example, to nonuniform shrinkage during electrode fabrication, were neglected. However, these stresses are expected to be minimized during processing because of the slow cooling rate used in processing.

The material properties used in the thermal and structural finite element analyses of this study are given in Table 3.4 along with their sources. It should be emphasized that all properties were assumed homogeneous, isotropic, and independent of temperature. A more thorough description of thermal and mechanical properties is given in Section 3.3.

Thermal and structural results for the three (slightly different) electrode designs and for the six load steps considered were generated. Little difference in the structural results was noticed for each of the three different geometries analyzed. In addition, the structural results for each of the six load cases were similar. Thermal and structural results for the geometry shown in Figure 3.13 and for load step 6 (steady-state electrolyte immersion) are shown in Figures 3.15 through 3.18. Figure 3.15 shows the thermal results for the entire model including the nickel bar, and Figure 3.16 is an enlarged view of temperature variation in the electrode body. Heat flow (the direction normal to the temperature contours) into the cermet base and up the nickel bar can be seen readily. The sparsity of contour lines in the insert region is consistent with its high thermal conductivity.

Two stress parameters were plotted for the above load case. The first parameter was the maximum principal stress, Figure 3.17. Maximum principal stress is often used as a design criterion (or failure criterion) for brittle materials. The second stress parameter, Figure 3.18, represents what is generally referred to as equivalent stress. Equivalent stress is often used as a design criterion for structures made from ductile materials and is approximately proportional to shear stress intensity. Only the central portion of the electrode shown had any significant stress.

Stress levels were quite consistent for all cases (steps and geometries) studied. For the cermet material, the maximum principal stress was seen to be approximately 300 MPa (about 43.5 ksi). The corresponding maximum cermet equivalent stress was about 500 MPa (72.5 ksi). Both of these maximums were near the insert interface. Both of these stress levels can be assumed to exceed the high-temperature strength of the cermet material. Due to the high temperatures at which these stresses occur, however, substantial yielding (and hence stress falloff) is likely. It is interesting to note that, based

TABLE 3.4. Material Properties

	Property	Cermet	65% Cu, 35% Ni	Nickel Bar	Alumina Powder[a]
E	Young's modulus (Pa)	1.12E11 (1)	1.51E11 (2)	2.14E11 (2)	1.0E8 (assumed)
υ	Poisson's ratio	0.3 (assumed)	0.342 (2)	0.3 (2)	0.3 (assumed)
G	Modulus of rigidity (Pa) (calculated)	0.43E11[b]	0.56E11 (2)	0.82E11 (2)	0.3 (calculated)
ρ	Density, kg/m^3	6.0E3 (3)	8.9E3 (2)	8.9E3 (2)	3.0E3 (2)
α	Coefficient thermal expansion, $°C^{-1}$	11.5E-6 (3)	15.38E-6 (2)	13.3E-6 (2)	6.3E-6 (2)
K	Thermal conductivity, $K_{cal}/m\ s\ °C$	2.09E-3 (3)	6.9E-2 (2)	2.1E-2 (2)	1.4E-3 (2)
C	Specific heat, K_{cal}/kg	0.2 (4)	0.0969 (2)	0.106 (2)	0.27 (2)

(a) Properties (except E) are for solid alumina. Reduced 30% for K, ρ.
(b) Calculated from E and υ.
(1) Personal Communication with C. H. Henager, PNL.
(2) Bulz 1970.
(3) Taylor and Groot 1988.
(4) Weyand et al. 1986.

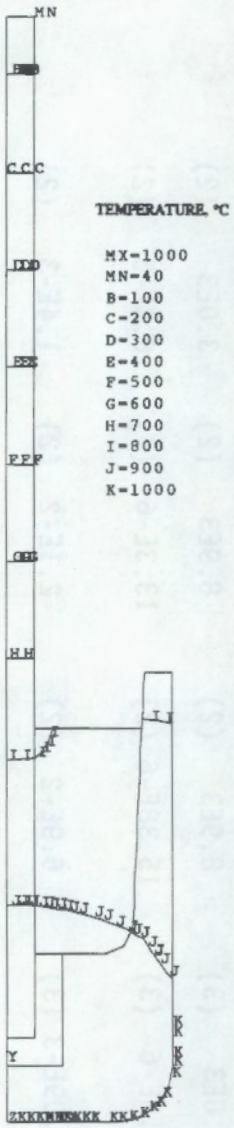

FIGURE 3.15. Steady-State Temperature Distribution After Electrolyte Immersion -- Entire Model

on the value of Young's modulus assumed, the above stress levels correspond to 0.26% and 0.44% strain, respectively. Most likely, the material has sufficient high temperature ductility to tolerate this level of straining (Section 3.3.1.2).

The insert material was seen to have higher stress levels than the cermet material. Of particular interest is the high level of SIG1 (contour level I) observed at the top surface. Plotting individual stress components (plots not shown) showed that this high level was caused by large tensile

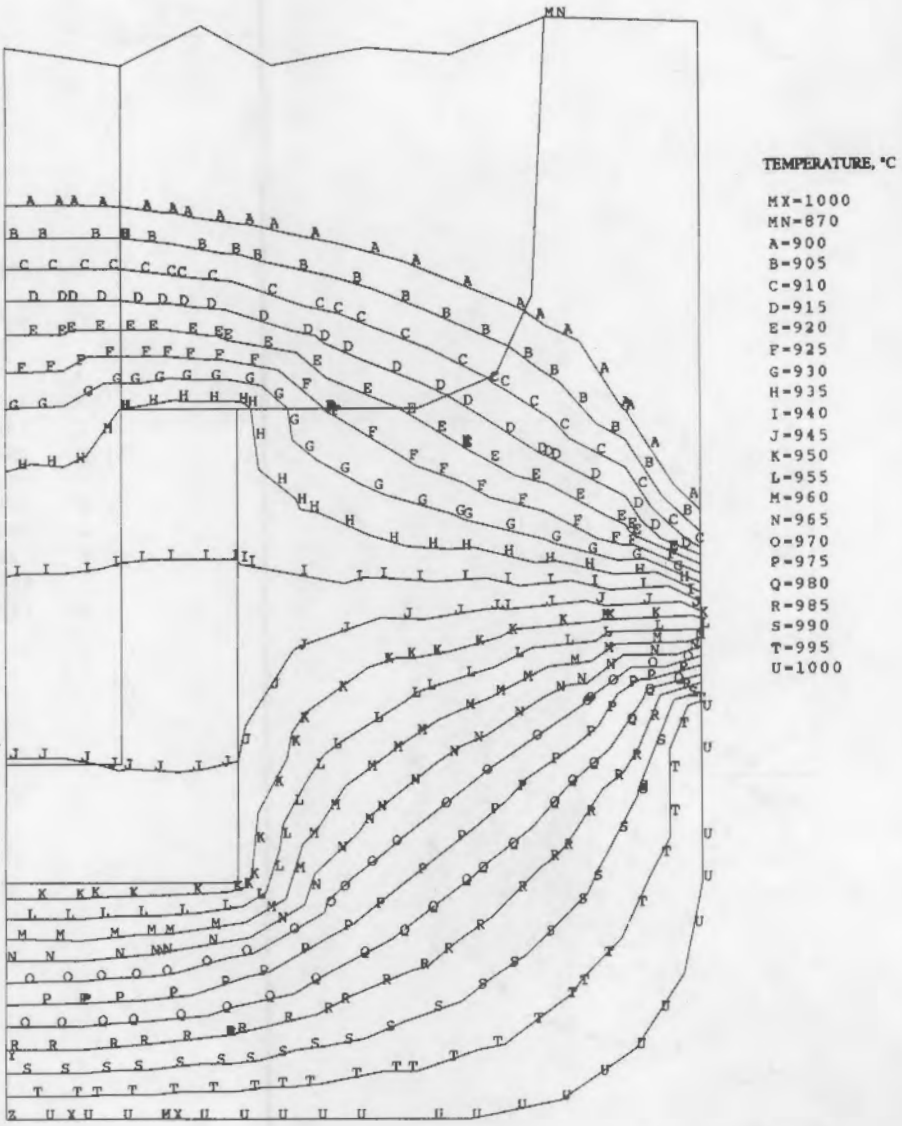

FIGURE 3.16. Steady-State Temperature Distribution After Electrolyte Immersion -- Electrode Body

radial stresses. Apparently, the insert material is trying to expand radially (more so than the nickel bar) and the nickel bar, which has a large radial stiffness due to small size, is holding it in. As with the cermet material, yielding (assuming it occurs) will tend to reduce these values.

Whether or not the stress levels are sufficient to cause a problem has not been determined. There are too many material property uncertainties for an accurate assessment. If initial testing of prototypes indicates a problem, however, the following actions might be considered.

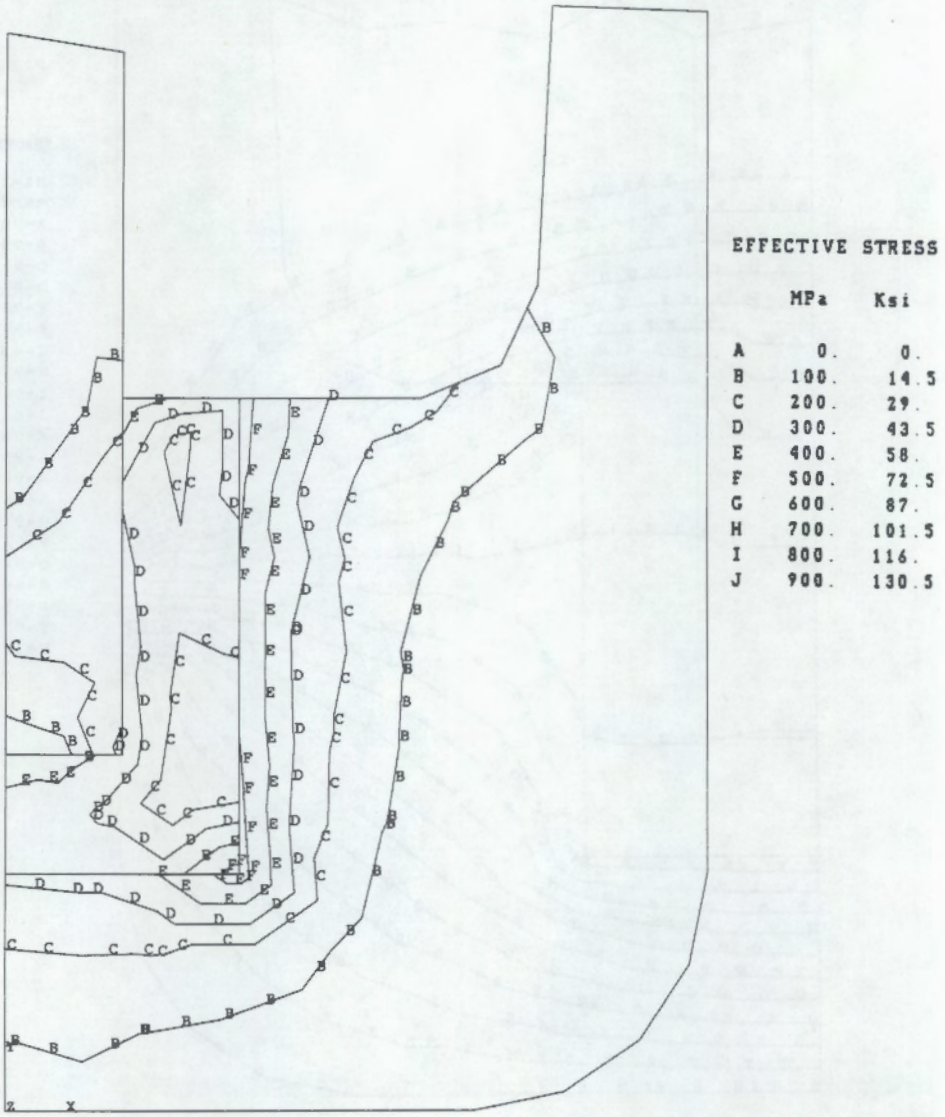

FIGURE 3.17. Steady-State Effective Stress After Electrolyte Immersion

1. Strive to keep coefficients of thermal expansion values of the various materials as close as possible. The mean CTE between stress-free conditions (assumed to be room temperature) and operating temperature (about 960°C in this case) should be used.

2. Preheat the anode very slowly. During the initial stages of preheat, ductility of the materials is likely to be much less than at operating temperatures, so yielding to accommodate thermal stresses will be much more difficult.

3. Try to avoid thermal cycling. If high-temperature yielding occurs, then thermal cycling could cause low-cycle fatigue damage problems.

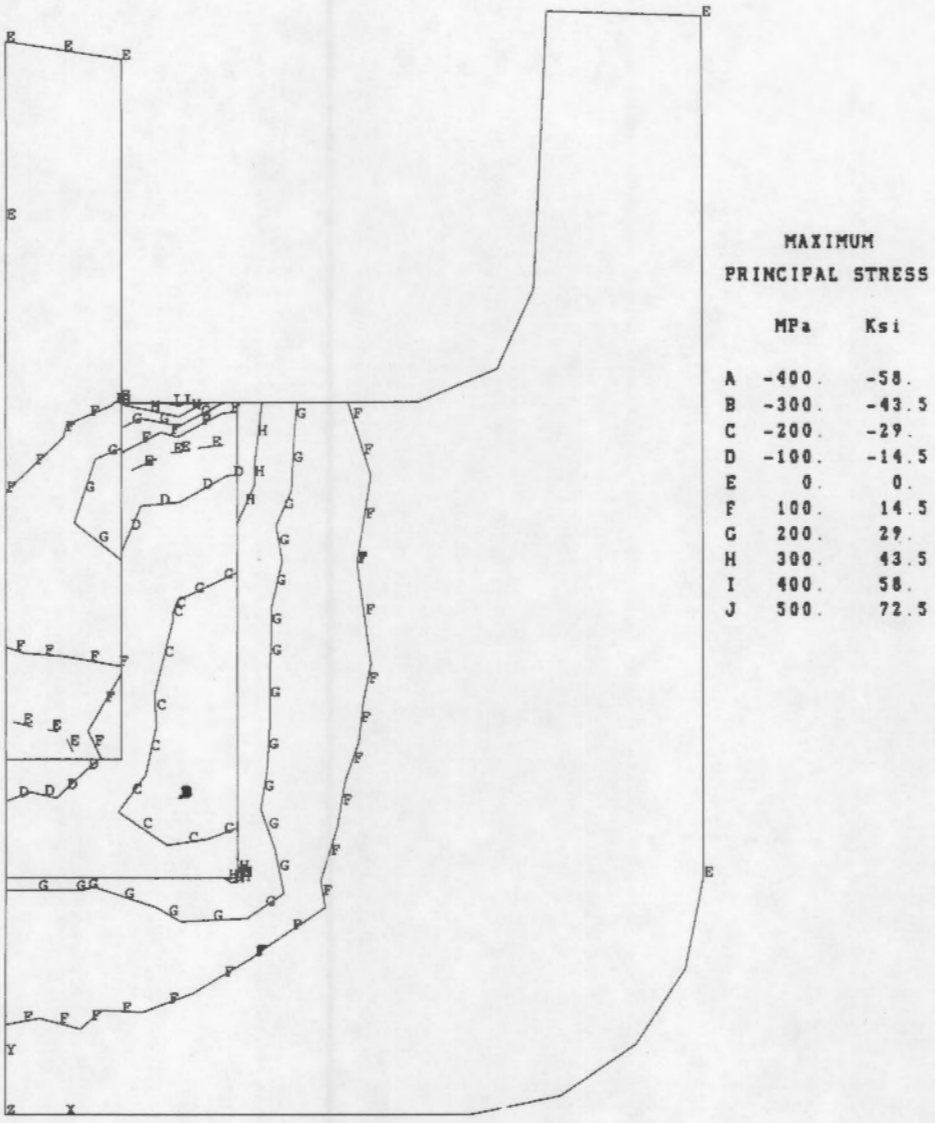

FIGURE 3.18. Steady-State Maximum Principal Stress After Electrolyte Immersion

4.0 ANODE PERFORMANCE

4.1. CONFIRMATION TESTING

Research performed in FY 1988 focused primarily on the evaluation of cermets based upon the two-phase oxide system NiO-$NiFe_2O_4$, containing a third, electrically conductive metal phase composed primarily of Cu or Cu/Ni alloy. The development of NiO-$NiFe_2O_4$-Cu-based cermet nonconsumable anodes at PNL also was continued in FY 1988. Research indicated that the NiO-$NiFe_2O_4$-Cu-based cermets are potentially viable as nonconsumable anodes for use in the electrolytic production of Al. This conclusion is supported by the results of successful laboratory-scale testing at PNL. High-purity Al was repeatedly produced in laboratory-scale cells, and several anodes were operated virtually free of degradation in 20-h tests.

As previously documented (Marschman 1989), these successful results were obtained by operating the experimental electrolysis cells at conditions slightly different from those found in commercial reduction facilities. Because a resistive "film" that appears to protect the non-consumable anodes was found, it was determined (for the present at least) that the experimental electrolysis cells had to be operated at lower anode current densities than found in commercial reduction cells. A process control device was developed for monitoring the performance of nonconsumable anodes in FY 1987, and this device was used during most of the experiments performed in FY 1988. Analysis of data obtained with the process control device led to the development of a rudimentary system of control, which has been used to correct conditions adverse to successful anode operation.

Research conducted during FY 1987 produced new technical developments and discoveries, and this research was expanded upon in FY 1988. Anode operating environments were explored to investigate the range of cell conditions that might be possible in commercial reduction facilities. These efforts are described in detail below.

Testing of nonconsumable anode materials involved the use of laboratory-scale electrolysis test cells. The principal goal of the laboratory-scale testing effort was to evaluate nonconsumable anode performance as a function

of electrolyte chemistry. Ten experiments were performed during FY 1988. The design of the electrolysis cell used to conduct these tests was described in a previous report (Hart et al. 1987).

4.1.1 Data Analysis

The data collected from each of the experiments is tabulated in Table 4.1. All tests were performed using alumina saturated baths lying in the temperature range 965 to 970°C. Although each experiment was performed with specific goals, of primary interest in each test was the resulting Fe, Ni, and Cu impurities in the electrolytically produced Al. The impurity data for those elements [determined by inductively coupled plasma (ICP) spectroscopy] listed in Table 4.1 are corrected for the impurities introduced by the Al "seed" plates that were used in each experiment. Sources of Fe, Ni, and Cu impurities other than the anodes could not be quantified, as total mass balances for the electrolysis cells used in this testing effort could not be determined. Thus, the Fe, Ni, and Cu impurities found in the electrolytically produced Al may not have been derived entirely from degradation of the anodes. It should also be noted that the concentrations of these metals in the electrolyte are well below the saturation values reported by Baker (1983).

The impurity data were statistically analyzed to determine if any relationships between the experiments could be developed. The statistical analysis consisted of the following steps. First, the impurity data were divided into three sets: Fe impurities, Ni impurities, and Cu impurities. The N-1 standard deviation and sample mean was then calculated for each data set. Next, the individual data points from each data set were subjected to a Chauvenet's Criterion (Holman 1978)[a] test for acceptance or rejection. Each data set had only one data point that could not meet Chauvenet's Criterion, and those data points were rejected.

(a) Suppose N measurements of a quantity are taken and that the results follow the gaussian error distribution. Chauvenet's Criterion is used to eliminate those data points that have a small expected probability of occurrence, hence reflecting unacceptable experimental error. It specifies that a reading may be rejected if the probability of obtaining that particular deviation from the mean is less than 1/2N.

TABLE 4.1. Accumulated Data for Test Performed on NiO-$NiFe_2O_4$-Cu-Based Cermet Anodes, FY 1988

Exp. #	Anode Number	Duration h	Current Amps	Anode Current Density A/cm2	Aluminum Produced GMS	Coulombic Efficiency	Bath Ratio	AlF3	Al2O3	CaF2	MgF2	LiF	wt% Fe in Al Metal	wt% Ni in Al Metal	wt% Cu in Al Metal	wt% Fe in bath	wt% Ni in bath	wt% Cu in bath	Success or Failure	Comments
68	138-H-1	20.0	12.0	0.5	Unmeasur-able	---	1.35	3.77	7.35	2.71	0	0	ICP #'s not usable		---	ICP not performed		---	Success	Cup-shaped anode, slight edge wear
67	111-12	20.0	10.0	0.5	46.2	70%	1.35	3.77	7.35	2.71	0	0	1.226	0.194	0.055	ICP not performed		---	Success?	ICP numbers questionable, no wear on anode
66	133-2	20.0	10.0	0.5	58.9	88%	1.35	5.15	6.25	2.74	0	2.0	0.227	0.045	0.517	0.024	0.016	0.049	Partial success	Al anode, round bottom, single blister
65	131-1	20.0	10.2	0.5	51.4	76%	1.35	3.73	6.75	4.2	0	0	0.246	0.016	0.135	0.028	0.011	0.080	Success	High alloy Cu/Ni anode, round bottom
64	102-2	20.0	10.0	0.5	42.3	64%	1.35	3.98	5.0	1.4	0	0	0.361	0.021	0.134	0.010	0.001	0.003	Success?	Al anode, slight edge wear
63	104-2	20.0	10.1	0.5	63	92%	1.35	3.81	5.0	5.5	0	0	0.200	0.017	0.126	0.019	0.004	0.014	Success?	Al anode, slight edge wear, anode cracked before test
62	109-6	20.6	10.1	0.5	65	93%	1.35	3.23	5.0	0	0	2.0	0.136	0.021	0.096	0.054	0.019	0.038	Success	Slight discoloration
61	109-4	20.5	10.3	0.5	50	71%	1.35	3.7	8.0	5.0	0	0	0.064	0.003	0.014	0.018	0.018	0.035	Success	No Wear
60	115-25, 115-26	18.25	20.0	0.5	61.5	50%	1.15	9.5	8.0	4.0	0	0	0.012	0.003	0.072	0.012	0.024	0.069	Success	2 round-bottomed anodes
59	114-24	12.0	10.2	0.5	21.5	53%	1.35	3.7	8.0	5.0	0	0	0.710	0.052	0.134	0.012	0.018	0.018	Success	Round-bottomed anodes
										ADJUSTED AVERAGES:			0.245	0.022	0.096	0.018	0.014	0.038	

After the application of the Chauvenet's Criterion test to the data sets, new, adjusted N-1 standard deviations were calculated for the adjusted data sets. Additionally, adjusted sample means and sample variances were calculated. The adjusted sample means are given in Table 4.1 at the bottom of each data set.

Performance of these calculations provides the basis for data comparisons. Once data are accepted or rejected, the task of determining what significant information are in the data is made easier. Statistically analyzing the available data also prevents "data bias" and deters any attempt to extract more information from the data than is possible. The data analyses can be used to support several observations discussed in the following sections.

4.1.2 NiO-$NiFe_2O_4$-17% Cu Round-Bottomed Anodes

Research performed in FY 1987 indicated that square-edged, right cylindrically shaped anodes exhibited wear at the edges. It was postulated that the protective "film" that forms during anode operation might be "shape sensitive." That is, there might be a critical radius for film adherence to the anodes. Several sintered NiO-$NiFe_2O_4$-17% Cu anodes were submitted to the PNL optical shops for machining. The anode bottoms were rounded using diamond-tipped tools. These anodes were used in two tests, numbers 59 and 60, as listed in Table 4.1.

Test 59 was performed using a 1.35 bath ratio electrolyte formulated to contain 8 wt% alumina at saturation. This test and Test 60 were used to evaluate the possibility of placing the cell on "idle" during offsite hours in an attempt to attain >100 h of cell operation without excessive fatigue to the cell operators. Because of operating difficulties, the anode in this test was only operated for 12 h. The anode was initially immersed in the electrolyte and polarized for 7 h, then removed from the bath for the off-shift hours. The anode was re-immersed in the electrolyte after approximately 11 h of idle time. The anode was polarized for an additional 5 h and then removed from the bath for a second time. The cell was held at a temperature of 800°C or greater for a period of 121 h. As a result of the high

temperature, coupled with the corrosive cryolitic fumes, the Inconel® 601 liner used in these experiments was severely corroded. The liner failed, and the experiment was terminated.

During the entire 121-h experiment, the anode was either polarized in the electrolyte or held above the melt during idle time. A cross section of the NiO-$NiFe_2O_4$-Cu anode used in this test is shown in Figure 4.1. The anode showed virtually no signs of degradation, indicating that rounding of the anode corners could be used to mitigate the edge-degradation problems observed in FY 1987. Although the experiment was terminated because the Inconel 601 liner failed, and contamination of the electrolyte and electrolytically produced Al by the Inconel liner was suspected, the Fe, Ni, and Cu impurity levels in the Al did not fall outside the range of acceptable data. The Fe and Ni impurity levels are relatively high compared with the other experiments shown in Table 4.1, so it is possible that some corrosion products from the Inconel liner fell into the cell during operation. However, the Cu impurity level is well within the statistical average for all experiments, which indicates that the anode was not adversely affected by the cycling from electrolyte to vapor phase.

An enlarged version of the PNL laboratory testing cell was used for Cell 60, and two round-bottomed anodes were placed in parallel for this test. Both anodes were NiO-$NiFe_2O_4$-17% Cu anodes rounded in a manner identical to the anode used in Test 59. The electrolyte used in this test was formulated to have a bath ratio of 1.15, with an alumina saturation level of 8 wt%. This cell was run in a manner similar to that of Test 59 at a temperature of approximately 965°C. The anodes in this test saw a total of 18.25 h at polarization, and 114 h total exposure to the cell environment.

After an initial polarization period of 13 h, the cell-current was turned down to 0.1 A. Anode 115-25 was left immersed in the electrolyte, while Anode 115-26 was removed from the electrolyte and suspended over the melt. This was done to see what effect the electrolyte and fumes would have

---

® Inconel is a registered trademark of INCO Alloys International (Huntington Alloys), Huntington, West Virginia.

FIGURE 4.1. $NiO-NiFe_2O_4$-17% Cu round-bottomed anode used in Test 59 (Anode 115-24). Deposit on surface is frozen electrolyte.

on anodes not under a current load. After 12.5 h, Anode 115-26 was re-immersed and the current load restored. The anodes were polarized for an additional 5.75 h, then both were removed from the electrolyte. The cell temperature was reduced sufficiently to freeze the electrolyte, and the cell was left idle for one weekend. After the weekend-idle period, attempts were made to restart the cell. Unfortunately, one anode support rod failed, and corrosion products from the Inconel cell liner had fallen into the electrolyte. At this point the run was terminated.

Figure 4.2 shows cross sections of the anodes used in Test 60. Both anodes exhibited virtually no wear. The exposure to the electrolyte fumes and immersion-without-polarization periods did not cause additional corrosion of the anodes. In fact, the Al produced in Test 60 had the least amount of Ni, Fe, and Cu impurities of any test performed in FY 1988.

4.1.3 $NiO-NiFe_2O_4$-17% Cu Square-Bottomed Anodes

Two tests were run using square-bottomed, right cylindrical anodes (Tests 61 and 62). This was done to confirm the need for round-bottomed anodes. Test 61 was performed using a 1.35 bath ratio electrolyte formulated to contain 8 wt% alumina at saturation. This cell was operated at 970°C for 20.5 h. This cell experienced alumina feeding problems that were first detected by the process control device. The anode was not allowed to reach

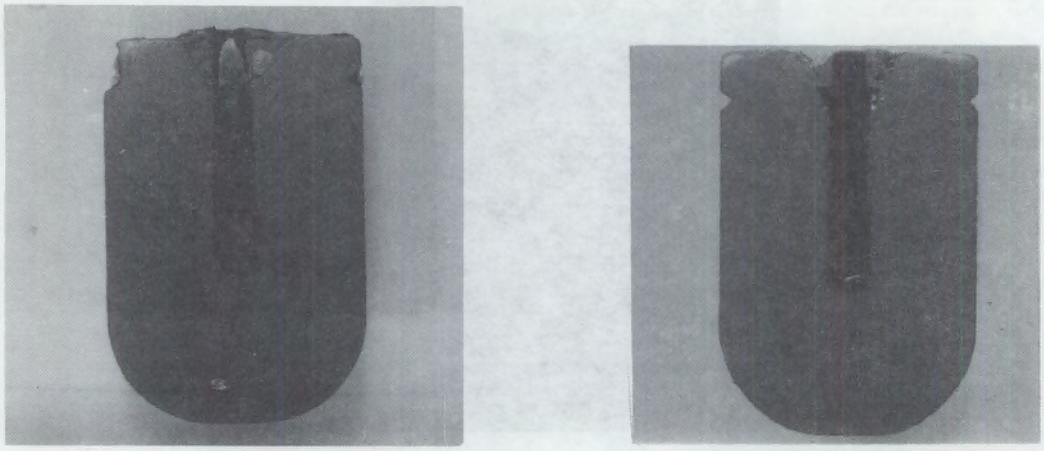

Anode 115-25 Anode 115-26

FIGURE 4.2. Two NiO-$NiFe_2O_4$-17% Cu Round-Bottomed Anodes Used in Test 60.

"upset" conditions, and a "recovery" process described by Marschman (1988) was used to restore steady cell operation. Other than the one incident of alumina "starvation," the anode performed flawlessly. A cross section of Anode 109-4 is shown in Figure 4.3. Virtually no wear was detected after 20.5 h of polarization, and the Ni, Fe, and Cu impurity levels in the electrolytically produced Al were low (see Table 4.1).

Test 62 was performed using an electrolyte with a bath ratio of 1.35 formulated to contain 5.0 wt% alumina at saturation. This test was performed at 970°C for 20.6 h. The only problem encountered during this test was a slight amount of cell sludging, which was corrected by reduction of the alumina feed rate. A cross section of this anode is shown in Figure 4.4. Although the photomicrograph does not show the condition clearly, a slight discoloration was present at the anode edge. This discoloration is an indication of corrosion processes, and the Al produced in this test had slightly higher Ni, Fe, and Cu impurities than those found in Test 61.

Although the Al metal produced in Tests 61 and 62 have Fe, Ni, and Cu impurities low enough to fall within acceptance criteria, the discoloration found on the anode from Test 61 indicates corrosion. Thus, most of the anodes used in subsequent tests had some amount of radius on the anode edges. The minimum radius required has not been determined.

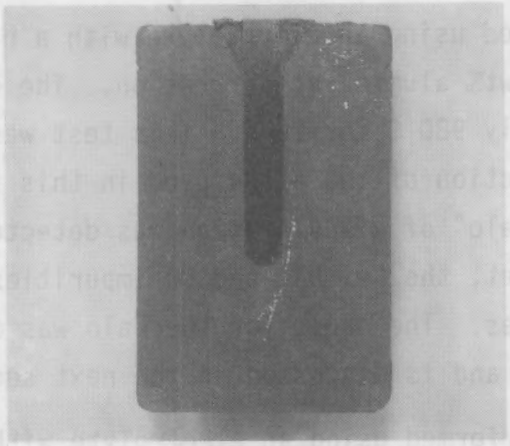

FIGURE 4.3. NiO-$NiFe_2O_4$-17% Cu Square-Bottomed Anode Used in Test 61 (Anode 109-4). Anode exhibited virtually no wear.

FIGURE 4.4. NiO-$NiFe_2O_4$-17% Cu Square-Bottomed Anode Used in in Test 62 (Anode 109-6). A slight discoloration at the anode bottom edge indicates corrosion.

4.1.4 NiO-$NiFe_2O_4$-Cu-Ni-Al Square-Bottomed Anodes

Two square-bottomed NiO-$NiFe_2O_4$-Cu-Ni-Al anodes were used in Tests 63 and 64. Square-bottomed anodes were used to determine if these high-alloy compositions were "shape-sensitive" to corrosion similar to the standard 17 wt% Cu cermet anodes. The compositions for these anodes are listed in Table 5.1 (Section 5.0).

Test 63 was performed using an electrolyte with a bath ratio of 1.35 formulated to contain 5 wt% alumina at saturation. The experiment was performed at approximately 980°C for 20 h. This test was performed without incident, and a cross section of the anode used in this test is shown in Figure 4.5. A slight "halo" of discoloration was detected around the entire surface of the anode. Yet, the Fe, Ni, and Cu impurities were within the acceptable range of values. The cause for the halo was determined after several more experiments and is discussed in the next section.

Test 64 was also performed using an electrolyte with a bath ratio of 1.35, which also contained 5 wt% alumina at saturation. This electrolyte was formulated to contain less CaF_2 than Test 63 (see Table 4.1). This test was operated 20 h at approximately 980°C. These tests also ran without incident similar to Test 63. However, this anode also exhibited a slight "halo" of discoloration around the entire perimeter of the anode (see Figure 4.6). Again, the Ni, Fe, and Cu impurities found in the electrolytically produced Al were within acceptance limits.

FIGURE 4.5. NiO-$NiFe_2O_4$-Cu-Ni-Al Square-Bottomed Anode Used in Test 63 (Anode 104-2). The anode showed a slight amount of discoloration across the entire anode surface.

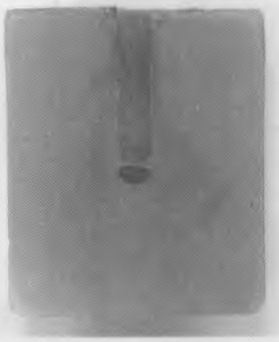

FIGURE 4.6. NiO-$NiFe_2O_4$-Cu-Ni-Al Square-Bottomed Anode Used in Test 64 (Anode 102-2). This anode showed a slight discoloration across the entire anode surface as did the anode from Test 63.

4.1.5 NiO-$NiFe_2O_4$-Cu-Ni-Al Round-Bottomed Anodes

Two tests (numbered 65 and 66) were performed using round-bottomed, high-alloy[a] cermets (composition given in Table 5.1, Section 5.0). This was done to determine if the "halo" of discolorization observed on the anodes from Tests 63 and 64 was from corrosion processes. Test 65 used an electrolyte with a bath ratio of 1.35, which contained 6.75 wt% alumina at saturation. The cell was operated for 20 h at 970°C. The cell was operated without major difficulties at an anode current density of 0.5 A/cm^2. A cross-section of this anode is shown in Figure 4.7. This anode had the same "halo" around the perimeter as found in the previous two tests, but again, the Ni, Fe, and Cu impurities fell within acceptance criteria.

Test 66 was performed using an electrolyte similar to Test 65, but was formulated to contain 6.25 wt% alumina at saturation. This test was operated for 20 h at approximately 960°C. The cell was operated without major difficulties, but in general required more attention to cell operation procedures (feeding, sludging, etc.) Although the Ni and Fe impurities were within the acceptance criteria, the level of Cu impurities was rejected because the deviation from the mean was too great according to Chauvenet's Criterion. This suggests that some process was occurring that resulted in degradation of the anode.

(a) The term "high alloy" is used to describe those anodes that contain >17 wt.% Cu with additions of up to 3 wt% Ni and up to 1 wt% Al.

FIGURE 4.7. NiO-$NiFe_2O_4$-Cu-Ni-Al Round-Bottomed Anode Used in Test 65 (Anode 131-1). Although difficult to see in this macrograph, a slight "halo" was detected around the entire perimeter of the anode.

A cross section of the anode used in Test 66 is shown in Figure 4.8. Again, discoloration around the anode perimeter was observed and can be seen at the top edge of the anode. Since the anodes from Tests 63 through 66 typically were operated without incident, and since no active corrosion processes were detected from the cell voltage or process control device, a simple dissolution process was suspected as the source of high Cu impurity level in Test 64.

Careful examination of the fabrication methods used to produce these anodes revealed that the halo observed around the anode perimeters was due to a reduction step used to prepare the anodes for brazing of the anode connection. The Ar-4% H_2 atmosphere used in the cermet reduction step leaked within the brazing furnace, resulting in the reduction of the entire anode surface to a metallic Ni-Fe-Cu-containing phase. Upon air-cooling, the anode surfaces partially oxidized, which hid the reduced layer beneath the surface. During cell operation this layer either dissolves or is attacked by some corrosion process, i.e., it either dissolves directly or the products of a corrosion reaction dissolve. If a corrosion process were active during Test 66, it went undetected. It should be noted that no process control device was used in Test 66 as it was believed that similar information provided by the device could be detected from the overall cell voltage. This assumption was incorrect if an active corrosion process was responsible for the high Cu impurity level found in Test 66.

FIGURE 4.8. NiO-$NiFe_2O_4$-Cu-Ni-Al Round-Bottomed Anode Used in Test 66 (Anode 133-2). This anode showed a halo of discoloration around the perimeter, which is visible at the top of the anode.

4.1.6 Vapor-Phase Attack of Cermet Anodes

Test 67 was performed to evaluate the effect of corrosion caused by electrolyte fumes on the above-electrolyte portion of a cermet anode. An alumina plate was machined to fit over the top of a standard 17 wt% Cu cermet anode as shown in Figure 4.9. This cell was fed alumina through a 1.27-cm (0.5-in.) diameter hole in the plate. The plate had a 2.5-mm (0.1-in.) sidewall clearance. It was expected that some of the fumes would escape. The test was performed using an electrolyte with a bath ratio of 1.35 and 7.35 wt% alumina at saturation. The cell was operated for 20 h at approximately 965°C. The cell operated smoothly, and no visible wear was detected on the anode, as shown in Figure 4.10. However, only the level of Cu impurity fell within the acceptance region of these tests. The Ni and Fe impurity levels were much higher than those found in the preceding tests. As no operating problems were encountered, and the Cu impurity level was acceptable, it is suspected that the Ni and Fe levels were the result of contamination by corrosion products formed during the test on the cell liner. Although it appears that the vapor phase found over the electrolyte does not promote excess corrosion of the anode, there is insufficient data to fully support such a claim. Confirmation of the present test results would require that a similar test be performed at a future date.

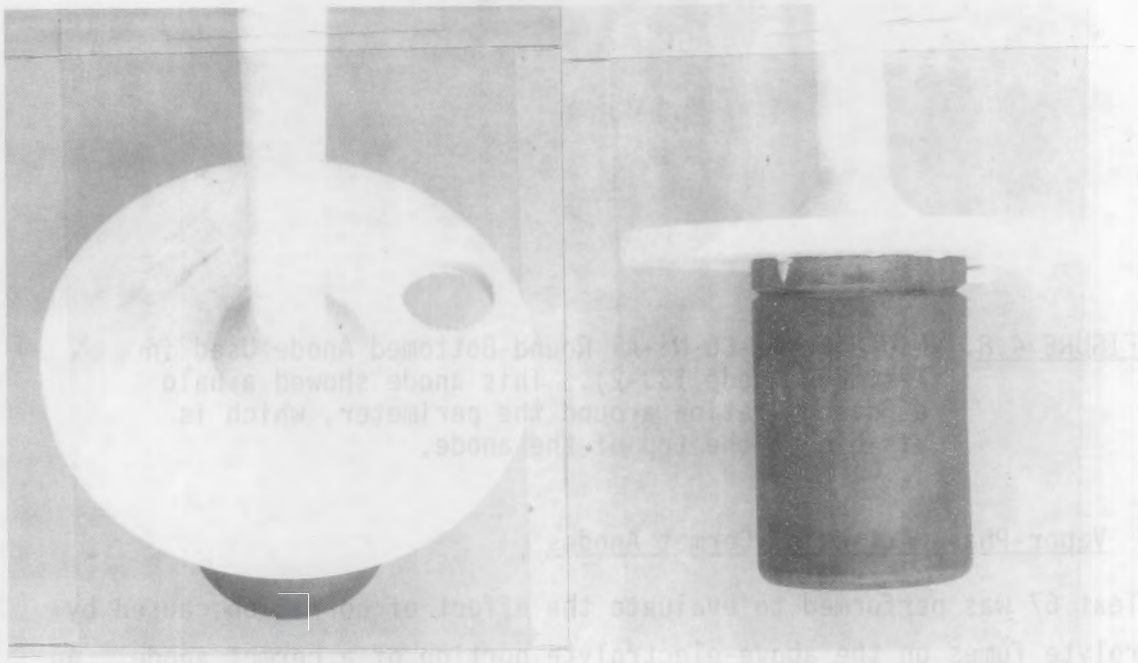

FIGURE 4.9. Alumina Plate Placed on Top on Anode Used in the Vapor Phase Attack Test (Test 67).

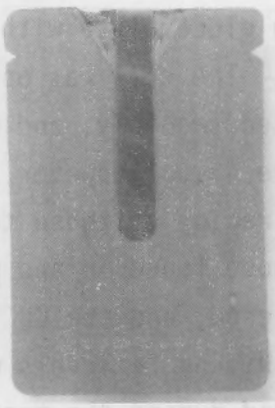

FIGURE 4.10. Standard 17 wt% Cu Cermet Anode Used in Test 67, Vapor Phase Attack Test (Anode 111-12).

4.1.7 Cup-shaped NiO-$NiFe_2O_4$-17% Cu Anode

Test 68 was used to test the first PNL-produced, cup-shaped anode (discussed in Section 5.0). The cell used in Test 68 was of a larger, but similar, design compared with those used in the preceding tests. This test employed a large cathode fixture designed to hold seven smaller TiB_2-based composite cathode samples. The cathode tests are discussed in Section 6.0.

The cell was operated using an electrolyte with a bath ratio identical to that used in Test 67. This cell was operated 20 h at approximately 965°C. A process control device was used to monitor anode performance. The cell was operated without difficulty. A cross section of the anode is shown in Figure 4.11. Because of difficulties in determining the total Al produced (as a result of the complex cathode fixture), no accurate impurity numbers could be determined. However, based on the appearance of the anode and the ease of cell operation, the impurity results would be expected to fall within the acceptance region established by the results of previous tests.

This test points out that thin-walled cermet anodes can be used successfully in small-scale tests. As a result of this test, this anode design was used in the 100-h test described in Section 4.2.

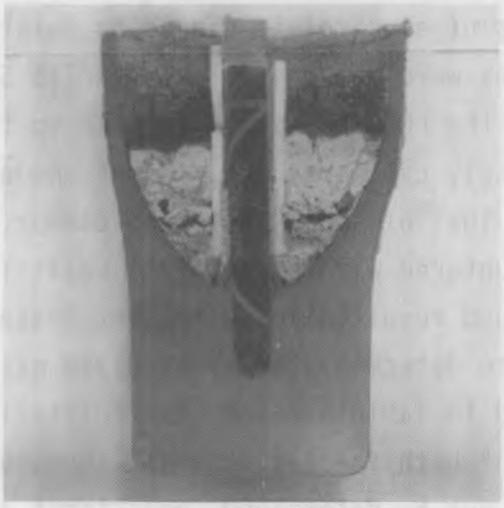

FIGURE 4.11. Cup-shaped 17 wt% Cu Cermet Anode Used in Test 68 (Anode 138-H-1). Small cracks on the inside of the anode were caused by cooldown after test completion.

4.1.8 Effect of Electrolyte Additives

Table 4.1 lists the electrolyte compositions used in each test. Two tests (62 and 66) contained 2 wt% LiF. Test 62 was mixed to contain low CaF_2 (shown as 0 wt% CaF_2). The remaining tests had varying amounts of CaF_2. The quantity of AlF_3 was selected as a function of bath ratio and the quantity of other additives. The alumina content at saturation is a function of temperature and composition.

Based on the Ni, Fe, and Cu impurities found in the electrolytically produced Al, no major conclusions could be drawn regarding the effect of LiF and CaF_2 on cermet anode performance. No statistical correlation could be drawn between impurities and electrolyte additives because of the close grouping of the Ni, Fe, and Cu impurities. However, the data imply that LiF is not harmful to anode performance as suggested by Alcoa researchers (Weyand et al. 1986). Furthermore, the anodes could be operated successfully in electrolytes that had higher bath ratios than reported possible by Alcoa. This indicates that the range of electrolyte compositions that can be used successfully with these cermet anodes is larger than previously believed.

4.1.9 Impurities in the Electrolyte

Because of the number of paths by which impurities could enter the electrolyte and the loss of electrolyte caused by volatility, accurate electrolyte mass balances were not possible for Cells 59 through 68. Impurity paths included the chemicals used to make up the electrolyte (Al_2O_3, AlF_3, CaF_2, LiF, cryolite), cell graphite, cermet anodes, and cell liner corrosion products, and loss of small tools and clamps. However, a much greater problem is encountered with electrolyte volatility. The loss of electrolyte by this method resulted in sufficient losses from all cells so as to thwart any attempts to determine the electrolyte mass balances. The analytical data reported in Table 4.1 for electrolyte impurities are those determined for "as-taken" bath samples. As all the sources for the Ni, Fe, and Cu impurities could not be determined, no attempt should be made to correlate these data with those listed for the electrolytically produced Al.

4.1.10 Corrosion Rates

The data in Table 4.1 were broken into two groups (standard 17 wt% Cu anodes and high-alloy anodes) for the purpose of calculating corrosion rates. Since the corrected Ni, Fe, and Cu impurity levels found in the electrolytically produced Al were known, the following equation was used to calculate the corrosion rate of the cermet anodes as a function of each impurity element:

$$k_{corr(i)} = \frac{Ri \cdot 8760}{Xi \cdot \rho \cdot A}$$

where $k_{corr(i)}$ = the corrosion rate per element i in cm/year

R_i = the weight lost from the anode of the ith anode constituent (gm/h)

X_i = the gravimetric ratio of the ith component in the anode

ρ = the fabricated anode density (g/cm^3)

A = the surface area of the anode immersed in the electrolyte (cm^2)

8760 = a conversion factor (h/yr).

The standard $NiO-NiFe_2O_4$-17% Cu anodes have the following elemental weight fractions based on the anode mass balance established during fabrication:

$X_{Fe} = 0.280$

$X_{Ni} = 0.337$

$X_{Cu} = 0.170$

$X_O = 0.213$

The gravimetric ratios were similarly calculated for the high-alloy $NiO-NiFe_2O_4$-Cu-Ni-Al anodes used in Tests 63 through 66. The corrosion rates for the anodes tested during FY 1988 are listed in Table 4.2.

4.1.11 Standard NiO-$NiFe_2O_4$-17% Cu Anodes

The corrosion rates for the anodes used in Tests 59, 60, 61, 62, and 67 are shown in Table 4.2. The corrosion rates determined for the anodes based on each element vary according to the element. It should be noted that the corrosion rate based on Ni is the lowest of the three, while for Cu it is the highest. In the worst case [$k_{corr(Cu)}$], these anodes might wear an average of 0.64 cm/year. The best case [$k_{corr(Ni)}$] wear rate average is 0.075 cm/year. The average of $k_{corr(Fe)}$ is 0.51 cm/year. The $k_{corr(Fe)}$ value for Test 59 was not used in the average as it is suspect because of possible contamination by corrosion products from the cell liner.

TABLE 4.2. Anode Corrosion Rates Determined from Tests Performed in FY 1988. Rates are given as a function of element and have the units of cm/year. Anode compositions may be found in Table 5.1, Section 5.0.

Experiment Number		$k_{corr(Fe)}$	$k_{corr(Ni)}$	$k_{corr(Cu)}$
59		1.97[a]	0.12	0.61
60		0.05	0.01	0.47
61		0.41	0.02	0.15
62		1.14	0.15	1.33
67		--	--	0.54
	Average	0.51	0.075	0.64
63		1.59	0.11	1.33
64		2.05	0.09	0.95
65		1.85	0.09	1.03
66		1.93	0.29	--
	Average	1.88	0.14	1.09

(a) Value is suspect - see text.

These values are promising and are lower than those determined by Alcoa. The values determined by Alcoa researchers (Weyand et al. 1986) are compared with the PNL values in Table 4.3. It should be noted that the Alcoa values were obtained from 60 A, 200-h tests, which are longer and of greater current load than the PNL tests. The Alcoa tests may also have been performed at high current densities, but this remains unconfirmed as Alcoa reports difficulty in determining true anode current densities.

The corrosion rate average obtained in the shorter, lower-current PNL tests for Fe and Cu is only 30% of the Alcoa values; the corrosion rate obtained by PNL for the anodes based on Ni is only 5% of the Alcoa average value. These results suggest that the corrosion of Ni may not constitute the serious problem encountered by Alcoa (Weyand et al. 1986).

It is not advisable to postulate "scaled-up, real-world" values from these data. Research performed in the past by others has shown that, in general, small-scale test results do not "scale up" with any great success. What these results do point out is that these materials are ready for the next larger step in testing: long-term laboratory testing. Research to be performed in FY 1989 will focus on the performance of a 100-h, 200-A test followed by a 1200-A, 3-week pilot-scale test. Successful results at that stage will point the way for commercialization.

TABLE 4.3. Comparison of Corrosion Rates for Cermet Anode Tests Performed at Alcoa and PNL. The anodes were NiO-$NiFe_2O_4$-17% Cu

Corrosion Rate, cm/year	Alcoa (2-run average)	PNL (5-run average)
$k_{corr(Fe)}$	1.69	0.51[a]
kcorr(Ni)	1.63	0.075
kcorr(Cu)	1.84	0.64

(a) Four runs used for average.

4.1.12 $NiO-NiFe_2O_4$-Cu-Ni-Al Anodes

Corrosion rates for the Tests 63 through 66 were calculated despite the fabrication-related reduced layer on the surface of each anode. These results are shown in Table 4.2. The averages for the corrosion rates are also listed. These rates compared well with the values Alcoa obtained for their $NiO-NiFe_2O_4$-17 wt% Cu (Weyand et. al. 1986) cermets. This may suggest that these high-alloy, high electrical conductivity anodes should be further investigated in FY 1989.

4.2 OPTIMUM CONDITIONS

The Optimum Conditions Task for FY 1988 involved a long-term test in which the test conditions spanned conditions considered to be suitable for operation of the inert anodes. A new cell was required to run this test, and SiC was selected as the cell material. However, as will be shown, the SiC material oxidized, dissolved in the cryolite, and interfered with the test objectives. After 100 h, the test was stopped because of the SiC interference and cell degradation. Some useful information was obtained from this test, however, and is summarized below.

In the past, short-term tests have been run in graphite and Al_2O_3-lined electrolysis cells with some success. However, the cells degraded badly and it appeared that for long-term tests a special cell material would be needed. The use of SiC was suggested as a material that would withstand attack by cryolite. Silicon nitride-bonded SiC has been used in commercial electrolysis cells as a sidewall component and for parts of the cell bottom.

With the assumption made that a long-term test could be run in a SiC cell, a cell was constructed from Si_3N_4-bonded SiC that was 19 cm (7.5 in.) inside diameter and 24 cm (9.5 in.) outside diameter. This material was surrounded by an oxidation-resistant metal can (Hastelloy-X®) to act as a secondary containment for the cryolite. Three anodes (discussed in Section 4.1) were used in this cell. The anodes were each run at 20 A. The target

---

® Hastelloy is a registered trademark of Haynes International, Inc., Kokomo, Indiana.

bath ratio for the electrolyte was 1.34. In this test, the plan was to run the cell for 100 h, after which parameters such as current density and electrolyte composition were to be varied.

From the start of the test, the cell appeared to be degrading. It was anticipated that under electrolysis the bath ratio would remain nearly constant or increase as $NaAlF_4$ was vaporized. However, the bath ratio decreased, indicating the consumption of sodium. In graphite or carbon cells, sodium is consumed during electrolysis when the sodium in the electrolyte is reduced to the zero valence state and intercalates into the graphite or carbon structure. The decreasing bath ratio indicated that something similar might be taking place in this cell. High SiO_2 contents and Si metal were found in the electrolyte samples taken from the cell, indicating that SiC was both oxidized and reduced in the cell. Samples were analyzed by dissolving them in acid and submitting them for ICP spectroscopy. As the test progressed, SiO_2 began to interfere with the Al_2O_3 analyses, in that analytical results indicated a steadily increasing Al_2O_3 content in the electrolyte when little or no Al_2O_3 had been added. The analytical results from the samples taken during this test are discussed in more detail below.

Figures 4.12 and 4.13 summarize the results from the analysis of the electrolyte samples taken during the test. The electrolyte samples could not be quantitatively dissolved, so these data are the result of leaching the electrolyte with HCl, which has been found to extract most of the elements of interest. These data are plotted against the cumulative test time, which has not been corrected for 4 h of down time. Bath ratio values varied from 1.4 to 1.24--the target value was 1.35. During electrolysis, the trend was toward lower bath ratios, indicating that Na was being consumed. Sharp increases in the bath ratio were a result of adding NaF to the electrolyte.

Boron concentrations (Figure 4.12) increased rapidly then decreased toward a steady-state value. Iron and nickel (Figure 4.12) and copper and silicon (Figure 4.13) increased gradually until about 60 h when the concentrations increased more rapidly. At 60 h, a large amount of solid sludge-like material was removed from the bottom of the cell. It is uncertain if removing this sludge-like material resulted in increase of anode constituents

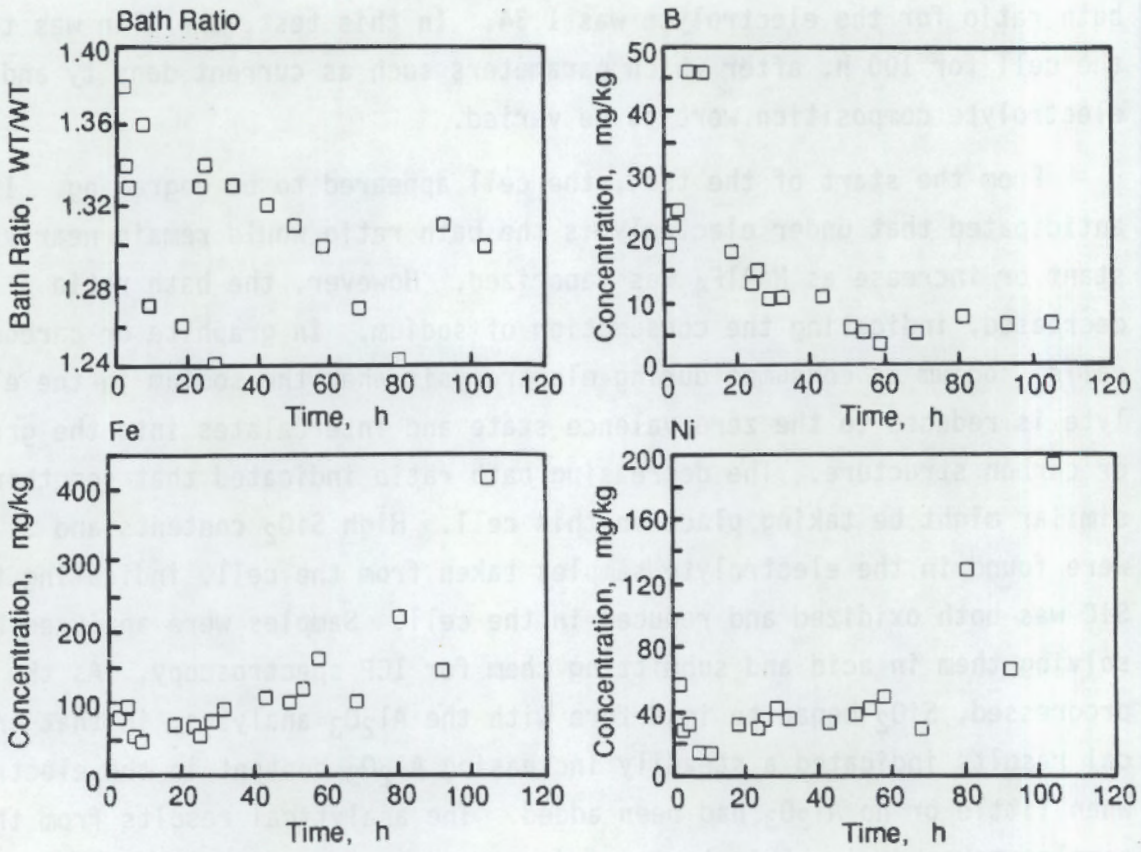

FIGURE 4.12. Summary from Analysis of Electrolyte Samples

in the electrolyte or if the observed increase was coincidental with the removal. At about the same time, the Ni rods used as electrical connectors on two of the anodes failed at welds, so only one anode was in the cell from 68 h to 100 h. The slowly increasing Ca concentrations shown in (Figure 4.13) are expected, since the Ca was added during makeup of the lost electrolyte but not lost by volatilization. Chromium in the electrolyte most likely came from the oxidation products of the Hastelloy-X can that surrounded and extended above the SiC cell. This can was used as a secondary containment in case of catastrophic failure of the SiC vessel.

Only five Al samples were obtained during the test. After about 50 h, there was no more metal that could be tapped from the cell and no metal was found when the cell was disassembled. Although there is a great deal of scatter in the data, it is useful to look at ratios of various components.

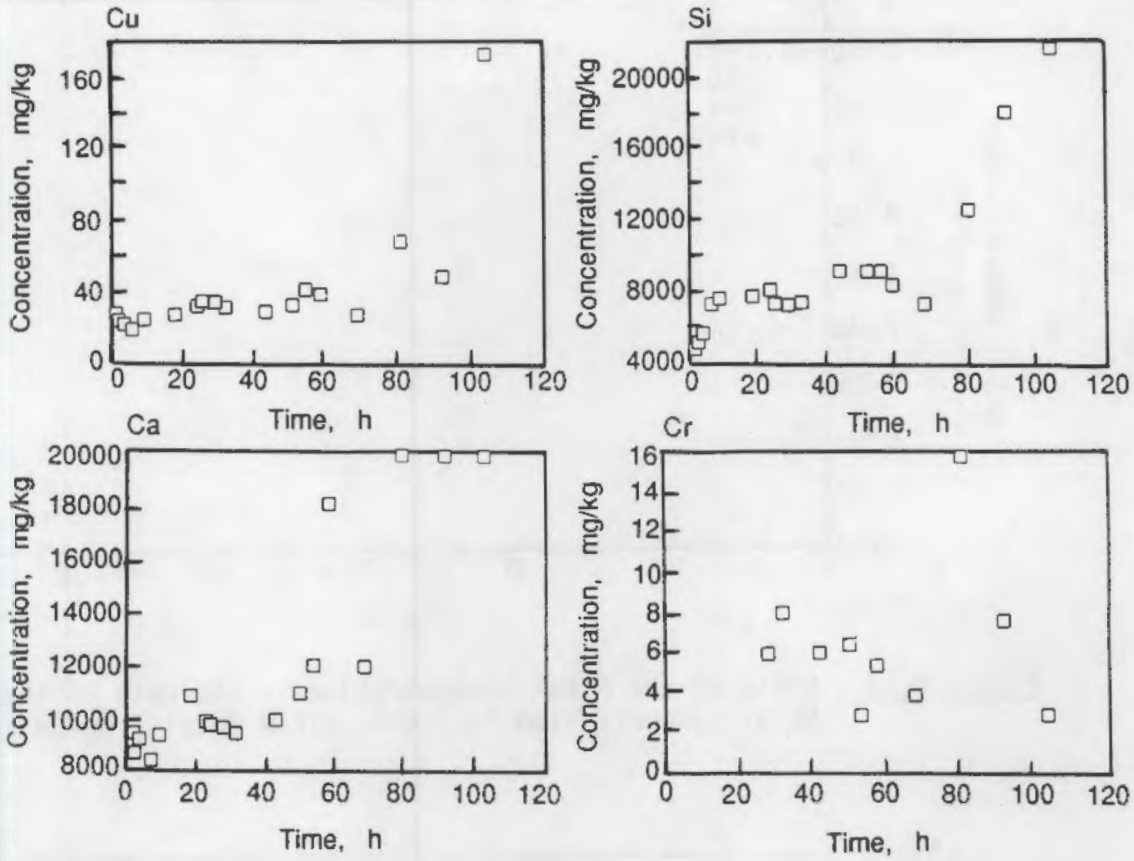

FIGURE 4.13. Summary from Analysis of Electrolyte Samples

Figure 4.14 shows the ratio of impurities found in the electrolyte to the impurities found in the Al metal samples. The ratios indicate a steady decrease, consistent with an increasing concentration of metal impurities in the Al, while the impurity concentration in the electrolyte remained nearly constant. Unfortunately, no Al metal samples could be recovered during the period that metal impurities in the electrolyte were increasing. However, once Al metal was removed as an impurity sink, the concentration of impurities in the electrolyte would be expected to increase.

Figure 4.15 shows the ratios of anode constituents in the electrolyte and in the Al metal plotted against time. Included in this plot are lines corresponding to the same ratios found in the anode. In the electrolyte, the Cu/Fe and Ni/Fe ratios are equal to each other and approximately the same as the Cu/Fe ratio in the anode, but about a factor of 3 less than the Ni/Fe

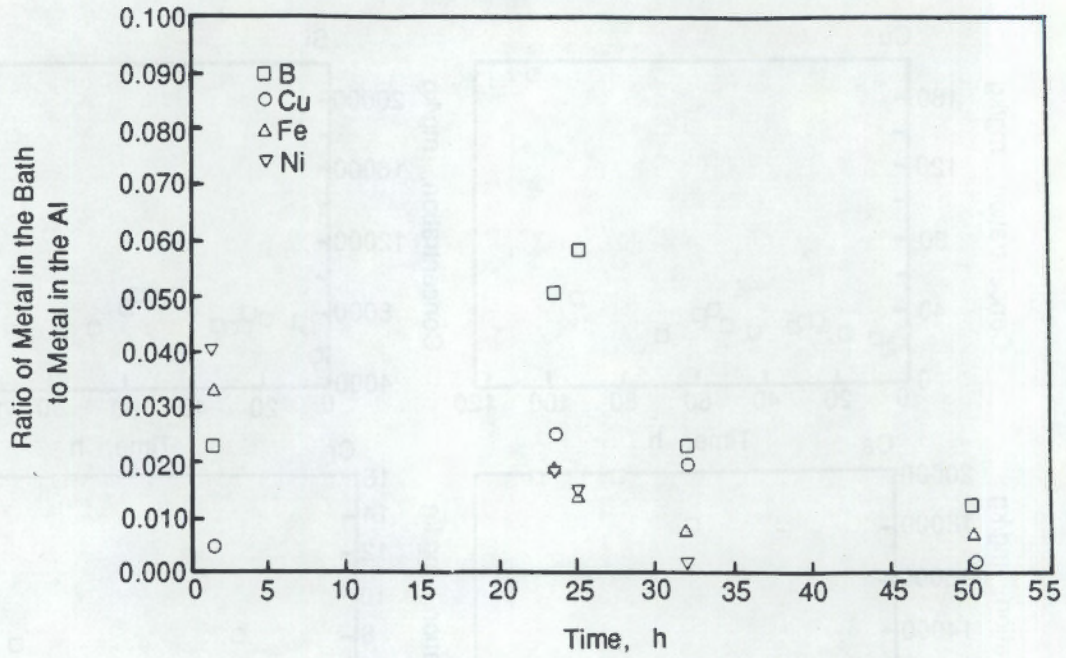

FIGURE 4.14. Ratio of the Metal Concentration in the Bath to the Metal Concentration in the Aluminum Metal from Cell 69

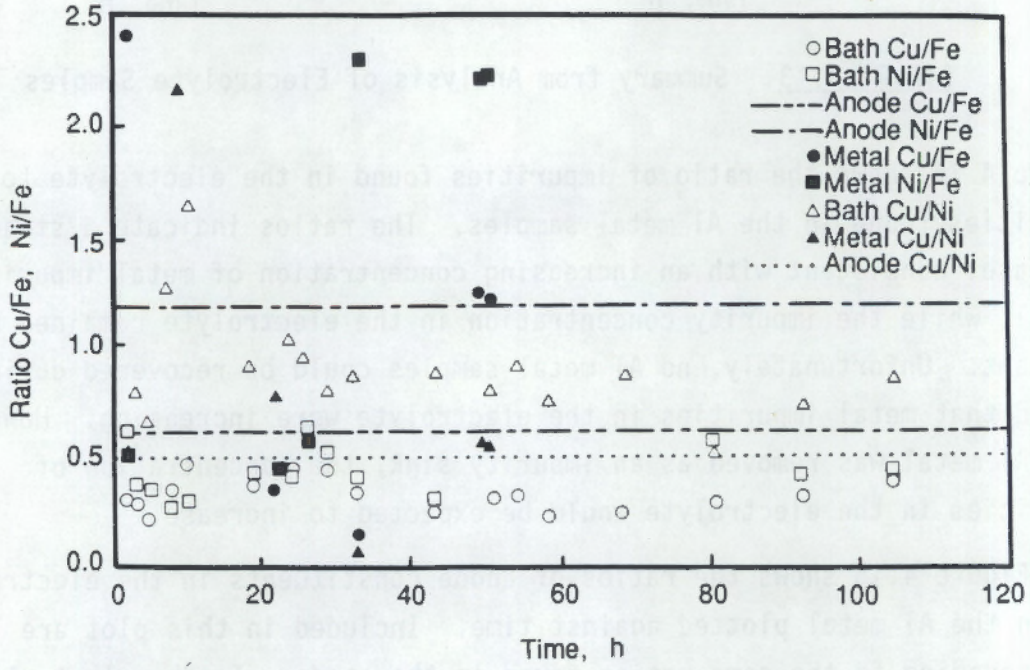

FIGURE 4.15. Anode Metal Ratio in the Bath and Aluminum Metal from Cell 69

ratio in the anode. The Cu/Ni ratio is about a factor of 2 higher than the Cu/Fe and Ni/Fe ratios in the electrolyte and about 80% higher than the Cu/Ni ratio in the anode. It should be pointed out that the concentrations of Fe and Ni are well below the saturation concentrations observed at Alcoa (Baker 1983). The data shown in Figure 4.15 for the electrolyte indicate that, if the impurities came solely from anode corrosion, the process may not be congruent and that other sources and/or sinks exist for these metal species. One likely source of Fe and Ni is the Hastelloy oxidation products. At least two sinks for the metal constituents have been identified in addition to the Al metal. These are the vaporization of metal species - high concentrations of Ni were found in the condensate on the Al_2O_3 feed tube - and an intermetallic species found in the solidified electrolyte. This intermetallic is josephineite (approximately 25% Fe and 75% Ni). It is uncertain if this phase was present at temperature or precipitated during cooldown. The ratios of impurities found in the Al metal are too scattered to draw many conclusions (Figure 4.15).

In an effort to understand some of the chemical processes that took place in the cell, several samples of solidified electrolyte were characterized using X-ray diffraction. In the method for determining the Al_2O_3 content of the electrolyte, the material that is insoluble in boiling $AlCl_3$ is filtered and fired at 1000°C. Toward the end of the test, a black material was observed in filtered and fixed solids. An X-ray analysis of the fixed material showed that this material consisted of iota-Al_2O_3 and gamma-Al_2O_3. Iota-Al_2O_3 is an impure form of Al_2O_3 containing about 1% SiO_2. Chemical analysis of this material suggested that the SiO_2 content was about 1.5%. Thus, the presence of SiO_2 from the oxidation of SiC was interfering with the Al_2O_3 analyses.

Electrolyte from the bottom of the cell was characterized using X-ray diffraction. The presence of cryolite (Na_3AlF_6) and significant amounts of Si metal were detected. A small amount of nepheline ($NaAlSiO_4$) was also detected. At the interface between the SiC cell and the electrolyte, significant amounts of nepheline and Si metal were found. Sodium in the zero

oxidation state can react with SiO_2 to form Si and Na_2O. Free sodium exists in the bath during electrolysis. Thus, the presence of Si metal is understandable.

The anodes from this cell were visually examined, and a small piece of one of the anodes was analyzed using X-ray diffraction. In the portion of the anode that lay below the electrolyte, a substantial portion of the anode has lost the copper color usually seen in cross sections and had turned black, which is indicative of either corrosion or oxidation. Since no increase in the porosity was visually detected, it was assumed that the copper had oxidized. This was confirmed using X-ray diffraction. Lines in the diffraction pattern could be assigned to a spinel ($NiO\text{-}NiFe_2O_4$), Cu_2O, NiO, $Cu_{0.2}Ni_{0.8}O$, and two very weak lines associated with an unidentified phase. The phase $Cu_{0.2}Ni_{0.8}O$ is actually the end member of a range of compositions $Cu_xNi_{1-x}O$ where x = 0 to 0.2. Since NiO and $Cu_{0.2}Ni_{0.8}O$ yield almost identical diffraction patterns, both were assumed to be present in the darkened portion of the anode. Since the $Cu_xNi_{1-x}O$ phase was essentially indistinguishable from NiO using X-ray diffraction and since $Cu_xNi_{1-x}O$ was the only phase identified as a Cu(II)-containing phase, additional analyses were needed to determine if Cu(I) was the only oxidation state for Cu in the oxidized portion of the anode or if Cu(II) was also present.

To determine the oxidation state of Cu in the oxidized portion of the anodes, X-ray photoelectron spectroscopy (XPS) was used to analyze a sample of the oxidized area. Results from the X-ray photoelectron spectrometer (Figure 4.16) allow the following general conclusions. The oxidation state of the Cu in the oxidized layer was predominantly Cu(I). In the oxidized zone no Cu metal was found using XPS or X-ray diffraction. About 85% of the Cu was Cu(I) and 15% Cu(II) in one sample and about 50% Cu(I) in another. It is not possible with these cursory examinations to determine if the Cu_2O was located closer to the unoxidized Cu metal or if it was intermixed with the CuO.

Since XPS allows only the first few atomic layers of the specimen to be probed, quantitative analyses of the solid surface are obtained. During the examination of the oxidized portion of the anode, a sample was fractured and

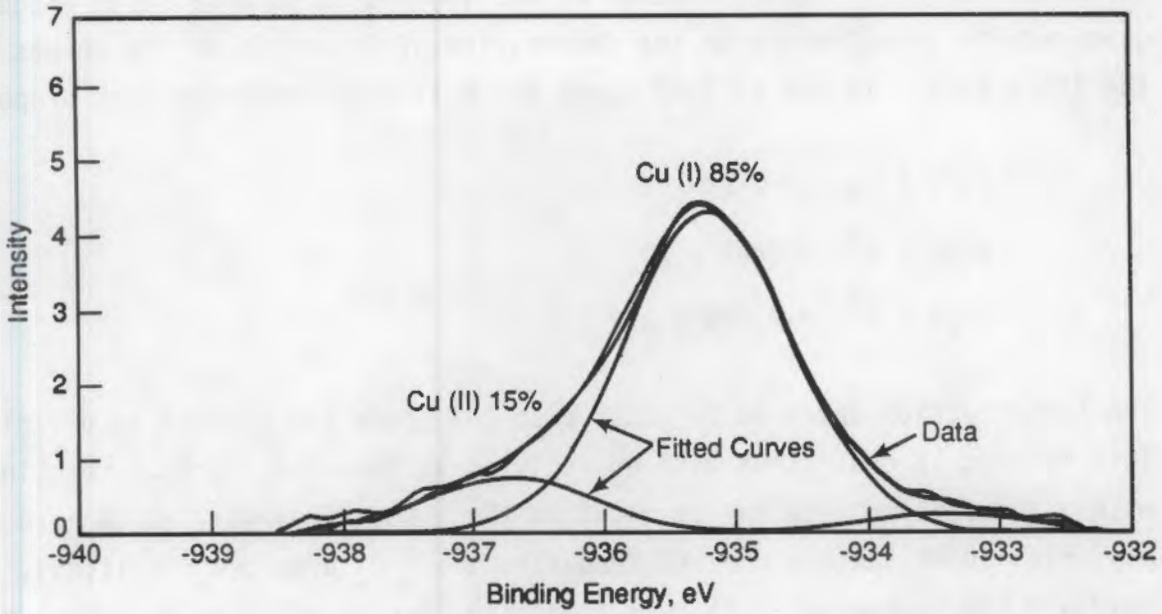

FIGURE 4.16. Results from the X-Ray Photoelectron Spectrometer

the fresh fracture surface examined. Presumably, most of the fracture surface resulted from cleavage along grain boundaries. Hence, the analysis of the fracture surface would give information on the material at the grain boundaries. The analytical results indicate that electrolyte had migrated into the anode material. The three major electrolyte components, Al, Na, and F, were found in the X-ray photoelectric spectrum from the oxidized layer, but the proportion of the components was different than expected from the electrolyte composition. At the grain boundaries, the molar ratio of Na:Al:F was about 1:1:2. This result suggests that the empirical formula for a migrating species in the oxidized layer was $NaAlOF_2$ (the oxygen content was obtained by charge balance). More analyses are needed to confirm this result, and more testing is needed to determine the role of $NaAlOF_2$ in the corrosion or oxidation of the inert anode. A significant amount of carbon or carbon-containing species was also found at the grain boundaries. The source and form of the carbon material is uncertain at this time, but it may be derived from the organic binder used during the anode fabrication process.

The solid-state analyses suggest that a nickel ferrite anode might be made with the oxides of Cu, rather than with metal. Electrochemical studies

performed during FY 1987 (Strachan et al. 1988) with pure Cu metal anodes gave results consistent with the observation of Cu oxides on the anodes after the 100-h test. In the FY 1987 study the following reactions were proposed:

$$Cu + F^- \rightarrow CuF + e^-$$

$$2CuF + O^{2-} \rightarrow Cu_2O + 2F^-$$

$$Cu_2O + O^{2-} \rightarrow 2\ CuO + 2e^-$$

The last reaction appeared to occur when the anode was anodically polarized. This finding is consistent with O_2 evolving at the anode surface reacting with and diffusing into the Cu metal in the anode. However, it is also possible, under the appropriate temperature and O_2 pressure conditions, for Cu_2O and CuO to coexist. This is predicted, for example, at an oxygen pressure of ~0.1 atmosphere and a temperature of 1000°C (Neumann et al. 1984). Thus, the presence of CuO and Cu_2O on the anode can be rationalized by means of either kinetic or thermodynamic arguments.

One of the reasons for not investigating Cu oxide-containing anodes initially was the high electrical resistance of the oxide. However, the data from the 100-h test indicate that the oxides at least do not hinder conduction and may be good conductors at 950°C, since the thickness of the anode-oxidized layer in that test approached 1 cm. That the copper oxides may be good high-temperature conductors is supported by limited high-temperature conductivity measurements, which show the conductivity of Cu_2O increasing by 10^4 over the temperature range 25°C to 200°C, from 10^{-6} to 10^{-2} mho/m. The Cu oxides, as well as NiO and $NiFe_2O_4$, are defect semiconductors. The conductivities of these oxides are expected to improve with increasing temperature.

4.3 REDUCED ANODE/CATHODE DISTANCE (ACD) TEST

Activities have been directed toward the design and fabrication of an experimental apparatus for determining current efficiency during the electrolytic production of Al with cermet anodes. The apparatus has a versatile design to serve the evaluation of current efficiency as a function of several

parameters, including anode-cathode spacing, anode and cathode slope, bath chemistry, different electrode geometries, and different electrode materials.

4.3.1 Design Status and Summary

The apparatus comprises a sealed laboratory-scale cell, which is equipped with instruments to measure the oxygen concentration in the off-gas from the electrolysis of Al_2O_3. Current efficiency is determined by comparing the amount of oxygen in the off-gas with the amount that is expected based on a known rate of power consumption at 100% efficiency.

An overall schematic of the apparatus is shown in Figure 4.17. There are four major components to the apparatus: 1) the superstructure, 2) the furnace, 3) the cell, and 4) the gas flow system. The superstructure is a steel weldment of simple design, which is used to position the furnace and adjust the slope of the cell between a level position and any position up to 20° from horizontal. The slope may be varied by handling turning two lead screws. The anode is positioned with a single-axis translator which moves by a hand-operated, rotating lead screw. The translator is attached to the superstructure so that the ACD can be varied during electrolysis. The anode may be positioned over a distance of 13 cm (5 in.) in increments as small as 0.025 mm (0.001 in.).

Originally, the cell comprised a SiC-Si_3N_4-based refractory crucible, which was a closed-bottomed right circular cylinder measuring 19 cm (7.5 in.) inside diameter, 24.1 cm (9.5 in.) outside diameter, 50.8 cm (20 in.) in height, and having a floor thickness of 2.54 cm (1 in.). Results from the long-term test reported in Section 4.2 indicated that a SiC crucible would be inappropriate for use in this test. During FY 1989, a new crucible will be designed and constructed from a combination of Al_2O_3 and graphite. A schematic of the proposed cell is shown in Figure 4.18. The crucible is positioned inside a top-opening electric furnace. The graphite crucible is press-fit into the Inconel 601 can. The cathode electrical connection is made by forcing an Inconel rod between the metal can and the graphite crucible.

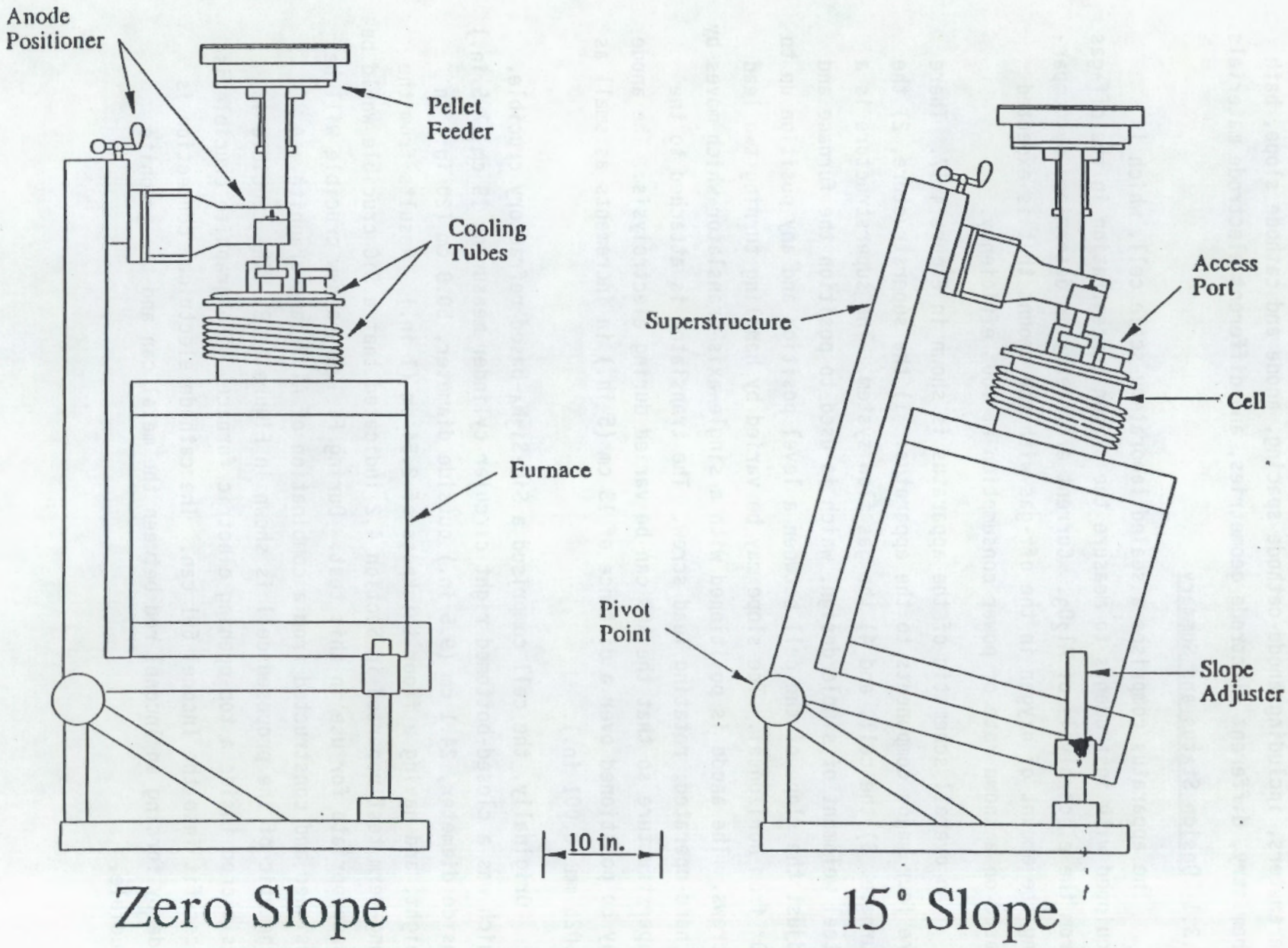

FIGURE 4.17. Adjustable ACD/Slope Apparatus

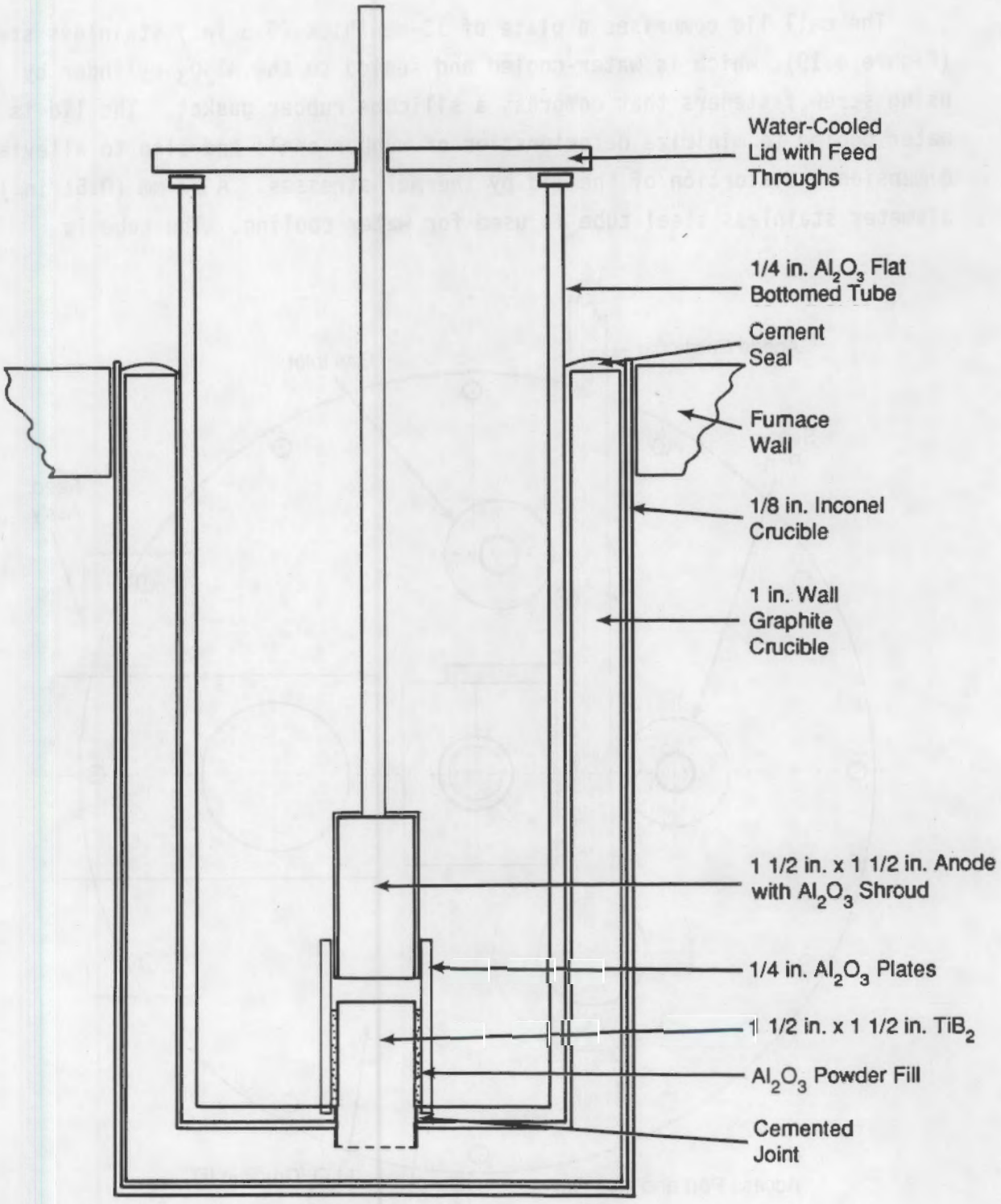

FIGURE 4.18. Proposed Cell Design for the Reduced Anode-to-Cathode Distance Test

The cell lid comprises a plate of 13-mm-thick (0.5 in.) stainless steel (Figure 4.19), which is water-cooled and sealed to the Al_2O_3 cylinder by using screw fasteners that compress a silicone rubber gasket. The lid is water-cooled to minimize deterioration of rubber seals and also to alleviate dimensional distortion of the lid by thermal stresses. A 13-mm (0.51 in.)-diameter stainless steel tube is used for water cooling. The tube is

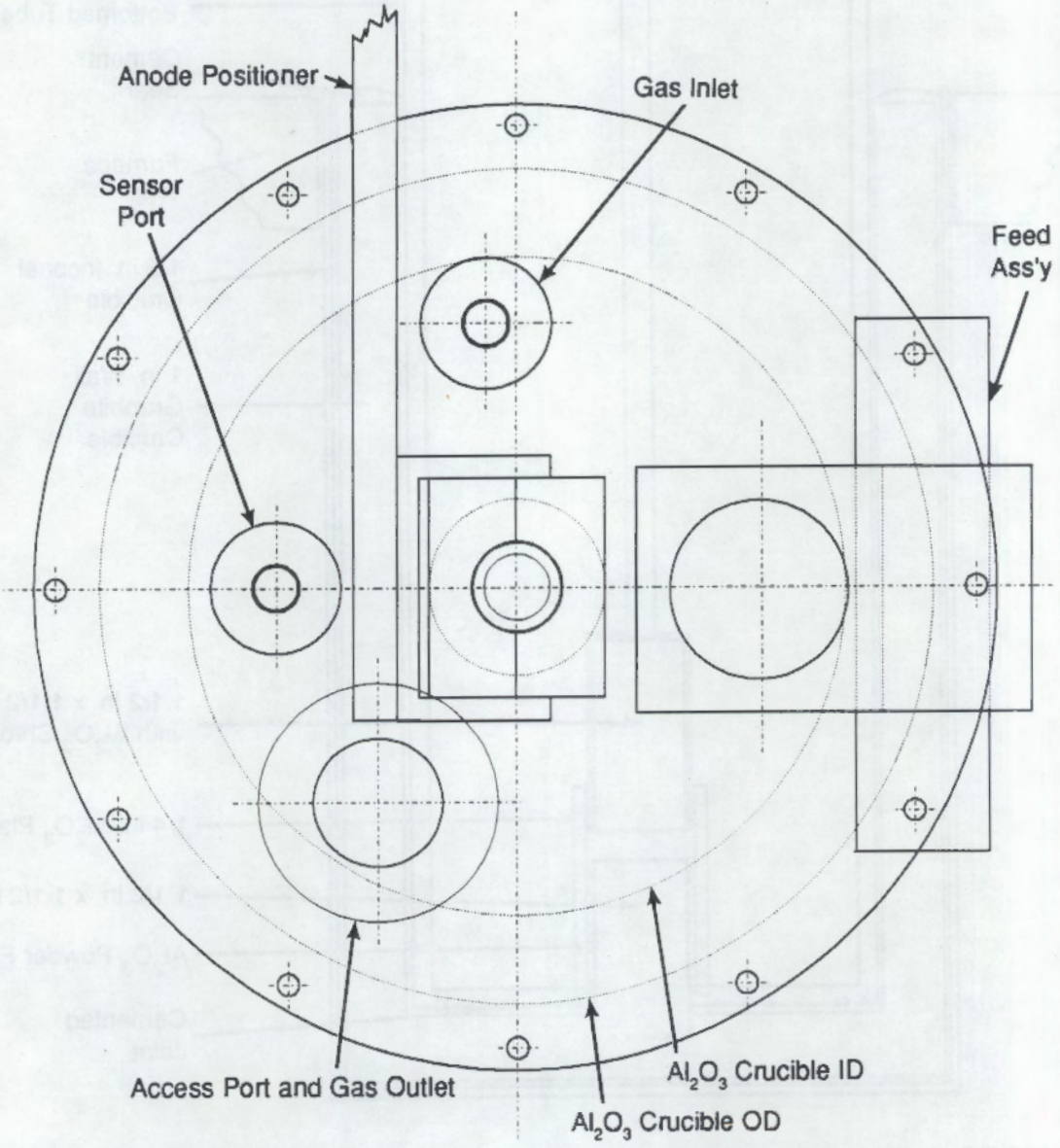

FIGURE 4.19. Cell Lid: Top View

tack-welded to the top of the lid in a close-fitting, serpentine pattern. Soft solder fillets are added to each side of the cooling tube to enhance heat transfer.

Attached to the lid are feedthroughs for the anode, feeder, inlet gas tube, and sensor (an example is shown in Figure 4.20). These feedthroughs are designed with similar features to facilitate fabrication, use of interchangeable parts, and cooling of O-rings and to maximize the cooled surface area on the cell lid. These feedthroughs are also designed to enable removal of the anode, sensor, inlet gas tube, and feeder during cell operation without detaching the cell lid. Also attached to the lid is a multi-purpose

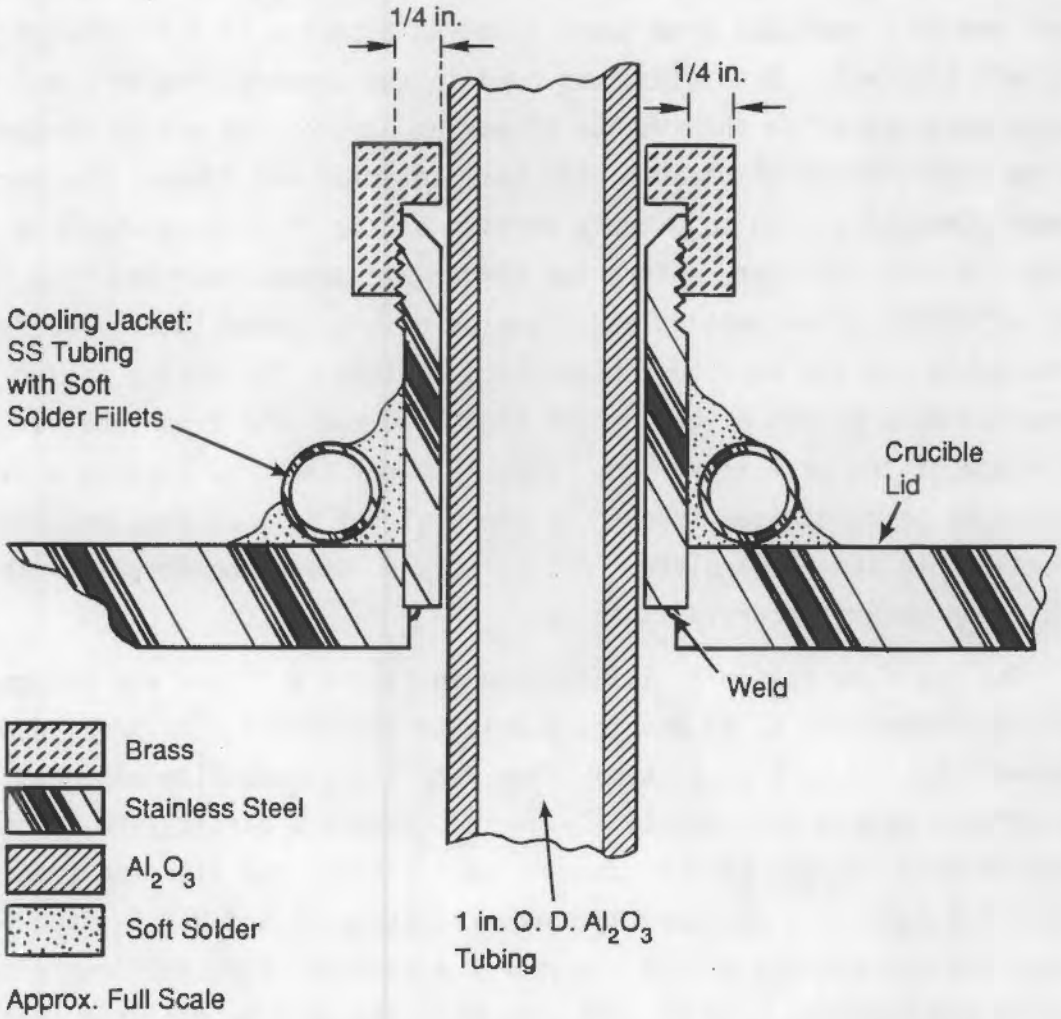

FIGURE 4.20. Feedthroughs for the Anode, Feeder, Inlet Gas Tube, and Sensor

port, which has a removable plate allowing access to the cell interior. This port is carefully positioned to enable viewing of all major components inside the cell (anode, sensor, inlet gas tube). The multi-purpose port also serves as an off-gas feedthrough. Although clogging of the off-gas feedthrough may occur, this feedthrough can be easily monitored and cleaned because of its closeness to the multi-purpose port.

The cell is fed at an adjustable rate by a pellet feeder (Figure 4.21), which contains up to 30 pressed pellets of Al_2O_3 measuring 13 mm (0.5 in.) diameter by 19 mm (0.75 in.) tall. The pellets are circumferentially held in a rotating tray driven by an electric stepping motor and associated controller. Each time the cell is fed, the tray pushes a pellet over a hole at the upper end of a vertical drop tube, allowing a pellet to fall through the tube and into the cell. Plexiglass was used in the construction of the feeder to reduce mass and allow observation of moving parts. The entire feeder is sealed from ambient atmosphere; the cell interior and feeder interior share a common atmosphere. An adjustable portion of the inlet gas, which is used to purge the cell interior, enters the feeder and passes down the drop tube to help alleviate deterioration and plugging of the feeder tube. The feeder has a removable lid for ease of replenishing pellets. The entire feeder is supported by a welded Al brace that hinges to keep the drop tube vertical as the slope of the cell is varied. This is a key feature, because a line-of-sight must be maintained throughout the angle of tilt so that pellets fall directly into the electrolyte. All parts are interchangeable, and the feeder is used on other electrolysis tests.

The gas flow system is illustrated in Figure 4.22 and was designed based on discussions with W. E. Haupin, a private consultant. An Ar stream is metered into the cell at a steady flow rate via a mass flow controller, and the off-gas stream is successively passed through a particulate filter, fluorine trap, oxygen sensor, and wet test meter. The fluorine trap entails use of 1 M NaOH in a gas washing bottle to strip HF and $NaAlF_4$ from the gas stream and protect the oxygen analyzer. A chemical indicator may also be used in the fluorine trap to determine when the NaOH is depleted. At the end of an experiment, the solution in the gas washing bottle may be analyzed for

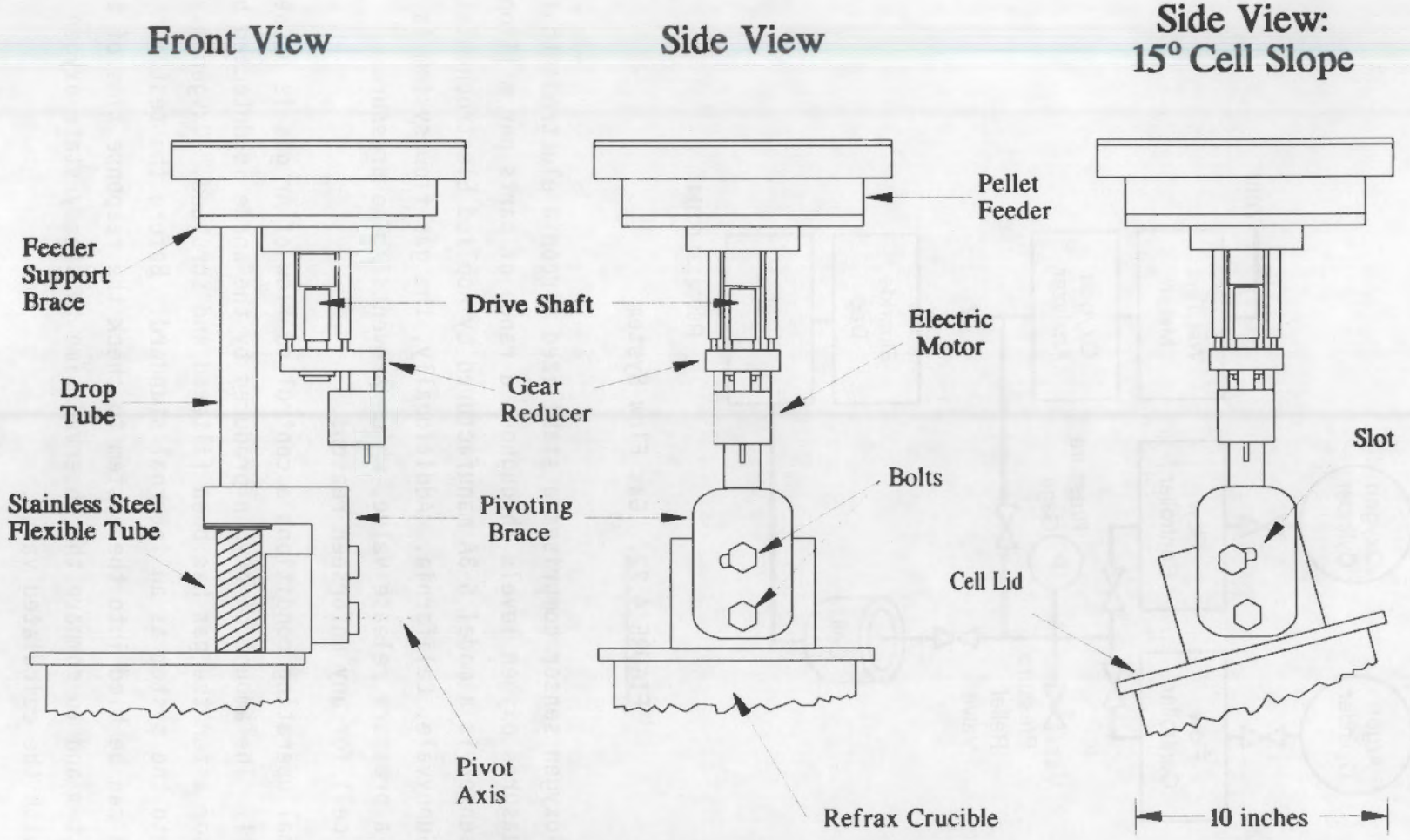

FIGURE 4.21. Pellet Feeder Assembly

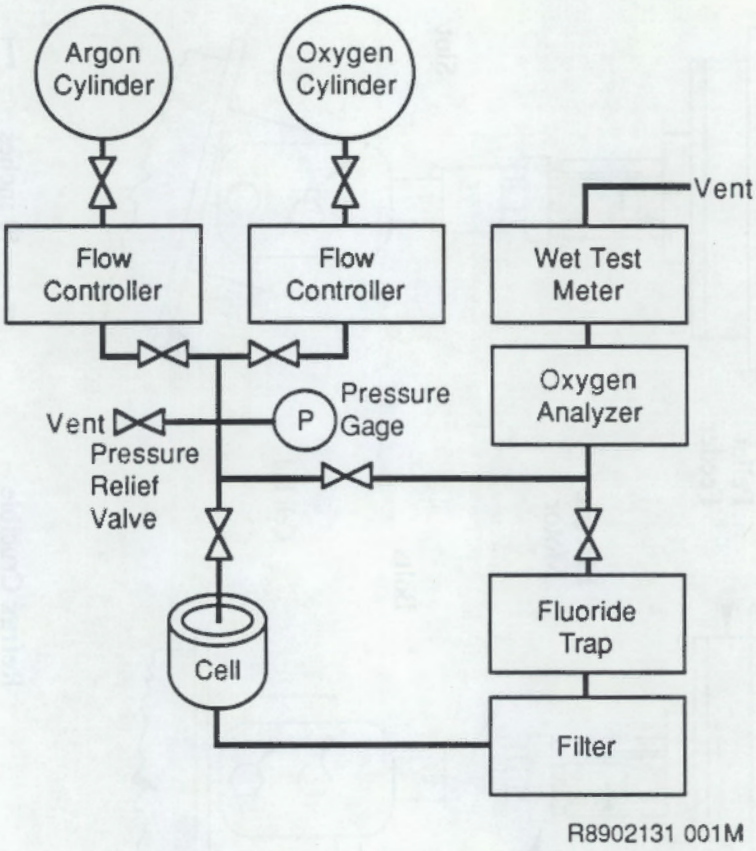

FIGURE 4.22. Gas Flow System

F and Al. The oxygen sensor comprises a stabilized zirconia electrode that continuously measures oxygen levels throughout a range of parts per million to 100%. The sensor is a model S-3A manufactured by Applied Electrochemistry Incorporated, Sunnyvale, California. Additionally, the gas flow system is protected with a pressure release valve, which prevents undue pressure buildup in the cell for any unforseen reasons.

Under normal operating conditions a controlled flow of Ar gas is passed through the cell. The amount of oxygen produced by the anode is detected by the oxygen sensor after the gas has been filtered and scrubbed. Oxygen may also be bled into the system as an internal standard. Before the test is started, oxygen can be bled into the system to check the response time of the measurement system and to compare the observed time to steady-state oxygen concentration with the calculated value.

A general expression was derived to model the oxygen concentration in the off-gas as a function of time, mass flow rate of oxygen emanating at the anode, mass flow rate of argon entering the cell, and the cell volume. The expression is as follows:

$$c/w = 1-\exp\left(-\frac{R}{V}t\right)$$

where $c = O_2$ concentration at the cell exit

$w = O_2$ concentration entering the cell from the anode

R = gas flow rate

V = cell volume.

Sample calculations proceed after the derivation and provide valuable guidance as to what range of Ar flow rates are to be selected and also what corresponding times are required for the cell to reach a steady-state concentration of oxygen. The results shown in Figure 4.23 indicate that, for example, at an Ar inlet flow rate of 300 cm^3/s, 5 min are needed for the off-gas to reach a steady-state oxygen concentration of 0.9%. Curves are also shown for 50, 100, 200, and 400 cm^3/s.

4.3.2 Fabrication and Assembly Status

To date, fabrication has been completed on the superstructure, and anode positioner, screw fasteners for the cell lid, and all parts of the feeder except for the support brace assembly, which positions the feeder above the cell lid. The cell lid, feedthroughs, and the support brace assembly for the feeder have also been constructed. The gas flow system is approximately one-third assembled. The feeder has been assembled and used in an electrolysis experiment. The feeder was found to operate acceptably with a gear motor instead of a stepping motor, but a stepping motor will be used in later experiments so that the feeder can be controlled using a computer.

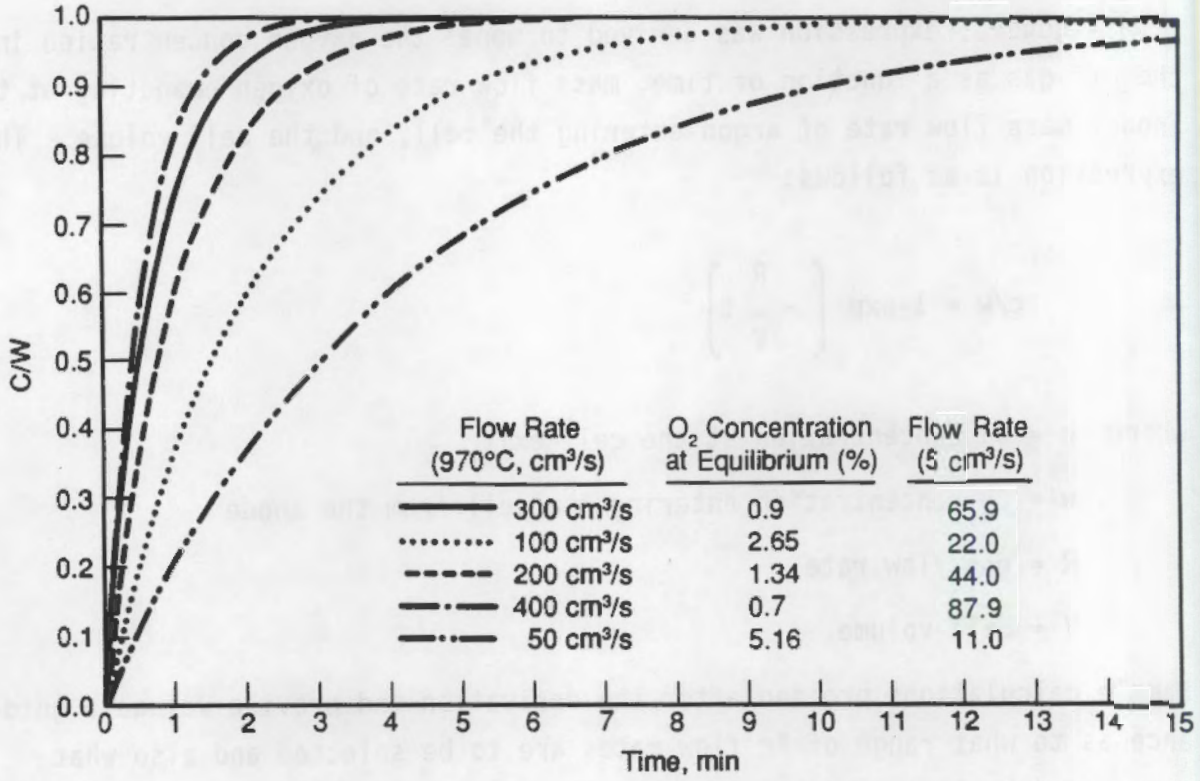

FIGURE 4.23. Time for the Gas Composition from the Reduced ACD Cell to Reach Equilibrium After a Change in Oxygen Content

5.0 ANODE FABRICATION

Sintering test runs were performed to produce NiO-$NiFe_2O_4$-Cu-based cermet materials for electrolysis tests and sensor development work in FY 1988. In general, "standard" NiO-$NiFe_2O_4$-17% Cu cermet materials were fabricated for use in sensor development, and the method of production for these materials has been discussed previously (Strachan et al. 1988). Cermets fabricated for electrolysis testing were evaluated on the basis of density and microstructure. Typically, cermets with high sintered density and a homogeneous microstructure were selected for testing. The key elements of the fabrication parameters for the cermet anodes used in Tests 59 through 69 (discussed in Section 4.0) are described below.

The standard NiO-$NiFe_2O_4$-17% Cu anode materials were initially developed by Alcoa (Weyand et al. 1986). Research has been performed at PNL to improve upon the fabrication process. Two of the principal goals of this research have been to improve the distribution of phases within the microstructure and increase the electrical conductivity of these cermets. Much of this work is discussed elsewhere (Hart et al. 1987; Strachan et al. 1988; and Marschman and Davis 1987).

The basic PNL fabrication procedure for the NiO-$NiFe_2O_4$-17% Cu cermets (Marschman and Davis 1987) was used to produce the samples that have been ceramographically examined and shown in Figures 5.1 through 5.4. Table 5.1 lists composition and density of these and other cermet anodes.

The microstructure shown in Figure 5.1 is typical of those formed using the Stackpole[(a)] 5324 duplex NiO-$NiFe_2O_4$-Cu spray-dried powder mechanically blended with 17 wt% Aremco[(b)] "5-15 μm" Cu powder. Anodes fabricated using this formulation have been used by this task for laboratory-scale electrolysis testing. Anodes numbered 115-24, 115-26, 109-4, 109-6, 111-12, and 138-H-1 have been used in experiments numbered 59, 60, 61, 62, 67, and 68, respectively, during FY 1988.

(a) Stackpole Corporation, St. Mary, Pennsylvania.
(b) Aremco Products Incorporated, Ossining, New York.

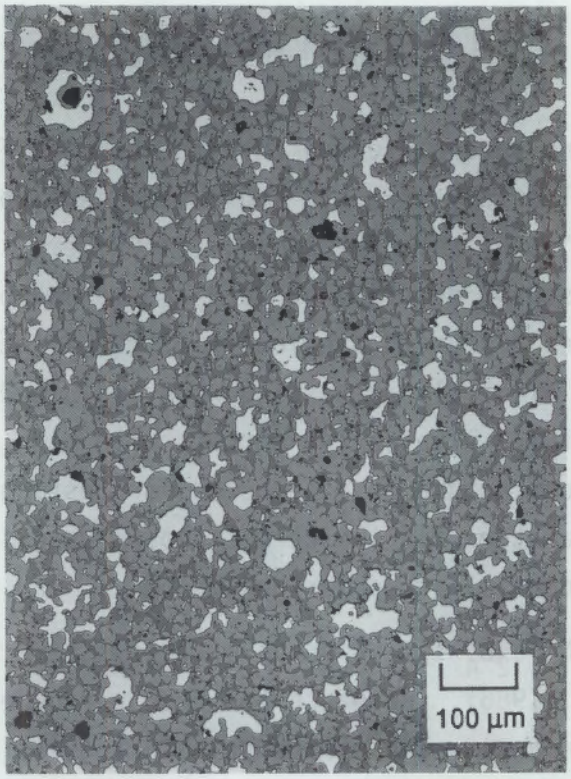

151-2

FIGURE 5.1. $NiO-NiFe_2O_4$-17% Cu. Density 6.11 g/cm^3. Aremco Cu, standard process.

Efforts to locate alternative sources of inexpensive Cu powder were undertaken in FY 1988, and Cu powder was purchased from Alamo Supply Company, Inc., Houston, Texas, and Greenback Industries, Greenback, Tennessee. Typical microstructures of $NiO-NiFe_2O_4$-Cu cermets produced using these Cu powders are shown in Figures 5.2 and 5.3. These microstructures are very similar to that shown in Figure 5.1, indicating that many Cu powder sources can be used to produce these cermets. It should be noted that careful attention was paid to the fabrication procedures to ensure these consistent results.

The $NiO-NiFe_2O_4$-Cu cermet materials were used to produce anodes of two basic shapes. Typically, right cylindrical shapes were used for the laboratory-scale testing and sensor development efforts. Those used in the laboratory-scale testing efforts were approximately 3.2 cm (1.3 in.) diameter by 5 cm (2 in.) long. Smaller versions, 1 cm (0.4 in.) diameter by 2.5 cm (1 in.) long, were used in the sensor research.

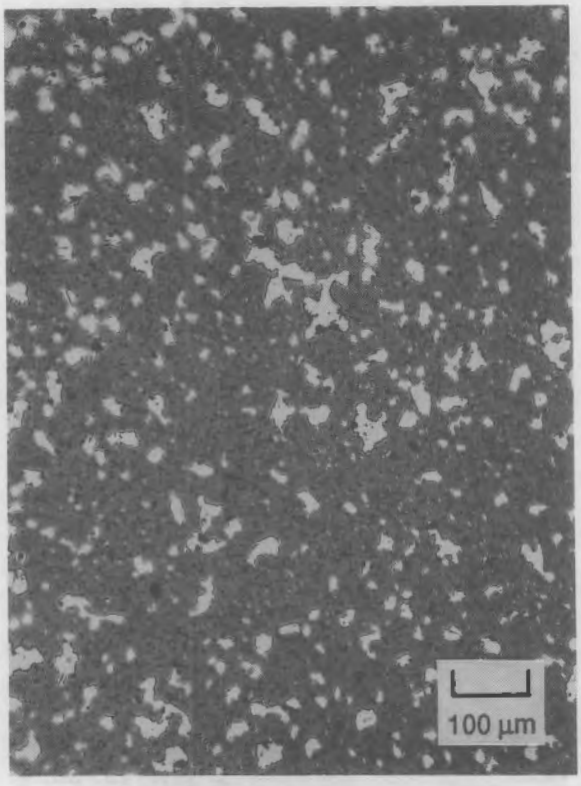

154-B

FIGURE 5.2. $NiO-NiFe_2O_4$-17% Cu. Density 6.06 g/cm^3. Alamo Cu, standard process.

A third shape was developed for experimental use. To reduce the amount of material in each anode and provide more surface area (to allow greater cell amperages), a thin-walled, cup-shaped anode was developed. All of the cup-shaped anodes produced in FY 1988 were fabricated using the standard $NiO-NiFe_2O_4$-17% Cu composition. Figure 5.4 shows both a green, as-pressed anode, and a sintered, test-ready anode. These anodes utilized a threaded electrical connection, as the anodes were fabricated with a Cu/Ni alloy core that could be drilled and tapped after sintering.

The thin-walled anodes not only reduce materials consumption, but the "cup" portions of the anodes provide some protection for the electrical connector from the corrosive electrolyte vapors. The "cup" portions of these anodes were typically filled with coarse-grained alumina powder after the electrical connection rod was attached to the anode. The alumina provided an effective seal over the connection by reacting with the electrolyte vapors to form a high-melting-point cement.

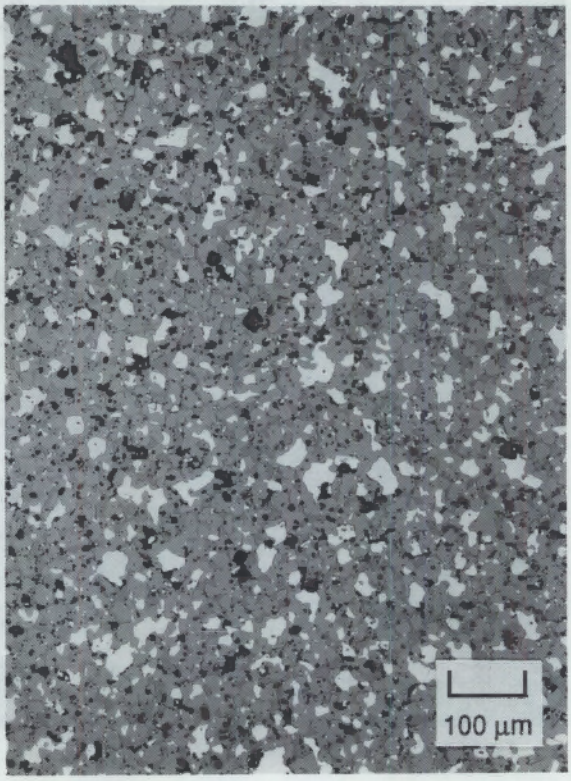

157-5

FIGURE 5.3. $NiO-NiFe_2O_4$-17% Cu. Density 6.03 g/cm^3. Greenback Cu, standard process.

The thin-walled, cup-shaped anodes were fabricated using a rigid Teflon®-coated aluminum mandrel positioned inside a flexible polyurethane mold. The pre-blended cermet powder was loaded into the mold and isopressed at pressures between 20 and 25 ksi to form the green body shown in Figure 5.4. The walls of the as-sintered anode shown in the figure are about 25 mm (1 in.) thick. The base of the anode is solid to accommodate a Cu/Ni alloy center core. The core is drilled and tapped for use as a threaded electrical connection and support. This design may be scaled up within the size limits of the available press and sintering equipment.

® Du Pont de Nemours and Company, Wilmington, Delaware.

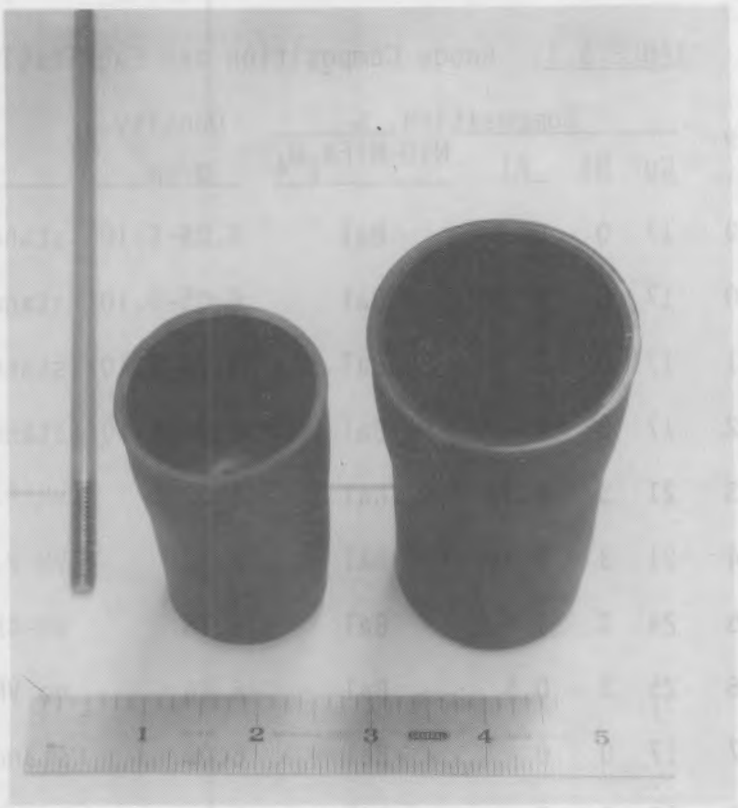

FIGURE 5.4. Cermet Test Anodes - NiO-$NiFe_2O_4$-17% Cu. Green anode as-pressed, right, and sintered anode, left.

5.1 PNL-DEVELOPED NiO-$NiFe_2O_4$-Cu OXIDE-BASED ANODES

The microstructure shown in Figure 5.5 is a standard NiO-$NiFe_2O_4$-17% Cu cermet that was fabricated using a PNL-developed NiO-$NiFe_2O_4$-Cu powder rather than the spray-dried Stackpole powder. As discussed previously (Strachan et al. 1988), a minor effort was made in FY 1987 to develop an alternate source of NiO-$NiFe_2O_4$ powder. Although homogeneous microstructures with high sintered density were produced in cermets made using this powder, none were electrochemically tested. Thus, several samples were fabricated in FY 1988 for electrolysis testing.

The PNL-produced NiO-$NiFe_2O_4$ powder, identified as PNL-800, is an oxide formulation that was blended and milled with the copper constituent instead of using a commercially prepared ferrite powder. The steps used to prepare a powder containing the PNL-800 oxide and 17% Cu are as follows:

TABLE 5.1. Anode Composition and Fabrication

Anode No.	Exp. No.	Composition, % Cu	Ni	Al	$NiO-NiFe_2O_4$	Density, g/cm^3	Comments
115-24	59	17	0	0	Bal	6.05-6.10	standard process
115-26	60	17	0	0	Bal	6.05-6.10	standard process
109-4	61	17	0	0	Bal	6.05-6.10	standard process
109-6	62	17	0	0	Bal	6.05-6.10	standard process
104-2	63	21	3	0.75	Bal	6.22	VM(a)-3h-dry
102-2	64	21	3	0.75	Bal	6.22	VM-2.5h-dry
131-1	65	24	3	1.0	Bal	6.16	VM-4h-dry
133-2	66	25	3	0.5	Bal	6.26	no VM
111-12	67	17	0	0	Bal	6.05	standard process
138-H-1	68	18	0	0	Bal	6.15	first cup-shaped(b) standard process
149-A	69	17	0	0	Bal	6.08	standard process
150-A	69	17	0	0	Bal	6.10	standard process
151-A	69	17	0	0	Bal	6.11	standard process
152-A	69	17	0	0	Bal	6.09	PNL-800 oxide

(a) VM = vibratory milling.
(b) Cup-shaped design used in Experiments 68 and 69.

1. Blend 57.3 wt% NiO and 42.7 wt% Fe_2O_3 by conventional dry milling for 24 h.

2. Calcine the mixed oxides at 800°C for 4 h to form the duplex $NiO-NiFe_2O_4$ oxide powder.

3. Blend 79 wt% oxide powder with 17 wt% Cu (Aremco "5-15 μm" Cu), 2 wt% polyvinyl alcohol (PVA binder), and 2 wt% polyethylene glycol (PEG binder).

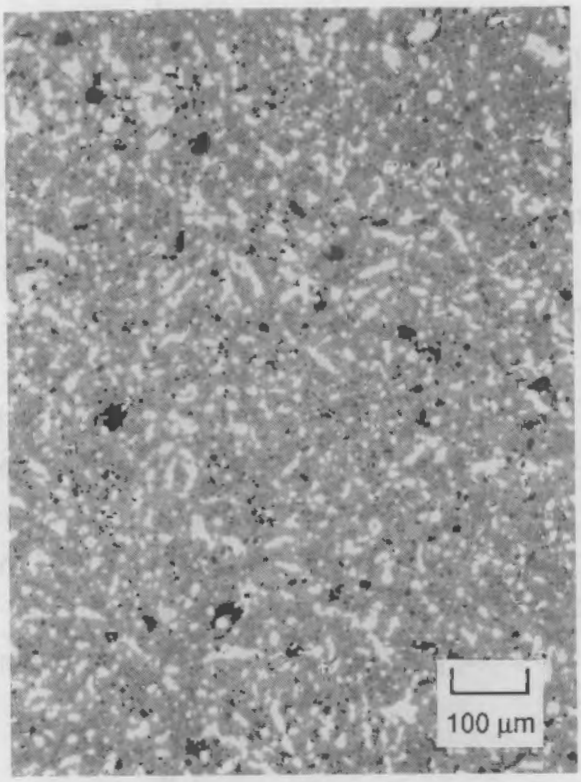

152-4

FIGURE 5.5. NiO-$NiFe_2O_4$-17% Cu. Density 6.11 g/cm^3. Anode Type 152-A. PNL Oxide/Aremco Cu.

4. Ballmill the mixture for 16 h in distilled water.

5. The resultant powder is then dried, pre-compacted, then granulated to -14 mesh (Tyler Series).

This process yields a granulated powder that can be used in isostatic pressing operations. Although the powder flows well and has a relatively good tap density, it should be stressed that this is not an optimized process suitable for scale-up. This powder was pressed and sintered using the standard PNL methods. Anode number 152-A was produced using this powder and used in Test 69. This anode was sintered to a density of 6.1 g/cm^3, which is slightly higher than that of anodes fabricated using the spray-dried Stackpole oxide powder.

Variations from the steps listed previously have included the use of vibratory milling after the calcination step. Vibratory milling is a more efficient and effective method of blending and dispersing the binder/

lubricant and copper in the oxide powder. The milling step also breaks up all the powder particles to sizes that aid sintering.

Overall cermet metal loadings could be increased by using vibratory milling. The as-sintered density of cermets prepared with milling as a process step was higher than the density of standard PNL cermets. Figure 5.6 shows the microstructure of a NiO-$NiFe_2O_4$-17% Cu cermet sintered to a density of 6.18 g/cm^3. The only fabrication difference between this cermet and the one shown in Figure 5.4 is a 5-h vibratory milling/blending step used after the calcination step. Although the microstructure is not significantly different, much of the Cu metal phase is more finely dispersed, which may aid in improving the electrical conductivity of the cermet. The remaining Cu metal phase particles appear as thin rodlets and plates dispersed throughout the matrix. Additional work is planned in FY 1989 to determine the significance of this microstructure.

149-7

FIGURE 5.6. Anode from PNL Vibration-Milled Oxide, NiO-$NiFe_2O_4$-17% Cu. Density 6.18 g/cm^3.

Figure 5.7 shows the resulting microstructure of a cermet, which included 24 wt% of an 85 wt% Cu/15 wt% Ni metal. This high alloy content was made possible by the homogeneous dispersion of particles that vibratory milling affords. The Cu/Ni alloy mixture is prepared by blending Cu and Ni powders in a vibratory mill. The sample microstructure shown in Figure 5.7 was prepared by vibratory milling the PNL-800 oxide powder, Cu/Ni alloy powder, and the binder/lubricants for 4 h. The as-sintered density of this sample was 6.33 g/cm^3. Although the benefits of high density and fine metal phase dispersion are not yet fully understood, future research is planned to evaluate these properties.

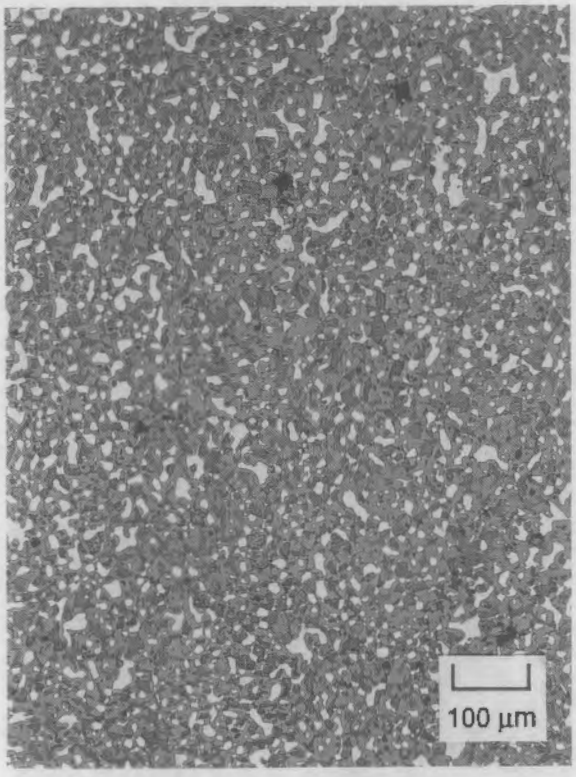

151-16

FIGURE 5.7. Anode Sample from PNL-800 Oxide Cermet, 24% Alloy (85 Cu/15 Ni) with 86% NiO-$NiFe_2O_4$.

Advanced Cermet Anodes

Fabrication efforts continued in FY 1988 on the development of the NiO-$NiFe_2O_4$-Cu-Ni-Al cermets. These Al-containing anodes have exhibited the highest electrical conductivities of any cermet anode material, i.e., over 400 ohm^{-1} cm^{-1} at a temperature of 900°C. Two basic microstructures have been produced; Figure 5.8 shows a relatively porous microstructure (~90% of theoretical density), while Figure 5.9 shows a dense microstructure (~96% of theoretical density). The basic fabrication processes used to fabricate these cermets has been discussed previously (Strachan et al. 1988).

Four NiO-$NiFe_2O_4$-Cu-Ni-Al anodes were tested in FY 1988: anode numbers 104-2, 102-2, 131-1, and 133-2, which were used in tests numbered 63, 64, 65, and 66, respectively. The pre-sintered compositions of these anodes are

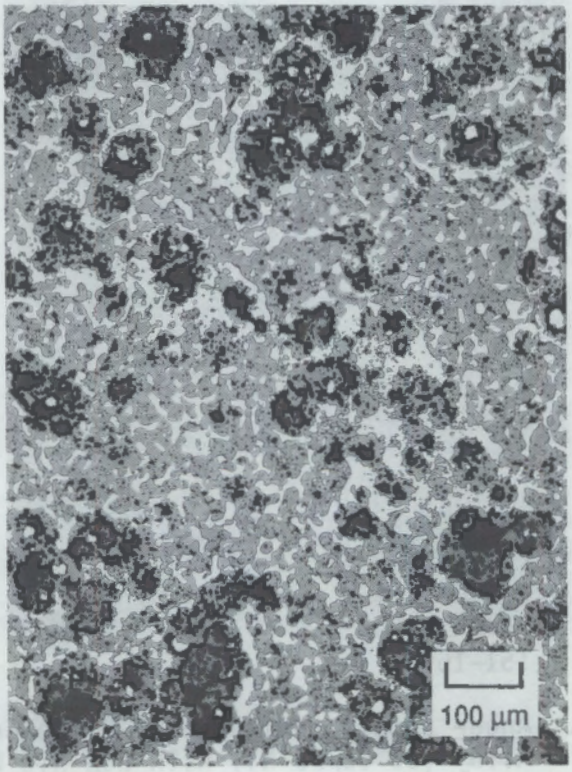

64-7

FIGURE 5.8. NiO-$NiFe_2O_4$-Cu-Ni-Al Porous Cermet Microstructure. This cermet contained 29 wt% Cu-metal alloy and had a density of 5.9 g/cm^3.

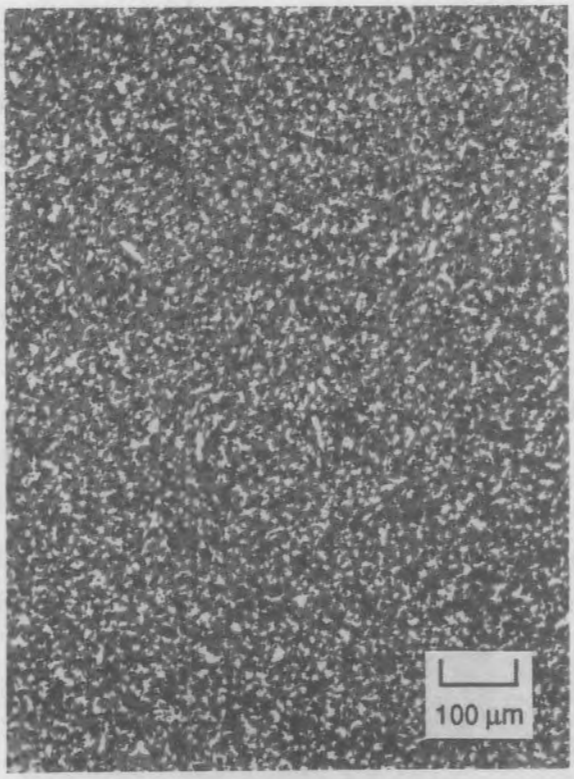

64-5

FIGURE 5.9. $NiO-NiFe_2O_4$-Cu-Ni-Al Dense Cermet Microstructure. This cermet contained 29 wt% Cu-metal alloy and had a density of 6.3 g/cm^3. The powders used to make this cermet were vibratory milled.

listed in Table 5.1. Basically, these anodes were prepared by adding a small quantity of finely divided Al powder as a sintering and/or reaction catalyst to a $NiO-NiFe_2O_4$-Cu-Ni powder mixture. All of the anodes tested had the high-density microstructure.

Anodes numbered 104-2 and 102-2 contained 21 wt% Cu and 3 wt% Ni, had a density of 6.22 g/cm^3, and a microstructure similar to that shown in Figure 5.9. These anodes were prepared by dry vibratory milling of the powders as opposed to wet vibratory milling described in Strachan et al. (1988). This was done as part of a continuing effort to determine the trade-offs between fabrication cost and final product.

Anode 131-1 contained slightly more Al and an increased quantity of Cu and Ni. The as-sintered density decreased slightly, but the microstructure was similar to that shown in Figure 5.9. The reason for the decrease in density is unknown. The microstructure of Anode 131-1 is shown in Figure 5.10.

The effect of vibratory milling can be seen by comparing the microstructure of Anode 131-1 with that of Anode 133-2 (Figure 5.11). Anode 133-2 was prepared from powders that were not vibratory milled. The microstructure exhibits residual particle boundaries of the spray-dried NiO-$NiFe_2O_4$-Cu agglomerates. The reasons for the high density without vibratory milling are not yet fully understood, and will be investigated in FY 1989. The ability to obtain a dense cermet without using vibratory milling is desirable, as

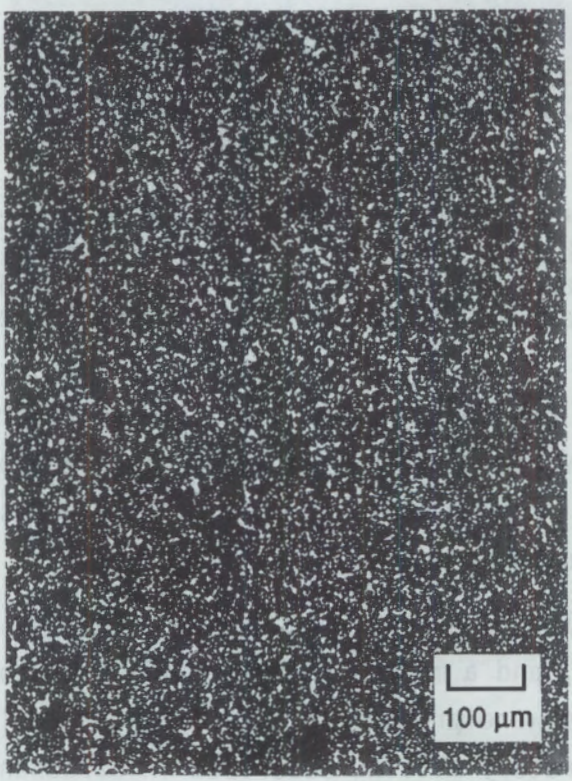

133-A

FIGURE 5.10. NiO-$NiFe_2O_4$-Cu-Ni-Al Cermet Anode (24 wt% Cu, 3 wt% Ni, 1 wt% Al). The as-sintered density was 6.16 g/cm^3.

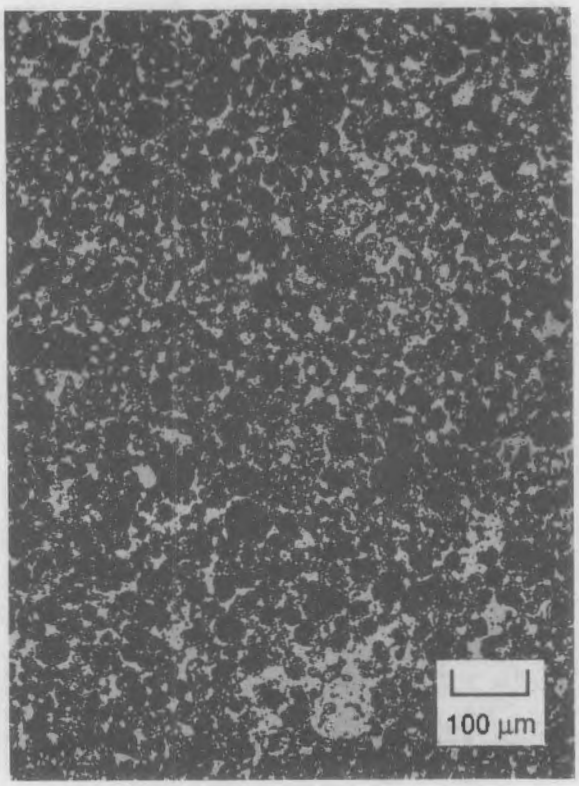

133-B

FIGURE 5.11. NiO-$NiFe_2O_4$-Cu-Ni-Al Cermet Anode (25 wt% Cu, 3 wt% Ni, 0.5 wt% Al). The as-sintered density of this anode was 6.26 g/cm^3. No vibratory milling was used in the preparation of powders used to make this anode.

elimination of the vibratory milling operation would allow retention of good flow properties of the powder while eliminating the processing time/power requirements associated with the milling operation.

Other catalyst metals have been previously suggested (Marschman and Davis 1987) for producing the high-alloy, high electrical conductivity cermets. The microstructure shown in Figure 5.12 was produced using Mg as the sintering aid/reaction catalyst rather than Al. In this case 0.75 wt% Mg was dry vibratory milled for 3 h with 21 wt% Cu, 3 wt% Ni, and the balance spray-dried NiO-$NiFe_2O_4$-Cu powder. The as-sintered density was 6.15 g/cm^3. This cermet has not been electrochemically tested, but it is interesting to note that fine dispersion of Cu yields a highly electrically conductive cermet, which is a desirable characteristic for cermet anodes.

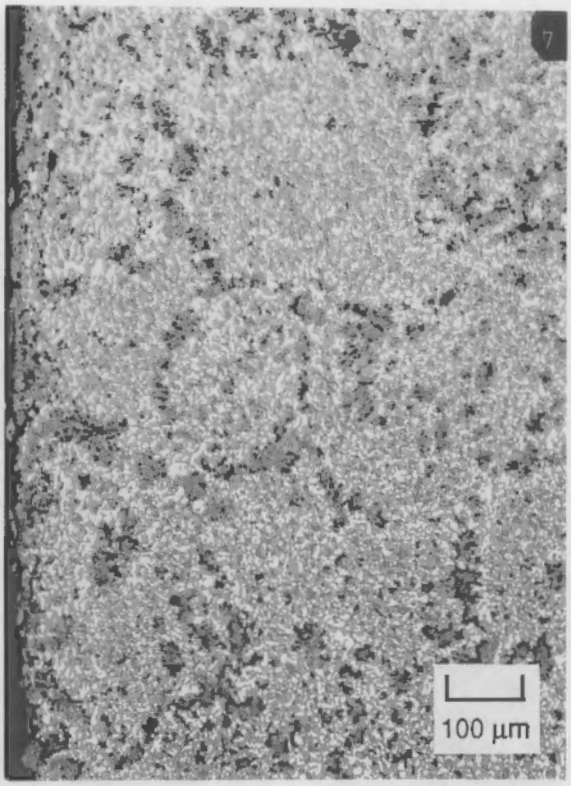

145-12

FIGURE 5.12. Advanced High Alloy Cermet Anode (75% $NiO-NiFe_2O_3$/ 21% Cu/3% Ni with 0.75% Mg as a catalyst). Density: 6.15 g/cm^3.

6.0 CATHODE PERFORMANCE

The objective of this work is to determine the degradation mechanisms for TiB_2-based cathode materials. Specifically, the studies concern the corrosion mechanisms that take place in TiB_2-graphite materials which are candidate materials for use as cathodes in Hall-Heroult cells.[a] However, the scope of the work was limited in that the electrolysis experiments were optimized for anode performance and not for the investigation of the cathode performance. Nevertheless, useful information was obtained from these experiments.

The performance of TiB_2-graphite materials as candidate materials for cathodes in Hall-Heroult cells was evaluated by including samples in eight electrolysis experiments. These materials consisted of disks of approximately the diameter of the inside of the cell in which they were tested. The disk of TiB_2-graphite was placed on the bottom of the cell; no method of attachment was used. A disk of Al metal was placed over the TiB_2-graphite and solid electrolyte on top of the Al prior to heating the cell. In some of these tests, the power to the anodes was turned off and the anode was removed from the cell. This was done during off-shift hours and weekends. After the test was completed and the furnace cooled, the TiB_2-graphite disk was broken away from the resolidified electrolyte and sectioned for evaluation under a microscope.

Results from the study of TiB_2-graphite cathodes in eight electrolysis cells are summarized in Table 6.1. Most of the information relating to cathode performance in Table 6.1 is qualitative in nature, e.g., "severe cracking" or "severe spalling." The size and concentration of the cracks, for instance, was not measured. It should be noted that the composition of the electrolyte is the target composition at the beginning of the test. Samples of the electrolyte were not taken during the experiments (see Section 4.2), but the solidified salt was analyzed at the end of each test.

(a) The TiB_2-graphite composites used in the study were supplied by Great Lakes Research Corporation, Elizabethton, Tennessee.

TABLE 6.1. Results from Measurements on the TiB_2-Graphite Specimens from Eight Laboratory Electrolysis Tests

Measurements	Test Number 59	60	61	62	63	64	65	66
Time with electrolysis, h	11.75 @ 980°C	18.25 @ 970°C	20.25 @ 970°C	20.5 @ 970°C	20 @ 973°C	19.5 @ 975°C	19.5 @ 970°C	20 @ 970°C
Time without electrolysis, h	101.25 @ 800°C	106 @ 800-880°C	12.75 @ 970°C	11 @ 970°C	1 @ 973°C	19 @ 975°C	16.5 @ 970°C	16.5 @ 970°C
Subsurface cracks	severe	severe	none	few	very few	few	none	few
Thermal stress cracks	severe	none	few	few	severe	severe	severe	severe
Al_4C_3 crystals	frequent	frequent	very few	few	very few	very few	very few	very few
Spalling	severe	severe	none	few	few	few	few	very few
Intergranular cracking and Al penetration	frequent	isolated regions	few	few	few	few	very few	very few
Depth of Al penetration, μm	70	140	50	130	94	115	82	100
TiB_2-G/Al mass ratio	1.62	1.09	0.48	0.41	0.45	0.63	0.5	0.51
Bath/Al mass ratio	30.7	30.5	15.5	11	16.3	19.9	18.5	17.2
Bath/TiB_2-G mass ratio	8.9	28.4	32.6	26.5	36.3	31.4	37.4	34
Anode	17% Cu	2 @ 17% Cu	17% Cu	17% Cu	alloy	alloy	alloy	alloy
Na_3AlF_6, wt%	83.3	78.5	83.3	89.77	87	90.9	85.3	83.86
Al_2O_3, wt%	8	8	8	5	5	5	6.75	6.25
AlF_3, wt%	3.7	9.5	3.7	3.23	3.81	3.98	3.73	5.15
CaF_2, wt%	5	4	5	0	4.2	0.04	4.22	2.74
LiF, wt%	0	0	0	2	0	0	0	2
TiB_2-G machined?	no	no	no	no	yes	yes	yes	yes

The results summarized in Table 6.1 corroborate earlier findings (Strachan et al. 1988; Schilling and Graff 1988) involving long-term "soak tests" that the time period during which the electrolysis cell is off is the period of most rapid degradation of the TiB_2-graphite material. From those tests, it was concluded that Al_4C_3 can form at the Al-graphite interface. Because there is a 3:1 volume expansion when C is converted to Al_4C_3, it is surmised that the formation of Al_4C_3 results in cracking and spalling from stresses which exceed the strength of the material. Results from the experiments performed in FY 1988 (Table 6.1), indicate that the TiB_2-graphite material suffered the most severe cracking and spalling in the tests where the current was off for a significant period. It was also in those tests that Al_4C_3[(a)] crystals were found in the highest number. These features are shown in Figures 6.1 (250 magnification) and 6.2 (500 magnification).

The results indicating the effect of Al_4C_3 formation at the Al/TiB_2-graphite interface are complicated by the fact that the mass ratio of TiB_2-graphite material to Al is also high for the two specimens from Tests 59 and 60. That is, another interpretation could be that the Al became more easily saturated in these two tests because of the low mass of Al in the cell. The end result, however, still appears to be the same; when the Al becomes saturated or nearby saturated with Al_4C_3, Al_4C_3 may form at the Al/TiB_2-graphite interface and degradation of the TiB_2-graphite matrix may follow. Increasing the amount of Al in contact with the TiB_2-graphite may delay the onset of Al_4C_3 precipitation because it takes longer for the Al to become saturated. What cannot be determined from these data and previous data is whether the precipitation occurs before the bulk of the Al becomes saturated with Al_4C_3; i.e., is the Al-C reaction relatively rapid at the Al-C interface, or must the entire mass of Al become saturated before Al_4C_3 precipitates at the TiB_2-graphite surface? Additional research is needed to confirm the degradation mechanisms and to determine if similar behavior is to be expected in a full-scale industrial cell.

(a) From studies performed in FY 1987, X-ray diffraction results indicated the presence of Al_4C_3. The crystals found in these tests are assumed to be Al_4C_3 based on the near-identical morphology.

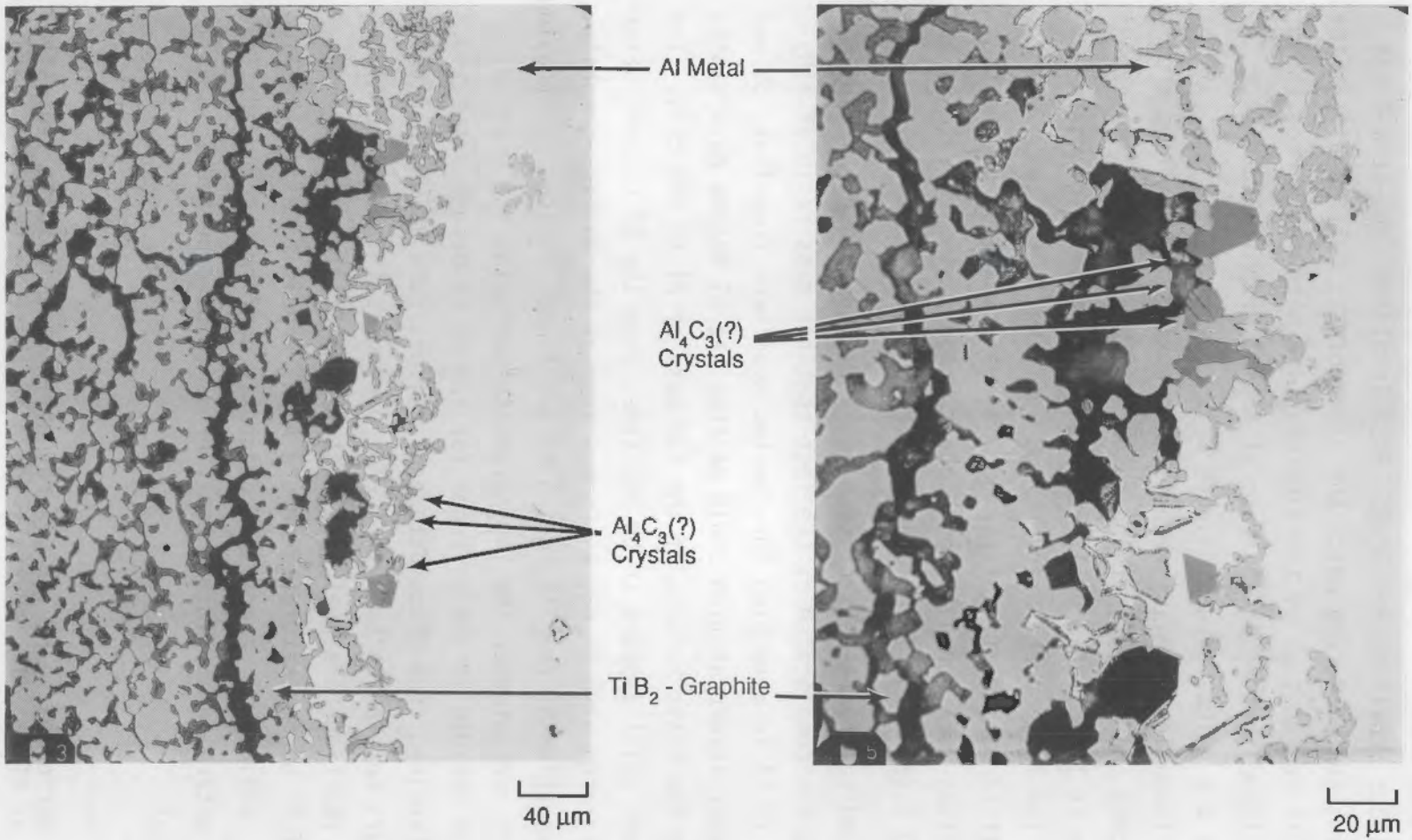

FIGURE 6.1. Photomicrographs of the TiB_2-Graphite Specimen from Test 59 showing Al_4C_3 (?) Crystals and the Resulting Spalling and Cracking

The target electrolyte compositions are also listed in Table 6.1. Since the composition was not monitored throughout the test, it is not possible to extract any firm indication of the effect of electrolyte composition on the degradation of the cathode material. During the test, $NaAlF_4$ is volatilized, which causes the bath ratio to shift to higher values. In these tests, any electrolyte losses were made up by adding the electrolyte components as shown in Table 6.1 but without the Al_2O_3. Therefore, there does not appear to be any strong indication of an effect of electrolyte composition on the degradation of the cathode material. However, since volatility tended to make all of the electrolytes have the same bath ratio, the effect of electrolyte composition on the degradation of the cathode is confounded. Further testing is required to determine if the degradation of the TiB_2-graphite material is sensitive to the electrolyte chemistry.

Data from Table 6.1 indicate there is a strong correlation between machining of the TiB_2-graphite and thermal stress cracking. Figure 6.2 illustrates this effect. Also shown in Figure 6.2 is the effect of process defects, which seem to act as regions in which cracks can initiate relatively easily.

Finally, it appears that a significant portion of the degradation occurs at the corners of the specimens. This degradation is illustrated in Figure 6.3, which is a photomicrograph of the specimen from Test 63. Note that the Al has infiltrated the TiB_2-graphite composite and dissolved the graphite. In these ordinary light photomicrographs, the graphite appears black, the TiB_2 a medium gray, and the Al white.

The extent of infiltration does not appear to be a function of the time of exposure (Table 6.1). However, an accurate measure of the penetration depth is difficult because of possible TiB_2-graphite spallation or dissolution.

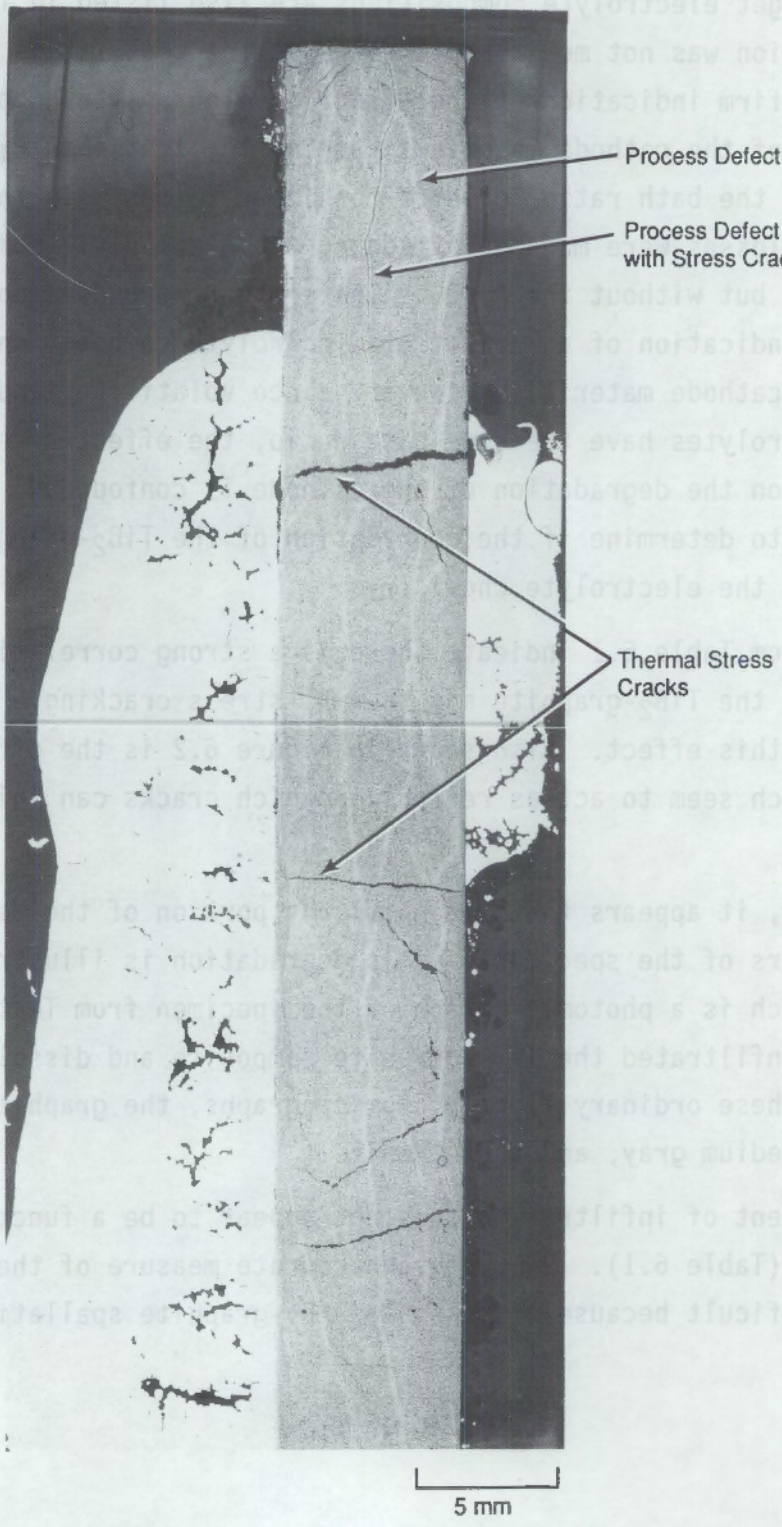

FIGURE 6.2. Photomicrograph of the TiB_2-Graphite Specimen from Test 66 Showing Process Defects and Thermal Stress Cracks

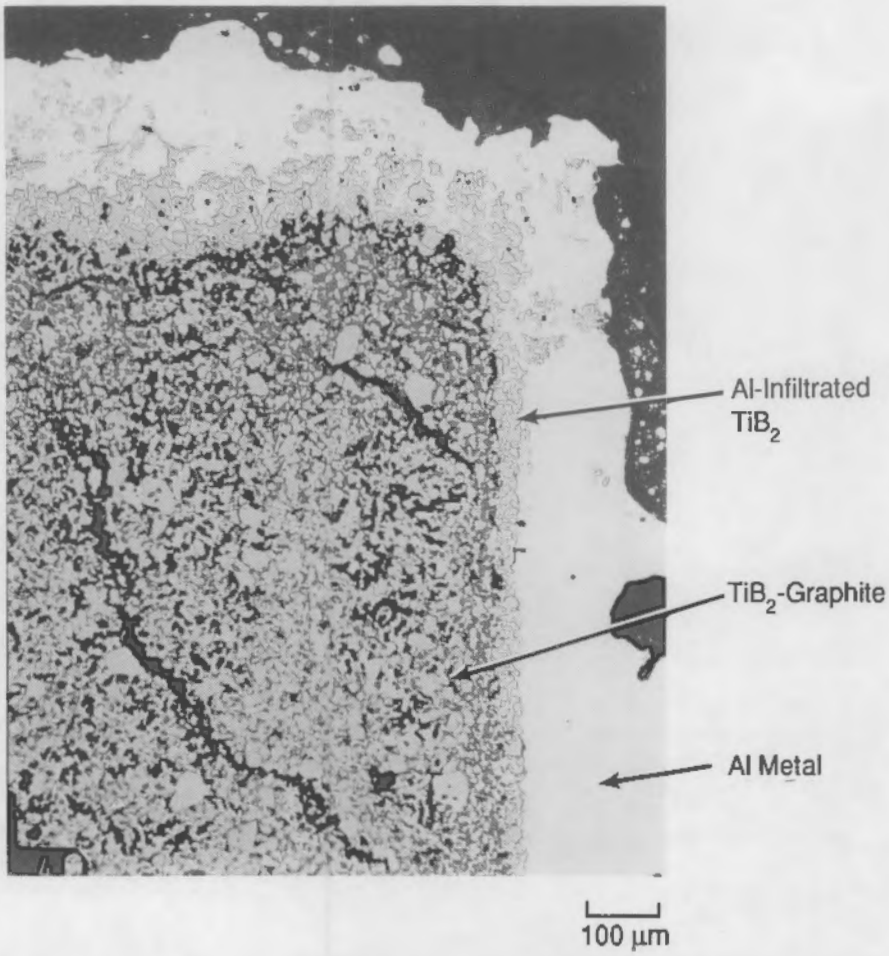

FIGURE 6.3. Photomicrograph of the TiB_2-Graphite Specimen from Test 63 Showing Degradation at the Corner of the Specimen

Al-Infiltrated
TiB2
TiB2-Graphite
Al Metal
100 µm

7.0 CONCLUSIONS AND FUTURE DIRECTIONS

The principal conclusions and future directions of the technical work performed on the Inert Electrodes Program at PNL in FY 1988 are presented in this section of the report, keyed to the major FY 1988 work divisions: 1) Scale-Up Activities; 2) Anode Performance; 3) Cathode Performance; and 4) Anode Materials.

7.1 SCALE-UP ACTIVITIES

7.1.1 Conclusions

- The first large anode for pilot-scale tests will be produced at Cercom, Inc., Vista, California. The schedule calls for delivery of the prototype anode to take place during February 1989.

- Electrical connector development work, indicates that a core of metal can be placed in the anode for the connector junction by including a "core" of metal powder alloy in the desired location when the isostatic mold is being filled. If required, the thermal expansion may be matched to that of the cermet material to minimize induced thermal stresses. The connector rod is expected to become diffusion-welded to the metal core.

- Mechanical tests of the NiO-$NiFe_2O_4$-17% Cu cermet material indicate a 4-point flexure strength of 97.7 MPa ±3.5 MPa and a 109 GPa ±14 GPa bending modulus at room temperature. At 1000°C a stress (corresponding to the maximum tensile fiber stress) of ~30 MPa was required to initiate plastic flow in a short-term 4-point bending test.

- Thermal diffusivity and thermal expansion properties of the NiO-$NiFe_2O_4$-17% Cu cermet material have been determined and catalogued for input into the large-scale anode design and process control process.

- Finite element analyses of a typical large-scale anode design were undertaken to determine the magnitude and location of thermal stresses. Maximum stresses were found to be located in the region of the metal conductor attachment insert, and were high enough to require yielding of the material. The material is apparently capable of undergoing the degree of deformation required at elevated temperatures, though it is important that 1) the CTE differences between anode components be minimized, 2) the anode be heated/cooled slowly, and 3) thermal cycling of the anode be avoided.

7.1.2 Future Directions

- The future emphasis in Scale-Up Activities will involve the large-scale testing of conceptual anode designs. It is anticipated that the first large-scale test, planned for FY 1989, will be performed in a pilot-scale cell (a cell intermediate between a production cell and a large laboratory cell) at Reynolds Metals Co., Sheffield, Alabama, using a single anode. This test is expected to be followed by a test utilizing a cluster of anodes. The ultimate objective is the successful demonstration of the inert anode in an actual industrial cell.

- In order to verify that the design of the anode and anode cluster will function in the large test cell as predicted, a porous graphite model of the anode cluster will be constructed and tested in water. Air bubbled through the porous graphite will give an indication of anode performance in a cell electrolyte. Various anode geometries will be evaluated.

- Mechanical strength determinations will be made on material recovered from anodes used in large-scale tests, to determine the rate at which material properties change when the anodes are exposed to the aggressive cell environments. These values will be used for future finite element database information.

- The heat conduction rate properties of the anode material are expected to vary with anode exposure time in an electrolysis cell. This property, in concert with the mechanical strength, will dictate the acceptable cooldown rate during a cell upset or shut down. Thermal diffusivity measurements will be made on used-anode-material specimens and employed in the finite element stress analysis evaluation of anode designs.

- The electrical conductivity changes of anode materials under operating conditions are potentially important to cell efficiency, so small increases in resistance become significant in light of the large currents passing through the anode. If the conductivity of the cermet material decreases with time, the power consumption caused by joule heating of the anode may limit its useful life on economic grounds. The electrical conductivity of specimens obtained from used anodes will be evaluated to determine whether or not a conductivity problem exists.

7.2 ANODE PERFORMANCE

7.2.1 Conclusions

- In electrolysis tests performed in FY 1988, the degradation of the inert anode materials appeared to be insensitive to electrolyte composition. The additions of LiF and CaF_2, for example, had no influence on anode degradation.

- Fe and Ni impurities were not found in a 2:1 stoichiometric ratio in the electrolytically produced Al - the ratio was determined to be 11:1. No conclusions could be drawn concerning the ratio of Fe to Ni in the electrolytes, as the sources of impurities could not be determined.

- Round-bottomed anodes exhibited less wear in the transition region between anode sides and bottoms than square-edged anodes. A critical radius was not determined.

- No firm conclusions could be drawn regarding the performance of NiO-$NiFe_2O_4$-Cu-Ni-Al cermet anode materials because fabrication artifacts influenced the performance of the anodes. However, based on the quantity of impurities found in the electrolytically produced Al, these cermets performed as well as other cermets tested during FY 1988.

- Hollowed-out, thin-walled cermet anodes can be used to perform successful electrolysis.

- The vapor phase in an operating electrolysis cell did not appear to enhance the degradation of the NiO-$NiFe_2O_4$-17% Cu anode used in the (single) experiment performed.

- Clusters of two and three anodes were operated simultaneously without difficulty.

- SiC is not a suitable cell material, as it is rapidly attacked by the cell electrolyte.

- A 100-h test, in which the metal phase of a NiO-$NiFe_2O_4$-17% Cu anode oxidized to a depth of ~1 cm, suggests the possible suitability of an anode material in which some portion of the metal phase is replaced with copper oxide(s).

- An experimental apparatus for determining the current efficiency of cermet anodes during the electrolytic production of aluminum, and which will permit the evaluation of anode-cathode distance spacing (ACD), anode/cathode slope, bath chemistry, electrode geometry, and electrode materials on the current efficiency, is under construction. It will be placed in service in FY 1989.

7.2.2 Future Directions

- The experimental ACD apparatus will be made operational through a series of shakedown tests.

- Tests will be performed to determine 1) the performance of anodes of various compositions, including anodes containing Cu_2O and CuO; 2) the performance of anodes in electrolytes of various compositions; 3) the electrochemical behavior of the anodes; and 4) the effect of tilt angle on cell performance.

7.3 CATHODE PERFORMANCE

7.3.1 Conclusions

- The TiB_2-graphite degradation mechanism suggested by the work performed to date involves saturation of the Al with Al_4C_3 at the interface between the infiltrating Al and the TiB_2-graphite. As Al_4C_3 precipitates, the volume expansion causes stresses in the material, which eventually exceed the strength of the TiB_2-graphite. Spalling and cracking result from these stresses. However, under electrolysis the concentration of Al_4C_3 in the Al does not appear to reach saturation, perhaps because of the oxidation of Al_4C_3 at the Al-electrolyte interface or dissolution of the Al_4C_3 into the electrolyte.

  Results from FY 1987 work suggest that components of the electrolyte play a role in the degradation of TiB_2-graphite. In specimens tested under electrolysis, a zone rich in Na and F was found deeper in the material than the Al-rich zone. These components appeared to hinder the further migration of Al into the specimen. More information on this effect would be desirable.

7.3.2 Future Directions

- No future work specifically directed toward cathode performance is planned.

7.4 ANODE MATERIALS

7.4.1 Conclusions

- The effect of cermet composition, cermet powder constituent characteristics, and cermet processing on the microstructure and density of the final cermet product have been investigated and catalogued as an integral part of the procedure for preparing laboratory-scale experimental anodes.

7.4.2 Future Directions

- Experimental anodes will be produced at PNL for use in the ACD apparatus (see Section 7.2.2).

- Experience gained at PNL in the formulation and processing of laboratory-scale anodes will be applied in the fabrication of large anodes for the single- and cluster-anode pilot cell tests.

8.0 REFERENCES

Baker, F. W. 1983. Inert Anodes for Aluminum Smelting, Final Technical Report for the Period 1981 October 01-1982 September 30. DOE/CS/40158, Aluminum Company of America, Alcoa Center, Pennsylvania.

Bulz, R. E. (ed.). 1970. Handbook of Tables for Applied Engineering Sience, The Chemical Rubber Co., Cleveland, Ohio.

DeSalvo, G. J., and R. W. Gorman. 1987. ANSYS Engineering Analysis System User's Manual. Swanson Analysis System, Inc., Houston, Pennsylvania.

Hart, P. E., et al. 1987. Inert Anode/Cathode Program, Fiscal Year 1986 Annual Report. PNL-6247, Pacific Northwest Laboratory, Richland, Washington.

Holman, J. P. 1978. Experimental Methods for Engineers. 3rd edition, McGraw-Hill, New York.

Kreith, F. 1965. Principles of Heat Transfer. International Textbook Co., Scranton, Pennsylvania.

Marschman, S. C. 1989. Laboratory-scale Testing of Non-consumable Anode Materials. PNL-6805, Pacific Northwest Laboratory, Richland, Washington.

Marschman, S. C., and N. C. Davis. 1987. Materials Development for Inert Anodes: Progress Report for the Period from November 1985 to February 1987. PNL-6343, Pacific Northwest Laboratory, Richland, Washington.

Marschman, S. C., N. C. Davis, and R. W. Stephens. 1987. Nonconsumable Anode Electrical Contacts and Support Mechanisms. PNL-6393, Pacific Northwest Laboratory, Richland, Washington.

Neuman, J. P., T. Zhong, and Y. A. Chang. 1984. Bull. Alloy Phase Diagrams 5(2) April.

Schilling, C. H., and G. L. Graff. 1988. Immersion Tests of TiB_2-Based Materials for Aluminum Processing Applications. PNL-6593, Pacific Northwest Laboratory, Richland, Washington.

Strachan, D. M., et al. 1988. Inert Electrodes Program, Fiscal Year 1987 Annual Report. PNL-6746, Pacific Northwest Laboratory, Richland, Washington.

Taylor, R. E., and H. Groot. 1988. TPRL 789 Thermophysical Properties of a Cermet -- A Report to Battelle Pacific Northwest Laboratories. School of Mechanical Engineering, Purdue University, West Lafayette, Indiana.

Weyand, J. D., et al. 1986. Inert Anodes for Aluminum Smelting. Final Technical Report for the Period 29 September 1980 - 30 September 1985. DOE-CONS-40158-20, Aluminum Company of America, Alcoa Center, Pennsylvania.

APPENDIX

THERMOPHYSICAL PROPERTIES OF A CERMET

TPRL

THERMOPHYSICAL PROPERTIES RESEARCH LABORATORY

TPRL 769

Thermophysical Properties of a Cermet

A Report to Battelle Pacific Northwest Laboratories

by

R.E. Taylor and H. Groot

August 1988

School of Mechanical Engineering

Purdue University, West Lafayette, Indiana

TPRL 769

Thermophysical Properties of a Cermet

A Report to Battelle Pacific Northwest Laboratories

by

R.E. Taylor and H. Groot

August 1988

TABLE OF CONTENTS

LIST OF TABLES

LIST OF FIGURES

Thermophysical Properties of a Cermet

INTRODUCTION

Samples of a cermet material were submitted for thermal diffusivity and expansion measurements.

Thermal diffusivity was determined using the laser flash diffusivity method. The flash method, in which the front face of a small disc-shaped sample is subjected to a short laser burst and the resulting rear face temperature rise is recorded, is used in over 80% of the present thermal diffusivity measurements throughout the world. A highly developed apparatus exists at TPRL (Figure 1) and we have been involved in an extensive program to evaluate the technique and broaden its uses. The apparatus consists of a Korad K2 laser, a high vacuum system including a bell jar with windows for viewing the sample, a tantalum tube heater surrounding a sample holding assembly, a spring-loaded thermocouple or an i.r. detector, appropriate biasing circuits, amplifiers, A-D converters, crystal clocks and a minicomputer based digital data acquisition system (Figure 2) capable of accurately taking data in the 40 microsecond and longer time domain. The computer controls the experiment, collects the data, calculates the results and compares the raw data with the theoretical model.

A dual Push-Rod Dilatometer (Theta Dilatronics II, Figure 3) is used to measure linear thermal expansion. The differential expansion between the sample and a known standard reference material is measured as a function of

temperature. The expansion of the sample is computed from this differential expansion and the expansion of the standard. The measurements are made under computer control and the linear expansion is calculated at preselected temperature intervals. The expansion can be monitored with a visual display during the measurement process. Five standard reference materials for expansion are available from NBS and these include materials with low, moderate and large expansions.

RESULTS AND DISCUSSION

The bulk density of the material was determined to be 6.022 gm cm^{-3} based on the diffusivity sample's mass and geometry. The sample is magnetic.

Thermal diffusivity results measured in air are given in Table 1 and are plotted in Figure 4. There is an inflection at the magnetic transformation.

Thermal expansion results are given in Table 2. Thermal expansion values are plotted in Figure 5 and the average coefficient values are plotted in Figure 6. There was good agreement between heating and cooling data.

TABLE 1

THERMAL DIFFUSIVITY RESULTS

SAMPLE NO.	TEMP. (C)	DIFFUSIVITY (cm^2 sec^{-1})
HEAT	23.	0.0258
	100.	0.0221
	200.	0.0184
	300.	0.0167
	400.	0.0160
	500.	0.0155
	600.	0.0142
	700.	0.0140
	800.	0.0135
	900.	0.0129
	1000.	0.0127
COOL	200.	0.0192

TABLE 2

Thermal Expansion Results

Temp. (°C)	Expansion (micro in/in)	Average Coefficient (10^{-6} C^{-1})	Remarks
21	0		
147	1253	9.9	
197	1804	10.3	
247	2498	11.1	
297	3106	11.3	
347	3718	11.4	
397	4363	11.6	
447	5041	11.8	
497	5748	12.1	
547	6496	12.3	
597	7294	12.7	
647	7971	12.7	
697	8601	12.7	
747	9215	12.7	
797	9836	12.7	
847	10510	12.7	
897	11200	12.8	
947	11920	12.9	
997	12760	13.1	
947	12030	13.0	Cooling
897	11250	12.8	Cooling
847	10540	12.8	Cooling
797	9876	12.7	Cooling
747	9228	12.7	Cooling
697	8588	12.7	Cooling
647	7939	12.7	Cooling
597	7256	12.6	Cooling
547	6449	12.3	Cooling

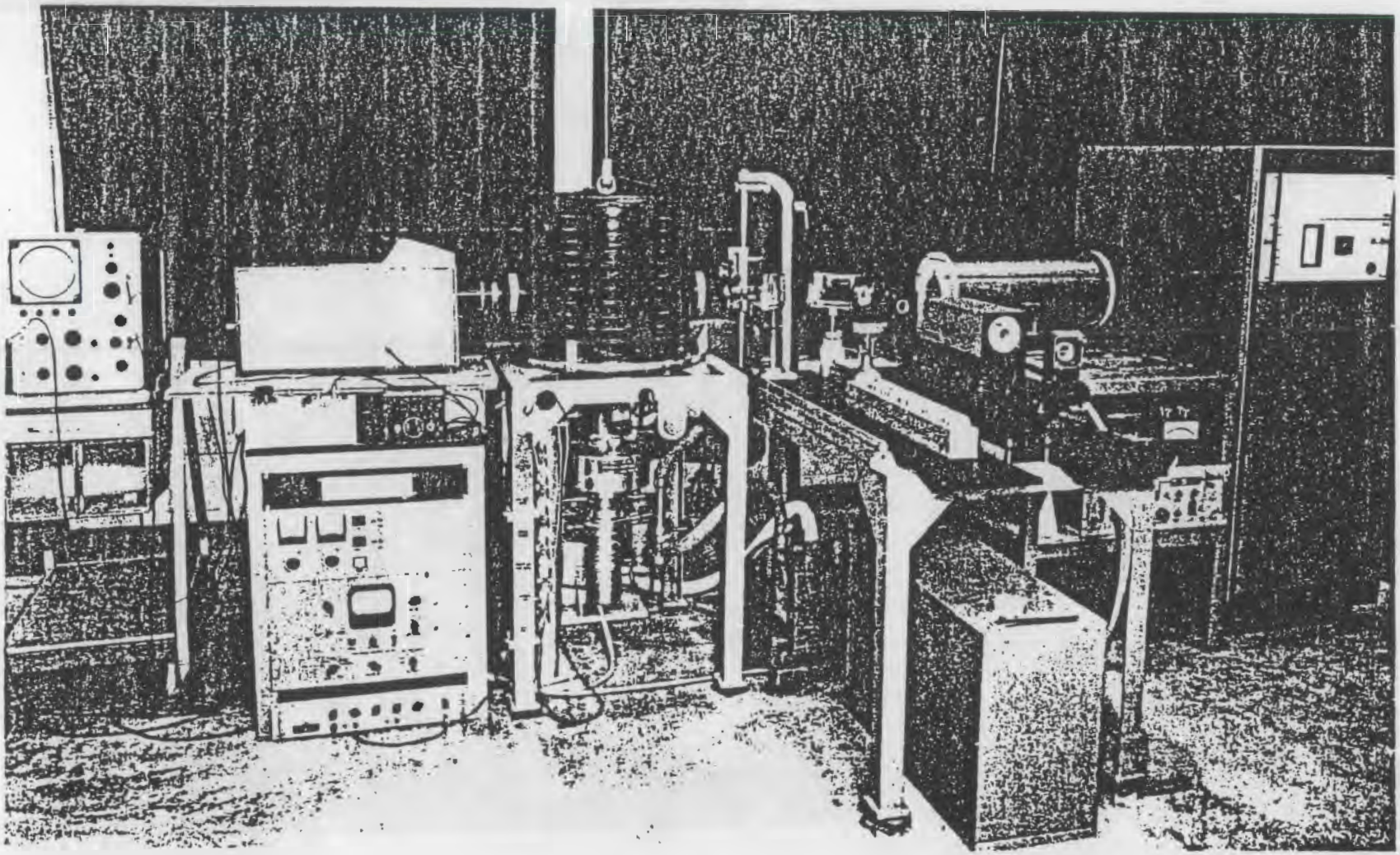

Figure 1. Flash Diffusivity Apparatus

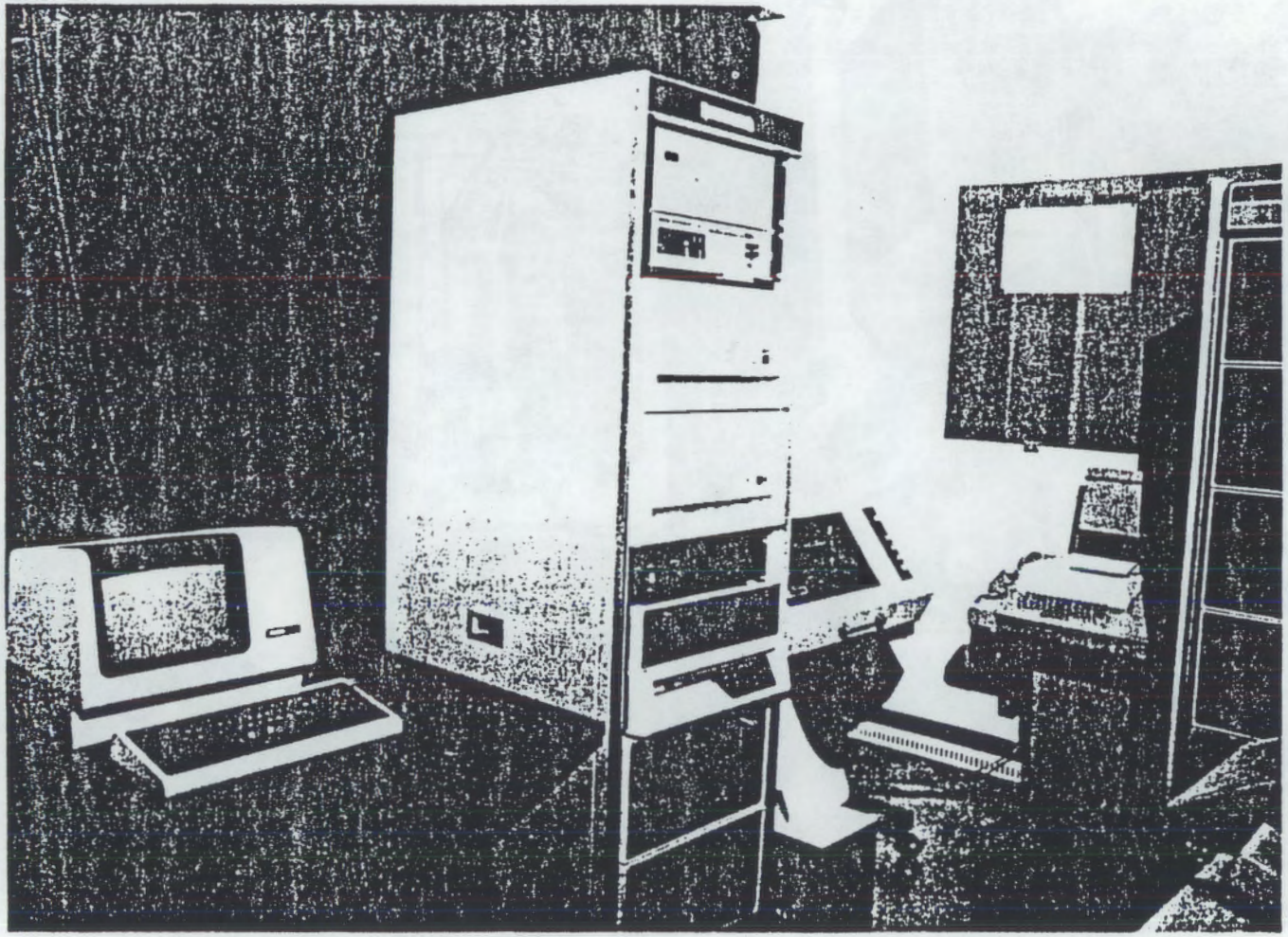

Figure 2. Digital Data Acquisition System

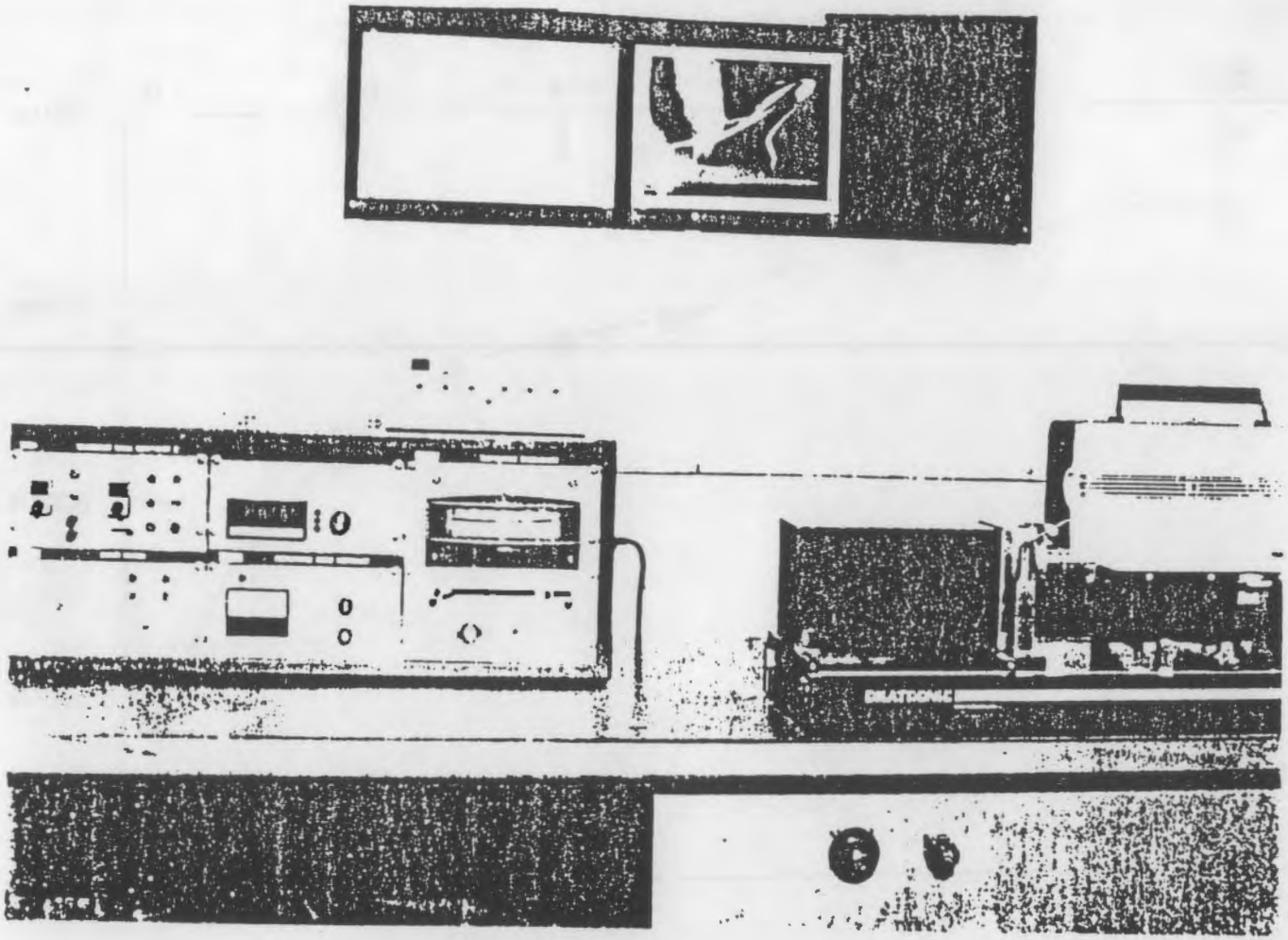

Figure 3. Push-Rod Dilatometer

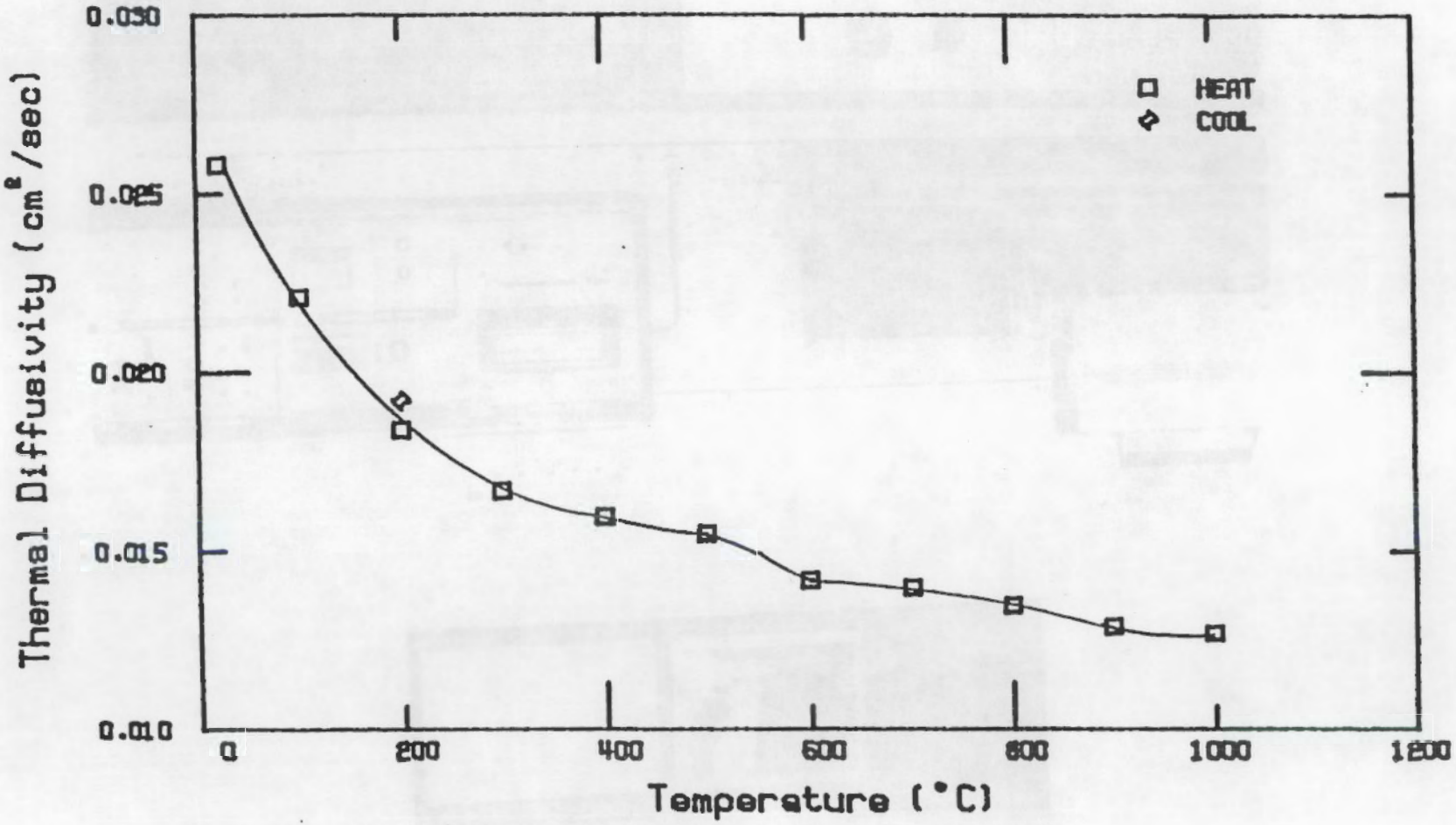

Figure 4. Thermal Diffusivity

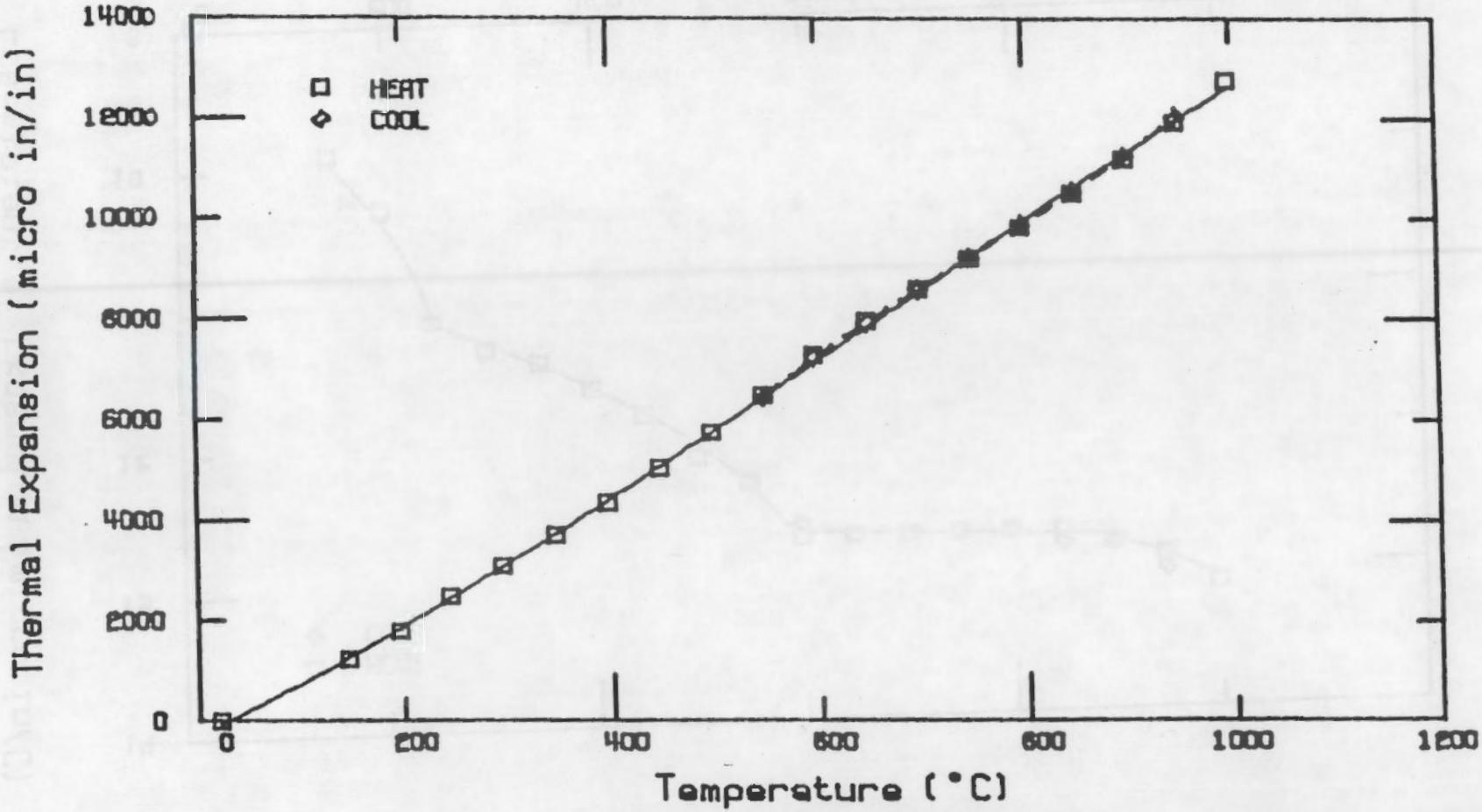

Figure 5. Thermal Expansion

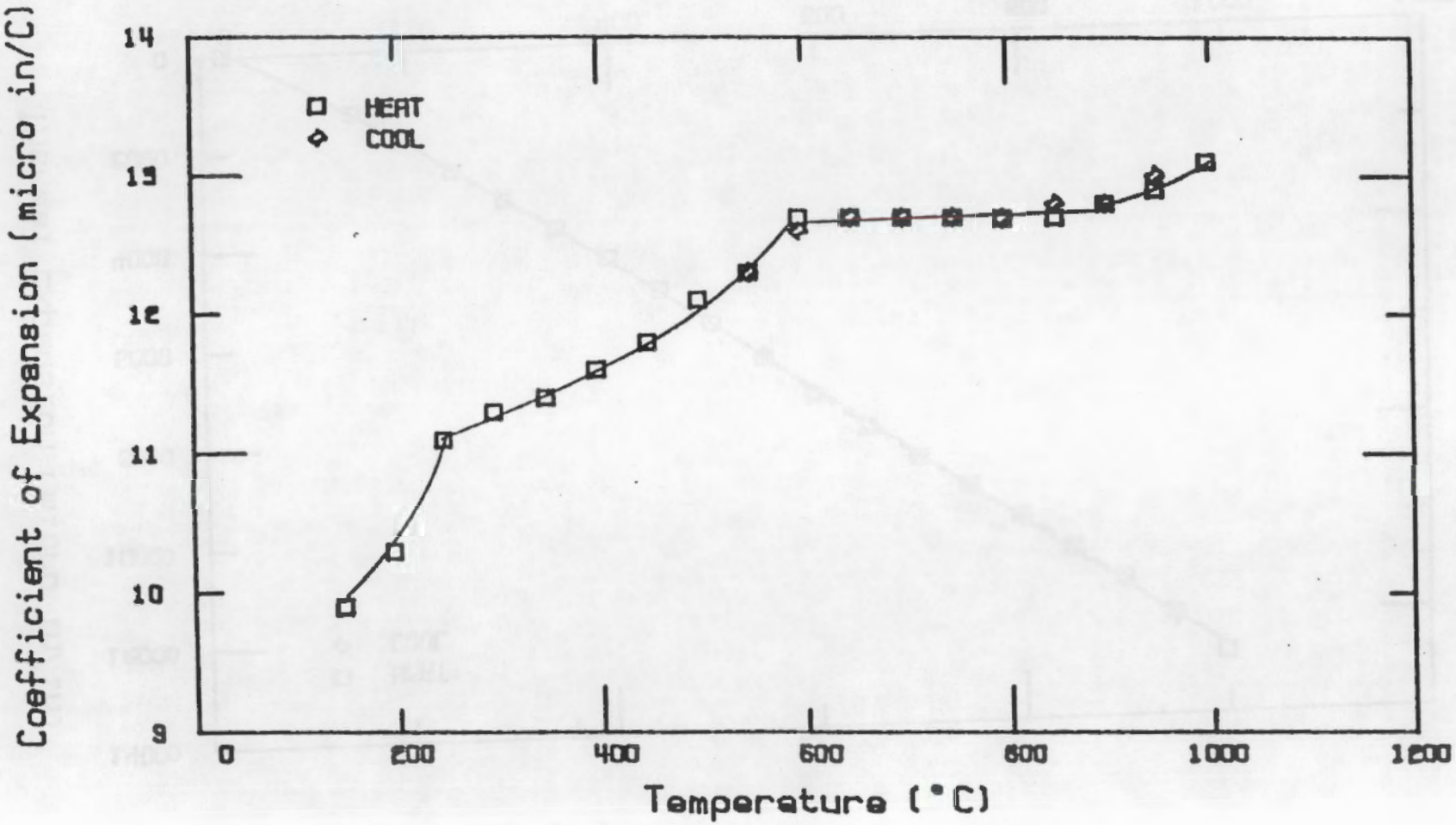

Figure 6. Coefficient of Expansion

DISTRIBUTION

No. of Copies

OFFSITE

M. J. McMonigle
U.S. Department of Energy
Office of Industrial Programs
Forrestal Building
Washington, DC 20585

T. J. Gross
U.S. Department of Energy
Office of Industrial Programs
Forrestal Building
Washington, DC 20585

R. L. Sheneman
U.S. Department of Energy
Office of Industrial Program
Forrestal Building
Washington, DC 20585

12 DOE Office of Scientific and Technical Information

C. Anderson
Columbia Aluminum Co.
85 John Day Dam Road
Goldendale, WA 98620

J. V. Anderson
WCVE3
EG&G Idaho, Inc.
Idaho Falls, ID 83415

D. Auburg
Bonneville Power Administration
P.O. 8ox 3621, PDX 97208
Portland, OR 97208

F. W. Baker
Ceramics Division
Alcoa Laboratories
Alcoa Center, PA 15069

No. of Copies

M. Baltzell
Eastalco Aluminum Company
Alumax, Inc.
5601 Manor Woods
Frederick, MD 21701

J. A. Barclay
U.S. Bureau of Mines
2401 "E" Street N.W.
Washington, DC 20241

H. Robert Baumgartner
Ceramics Division
Alcoa Laboratories
Alcoa Center, PA 15069

T. R. Beck
Electrochemical Technology Corp.
1601 Dexter Avenue
Seattle, WA 98109

S. Berwagan
Bonneville Power Administration
P.O. Box 3621 K
Portland, OR 97208

T. M. Besmann
Metals and Ceramics Division
Oak Ridge National Laboratory
P.O. Box X, Bldg. 4515
Oak Ridge, TN 37831-6063

K. A. Blakely
President
Advanced Refractory Technologies, Inc.
699 Hertel Ave.
Buffalo, NY 14207

M. H. Blenk
Du Pont
P.O. Box 787
Niagara Falls, NY 14302

No. of
Copies

L. G. Boxall
Martin Marietta Laboratories
1450 South Rolling
Baltimore, MD 21227

J. Bracher
Kaiser Aluminum and Chemical
Corp.
825 N.E. Multnomah St.,
Suite 960
Portland, OR 97232-2150

R. Brandt
Department of Materials Science
and Engineering
University of Washington FB-10
Seattle, WA 98195

J. J. Brown, Jr.
Materials Engineering
Virginia Polytechnic Institute
Blacksburg, VA 24061

A. Budner
Bonneville Power Administration
P.O. Box 3621--EPA
Portland, OR 97208

A. J. Caputo
Metals and Ceramics Division
Oak Ridge National Laboratory
P.O. Box X
Oak Ridge, TN 37831-6063

N. Clark
Bonneville Power Administration-
Industrial Conservation
P.O. Box 3621
Portland, OR 97208

A. Cooke
Martin Marietta Laboratories
1450 South Rolling
Baltimore, MD 21227

No. of
Copies

J. A. Coppola
Standard Oil Engineered
Materials Company
P.O. Box 156
Niagara Falls, NY 14302

D. D. Cudaback
Director
Washington State Dept of Trade
and Economic Development
312 First Avenue North
Seattle, WA 98109

R. Curtis
Materials Development
Corporation
81 Hicks Avenue
Medford, MA 02155

J. V. Day
Kaiser Aluminum and Chemical
Corp
E2111 Hawthorne Road
Mead, WA 99021

R. Dethlefsen
Maxwell Laboratories
8888 Balboa Ave
San Diego, CA 92123

D. H. DeYoung
Alcoa Technical Center
Alcoa Center, PA 15069

S. Diamond
Battelle Columbus Laboratories
505 King Avenue
Columbus, OH 43201-2693

C. W. Doerr
The Stackpole Corporation
Cermag Division
201 Stackpole Street
St. Marys, PA 15847

No. of
Copies

T. Dwonch
Snake River District
BPA
101 W. Poplar
Walla Walla, WA 99362

G. L. Eitel
Stone & Webster Engineering Corp.
Greenwood Plaza Box 5406
Denver, CO 80217

R. Engdahl
Deposits and Composites, Inc.
318 Victory Drive
Herndon, VA 22070

J. F. Elliott
MIT
Room 4-138
77 Massachusetts Avenue
Cambridge, MA 02139

B. G. Epstein
A. D. Little, Inc.
955 Lenfant Plaza SW 4200
Washington, DC 20024-2119

J. W. Evans
University of California
Dept of Matl. Sci. and Mineral Eng.
Berkeley, CA 94720

R. A. Fenimore
ICI Advanced Materials
Rollins Building, Eighth Floor
Wilmington, DE 19897

D. A. Figgins
ARCO Petroleum Products Co.
P.O. Box 61004
Anaheim, CA 92803-6104

No. of
Copies

P. Foster
Alcoa Laboratories
P.O. Box 772
New Kinsington, PA 15068

J. Gee
Great Lakes Research Corp
P.O. Box 1031
Elizabethton, TN 37643

T. Gilligan
Eltech Systems Corp.
625 East Street
Fairport Harbor, OH 44077

W. M. Goldberger
Superior Graphite Co.
120 S. Riverside Plaza
Chicago, IL 60606

J. Goodwell
Center for Metals Production
Mellon Institute
4400 Fifth Avenue
Pittsburgh, PA 15213

J.A.S. Green
Martin Marietta Laboratories
1450 South Rolling
Baltimore, MD 21227

C. Griffin
Ceramatec Inc.
2425 S. 900 West
Salt Lake City, UT 84119

L. I. Grindstaff
Great Lakes Research Corp.
P.O. Box 1031
Elizabethon, TN 37643

J. Haggerty
MIT
Building 12, Room 009
77 Massachusetts Avenue
Cambridge, MA 02139

No. of
Copies

I. L. Harry
Electric Power Research
Institute
P.O. Box 10412
Palo Alto, CA 94303

W. E. Haupin
2820 7th Street Road
Lower Burrell, PA 15068

H. W. Hayden, Jr.
1419 East 21st Street
The Dalles, OR 97058

R. Hill
Union Carbide Corp.
P.O. Box 94637
Cleveland, OH 44101

H. F. Hillegass
Alcoa Wenatchee Works
P.O. Box 221
Wenatchee, WA 98807

D. G. Howitt
College of Engineering
University of California, Davis
Davis, CA 95616

F. R. Huettig
Advanced Magnetics, Inc.
45 Corey Lane
Mendham, NJ 07945

G. R. Hyde
U.S. Bureau of Mines
2401 "E" Street N.W.
Washington, DC 20241

S. C. Jacobs
Primary Processing
Aluminum Company of America
Alcoa Technical Center
Alcoa Center, PA 15069

No. of
Copies

S. H. Jan
Tennessee Valley Authority
1850 Commerce Union Bank Bldg.
Chattanooga, TN 37401

N. Jarrett
149 Jefferson Avenue
New Kinsington, PA 15068

J. Joesowicz
Material Development Laboratory
Atlantic Richfield
20717 Prairie Street
Chatsworth, CA 91311

J. Johnson
Intalco Aluminum Company
P.O. Box 937
Ferndale, WA 98248

M. H. Johnson
Alcoa Wenatchee Works
P.O. Box 221
Wenatchee, WA 98801

L. Joo
Great Lakes Research Corp
P.O. Box 1031
Elizabethon, TN 37643

M. Karmous
Oregon State Department of
Energy
625 Marion Street, N.E.
Salem, OR 97310

R. Keller
RD 3 Roundtop Road
Export, PA 15632

K. Krupinski
Mail Stop 57
U.S. Steel Technical Center
1 Technical Center Drive
Monroeville, PA 15146

No. of
Copies

G. Y. Lai
Cabot Corporation
P.O. Box 9013
Kokomo, IN 46902-9013

R. A. Landy
Director of Research
North American Refractories Co.
3127 Research Dr.
State College, PA 16801

J. E. Lane
Ceramic Research and
Development Center
Westinghouse Electric
Corporation
1310 Beulah Road
Pittsburgh, PA 15235

Sai-Kwing Lau
Standard Oil Engineered
Materials Company
Niagara Falls R&D Center
P.O. Box 832
Niagara Falls, NY 14302

J. J. Leddy
Dow Chemical U.S.A.
1776 Building
Midland, MI 48640

W. W. Liang
Gas Research Institute
8600 West Bryne Mawr Avenue
Chicago, IL 60631

W. H. Link
Columbia Aluminum Corp.
85 John Day Dam Road
Goldendale, WA 98620

Steve Loftness
Washington State Energy Office
400 E. Union
Olympia, WA 98504

No. of
Copies

W. Long
Building B815
Dow Chemical
Freeport, Texas 77541

A. G. Longmuir
Kaiser Aluminum and Chemical
Corp.
P.O. Box 877
Pleasonton, CA 94566

R. A. Lowden
Metals and Ceramics Division
Oak Ridge National Laboratory
P.O. Box X, Bldg, 4515
Oak Ridge, TN 37831-6063

W. N. Maclay
Koppers Company, Inc.
440 College Park Drive
Monroeville, PA 15146

J. C. McCloskey
Ten Mile River Associates
296 Mt. Hope Street
North Attleboro, MA 02760

S. C. Manaktala
Manager of Technology
Reduction Division
Kaiser Aluminum and Chemical
Corp.
300 Lakeside Drive
Oakland, CA 94643

V. H. Markant
Du Pont
P.O. Box 787
Niagara Falls, NY 14302

C. J. McMinn
Extractive Metallurgical
Department
Reynolds Metals Company
P.O. Box 1200
Sheffield, AL 35660

No. of
Copies

C. H. McMurtry
Standard Oil Engineered
Materials Company
Niagara Falls R&D Center
P.O. Box 832
Niagara Falls, NY 14302

M. A. Mitnick
Avco Specialty Materials
Subsidiary of Textron Inc.
2 Industrial Avenue
Lowell, MA 01851

H. Mortensen
R. Palika
Cercom, Inc.
P.O. Box 70
Vista, CA 92083

A. Moussa
A. D. Little, Inc.
20 Acorn Park
Cambridge, MA 02140

B. C. Mutsuddy
Battelle Columbus Division
505 King Avenue
Columbus, OH 43201-2693

P. Ness
Senior Project Manager
Washington State Dept of Trade
and Economic Development
312 First Avenue North
Seattle, WA 98109

A. N. Patel
Battelle Columbus Laboratories
505 King Avenue
Columbus, OH 43201-2693

J. R. Payne
Kaiser Aluminum and Chemical
Corp.
P.O. Box 877
Pleasanton, CA 94566

No. of
Copies

T. Payne
Columbia Falls Aluminum Co.
Columbia Falls, MT

W. Pebley
Oregon Freeze Dry Corp.
525 25th Avenue SW
P.O. Box 1048
Albany, OR 97321

K. Peterson
Columbia Aluminum Corp.
85 John Day Dam Road
Goldendale, WA 98620

R. D. Peterson
Reynolds Metals Company
P.O. Box 1200
Sheffield, AL 35660

T. R. Pritchett
Kaiser Aluminum and Chemical
Corp.
P.O. Box 877

W. W. Pritsky
Aluminum Association
900 19th St. N.W.
Washington, DC 20006

S. P. Ray
Alcoa Technical Center
Alcoa Center, PA 15069

J. F. Rhodes
Advanced Composite Materials
Corp.
1525 S. Buncomb Rd.
Greer, SC 29651

N. E. Richards
Reduction Laboratory
Reynolds Aluminum Corporation
P.O. Box 1200
Sheffield, AL 35660

No. of
Copies

J. J. Ritter
Ceramics Division
National Bureau of Standards
Gaithersburg, MD 20899

R. C. Rohwedder
3028 Ohio Street
Longview, WA

J. Rosling
Myers Metals and Minerals
459 Colman Building
Seattle, WA 98104

D. R. Sadoway
MIT
Room 8-109
77 Massachusetts Avenue
Cambridge, MA 02139

W. Scott
Department of Materials Science
& Engineering
Wilcox Hall FB-10
University of Washington
Seattle, WA 98195

D. R. Secrist
Great Lakes Research Corp.
P.O. Box 1031
Elizabethon, TN 37643

A. B. Shah
Noranda Aluminum, Inc.
P.O. Box 70
New Madras, MO 63869

N. Shelton
Intalco
1300 S. W. 5th, Suite 3508
Portland, OR 97201

F. W. Spillers
Dow Chemical U.S.A.
B-1210 Building
Freeport, TX 77541

No. of
Copies

Dr. Richard M. Spriggs
Office of the Director
Center for Advanced
Ceramic Technology
Alfred University
Alfred, NY 14802

D. V. Stewart
Reynolds Metals Co.
P.O. Box 1200
Sheffield, AL 35660

D. Strahan
Reynolds Metals Company
P.O. Box 27003
Richmond, VA 23261

A. T. Tabereaux
Reynolds Metals Company
P.O. Box 1200
Sheffield, AL 35660

G. P. Tarcy
Aluminum Company of America
Alcoa Technical Center
Alcoa Center, PA 15069

P. Thaure
Primary Planning and Production
Alumax
400 S. El Camino Rd.
San Mateo, CA 94402

W. H. Thielbahr
Conservative Technology
Division
DOE-Idaho Operations Office
785 DOE Place
Idaho Falls, ID 83402

S. Thomson
General Manager
Klickitat PUD
1313 S. Columbus
Goldendale, WA 98620

No. of
Copies

R. Unger
Merner Research
P.O. Box 248
Ridgewood, NJ 07451

A. Vinnard
Bonneville Power Administration
(KWI)
P.O. Box 3621
Portland, OR 97208

T. Von Muller-KWI
Bonneville Power Administration
P.O. Box 3621
Portland, OR 97208

D. H. Weinblatt
AIMCOR
One Parkway North
Deerfield, IL 60015

J. D. Weyand
Alcoa Technical Center
Alcoa Center, PA 15069

B. Wilcox
Northwest Aluminum Co.
3313 W. Second St.
The Dalles, OR 97058

C. B. Wilson
Dow Chemical U.S. A.
Texas Operations
B-101 Building
Freeport, TX 77541

W. Winnard
Battelle Washington Office
2030 "M" Street N.W.
Washington, DC 20036

J. C. Withers
Keramont Research Corporation
4233 S. Fremont Avenue
Tucson, AZ 85714

No. of
Copies

W. A. Zdaniewski
Engelhard Corporation
Menlo Park, CN 28
Edison, NJ 08818

FOREIGN

D. Brodie
Comalco Ltd.
55 Collins St.
Melbourne, AUSTRALIA

H. Connor
Group Licensing Controller
Johnson Matthey, plc
New Garden House
78 Hatton Garden
London ECIN 8JP ENGLAND

T. Kjar
Comalco Ltd.
55 Collins St.
Melbourne, AUSTRALIA

E. W. Dewing
Alcan International
P.O. Box 8400
Kingston, Ontario
CANADA K7L 4Z4

T. J. Hudson
Alcan International
2001 rue University
C.P. 6090
Montreal, Quebec
CANADA H3C 3H2

D. N. MacMillan
Alcan International
C.P. 1250
Jonquieve, Quebec
CANADA G7S 4K8

No. of
Copies

T. Rawlings
Alcan International Limited
Engineering Division
C.P. 6090
Montreal, Quebec
CANADA, H3C 3H2

J. H. Reimers
Jan H. Reimers and Associates
Inc.
221 Lakeshore Road East
Oakville, Ontario
CANADA, L6J 1H7

A. Oye
Institute of Inorganic Chemistry
Norwegian Institute of Technology
University of Trondheim
N-7034 Trondheim-NTH, NORWAY

J. Thonstad
Laboratories of Industrial
Electrochemistry
Norwegian Institute of
Technology
University of Trondheim
N-7034 Trondheim-NTH, NORWAY

K. O. Vee
ASV Ardal Verk
N-5875 Ardalstargen, NORWAY

No. of
Copies

ONSITE

DOE Richland Operations Office

D. R. Segna

29 Pacific Northwest Laboratory

M. Clement
N. C. Davis
J. R. Divine
P. E. Hart
D. K. Hilliard
O. H. Koski
S. C. Marschman
G. L. McVay
N. L. Moore
L. G. Morgan (10)
C. H. Schilling
D. M. Strachan
R. E. Westerman
C. F. Windisch
Publishing Coordination
Technical Report Files (5)